

Numerical Simulations of Neutron Stars in General Relativistic Hydrodynamics

DISSERTATION

zur Erlangung des akademischen Grades
doctor rerum naturalium (Dr. rer. nat.)



seit 1558

vorgelegt dem Rat der
PHYSIKALISCH-ASTRONOMISCHEN FAKULTÄT
der
FRIEDRICH-SCHILLER-UNIVERSITÄT JENA

von Dipl.-Phys. Marcus Thierfelder
geboren am 01. Juni 1982 in Rudolstadt

Gutachter:

1. Prof. Dr. Bernd Brüggemann (Friedrich-Schiller-Universität Jena)
2. Prof. Dr. Kostas Kokkotas (Eberhard Karls Universität Tübingen)
3. Prof. Dr. Jose Aantonio Font-Roda (Universität Valencia)

Tag der Disputation: 06. Dezember 2011

Contents

1. Introduction	1
2. Evolution equations	5
2.1. BSSNOK	6
2.2. Gauge conditions	8
2.3. GRHD	9
2.3.1. Conversion between primitive and conservative variables	12
2.3.2. Equation of state	14
3. Initial data	17
3.1. TOV initial data	18
3.2. Boosted TOV initial data	22
3.3. Binary neutron star initial data	24
3.3.1. Numerical method	28
4. HRSC on moving boxes AMR	31
4.1. High resolution shock capturing scheme	31
4.1.1. Reconstruction methods	33
4.1.2. Fluxes	35
4.2. Time integrators	36
4.3. Finite differencing and dissipation	39
4.4. Moving boxes AMR	40
4.5. Vacuum treatment	44
4.6. Boundary condition	45
5. Code validation	47
5.1. Shock tube	47
5.2. Stable TOV	48
5.3. Boosted TOV	56
6. Collapsing TOV stars with puncture gauge	59
6.1. Collapsing spacetime	59
6.2. Comparison with the puncture solution	61
6.3. Behaviour of the matter inside the horizon	65

7. Binary NS	69
7.1. Numerical setup	69
7.2. Dynamics for cold EoS	71
7.3. Effect of different reconstruction methods	78
7.4. Comparison with hot EoS	79
7.5. Evolution with different damping parameters	83
7.6. Gravitational waves	86
7.7. Thermal effects in gravitational waves	94
8. Conclusion	97
A. 3+1 Formalism	101
A.1. 3+1 splitting	101
A.2. Extrinsic curvature	102
A.3. ADM constraint equations	103
A.4. ADM evolution equations	104
B. Global quantities	105
B.1. Total mass and momentum	105
B.2. Gravitational wave extraction	105
B.3. Energy and momentum of gravitational waves	107
C. Different reconstruction methods	109
C.1. MC2	109
C.2. PPM	109
C.3. CENO3	110
List of Publications	112
List of Presentations	113
Bibliography	115
Abbreviations, Acronyms and Notation	129
Acknowledgements	131
Lebenslauf	133
Ehrenwörtliche Erklärung	135
Zusammenfassung	137

1. Introduction

Some of the most interesting predictions of Einstein's theory are the existence of gravitational waves and compact massive objects like black holes and neutron stars. It is known that neutron stars exist in the universe. They were first predicted by Bade and Zwicky in 1934 [16] and first observed by Hewish et al. in 1967 [92]. Our understanding of these objects is, however, very poor. Studying collapsing stars or orbiting binary systems will allow us to understand the underlying structure much better. Information of the dynamics and the extracted gravitational waves will shed light on physics inside the star as described by the equation of state.

The detection of gravitational waves will allow a new understanding of the nature of the universe. However, the detection is a challenging task since these waves are very weak. In order to observe predicted waves a detector's sensitivity has to be good enough to measure a relative length change of less than 10^{-21} . According to [154] there exist several sources of noise like ground vibrations and thermal noise which have to be overcome to reach the necessary accuracy. However, the ground-based interferometric detectors [2, 4, 182, 171] have already entered this sensitivity regime and it is only a matter of time until actual waves will be observed. Since the measured signals from the detectors are hidden inside the noise, from the data analysis point of view it is crucial to generate template banks for gravitational wave and have a better theoretical understanding of the emission mechanisms.

The strongest sources are very compact and fast moving objects like black holes and neutron stars. For ground-based interferometers of present and future generation [37, 13, 1] binary neutron stars (BNS) are among the most promising sources of gravitational waves. Gravitational waves emitted during their inspiral and merger are expected to give unique information about the nature of matter at very high densities and temperatures, which is largely unknown, e.g. [142]. These binaries are also the origin of powerful electromagnetic astrophysical phenomena, in particular short-gamma-ray-bursts (SGRBs) [103, 131]. On the other hand SGRB are ultra relativistic

outflows expected to be produced during the post-merger phase [148, 149, 144] of rapidly spinning, strongly magnetized proto-neutron stars [124]. So far there exist no fully consistent simulation of a SGRB and it is currently under investigation (see for example [144, 98]).

Due to the complexity of the problem only numerical relativity can provide a complete theoretical modeling of the late inspiral and merger. In comparison to binary black hole (BBH) simulations, BNS simulations have been investigated for a longer time. The first numerical relativity simulation of BNS was performed in [164], several years before a generic BBH-system could be stably evolved [140, 30, 55]. At present there are a number of groups performing BNS simulations [72, 71, 125, 12, 184, 109, 77].

Electromagnetic fields in numerical relativity have been considered in [109, 11, 76, 77, 144] and were found likely to be relevant for SGRB and other astrophysical scenarios. However, simulations showed that the effects on gravitational waves during the inspiral phase can be neglected [11, 76, 77]. Thus, until now only the ideal general relativistic magneto-hydrodynamic (GRMHD) framework is used in full general relativistic numerical simulations.

In general BNS studies are based on the GRMHD equations coupled to 3+1 hyperbolic formulations (BSSNOK [129, 162, 34, 130] or GHG [107]) of general relativity. To model the interior of the neutron stars most results are based on a simplified treatment like an ideal gas, polytropic or piecewise polytropic equation of state (EoS). On the other hand in [163] (and following works) a realistic EoS with zero temperature is employed. Nevertheless thermal effects are expected to play a dominant role during the post merger phase and are treated in an approximate way by using a hybrid EoS [163, 36]. The focus on micro-physics is done by e.g. [150, 151, 135] which is important in order to model SGRBs. Other physically important point are transport phenomena and neutrinos [174, 158, 157] which are currently not implemented in full general relativity simulations.

Some of the aspects mentioned here are well understood, other aspects like the influence of micro-physics on the post-merger phase, the initial configuration space or waveforms have to be investigated further. The latter is a crucial point for gravitational wave detection. In comparison to accurate BBH waveforms (see e.g. [95, 86]) the accuracy of waves produced by BNS simulations is yet only poorly investigated [22]. Collaboration between the numerical relativity and analytical relativity communities

has started recently [142, 93, 63, 18, 19]. Investigations regarding the convergence of the waveforms and precise error estimates have not been done in detail yet.

The aim of the present thesis is to use astrophysically relevant initial data which solve the Einstein equations on the initial hypersurface to study collapse of a neutron star as well as binary neutron star systems with a free evolution scheme. In particular the evolution of irrotational neutron star initial data configurations without electric fields are investigated, from which gravitational waves are extracted. During this work I extended the BAM code [52, 54, 49] which was originally designed for numerical studies of multiple black holes spacetimes with adaptive mesh refinement techniques. In order to solve the full Einstein equations we upgraded the BAM code to solve the flux-conservative Eulerian formulation of ideal general relativistic hydrodynamics equations [31] which are coupled to the existing vacuum equations. The extension allows us to handle different kinds of equations of state in a hybrid form composed of a cold part and a thermal part modeled with an ideal gas EoS [163, 36]. We extract gravitational waves from the evolved spacetime and compare them for different resolutions and equations of state.

The structure of the thesis is as follows: The evolution system for the vacuum part and the hydrodynamic evolution equations are presented in chapter 2. A brief introduction of different astrophysically relevant initial data configurations is given in chapter 3.

In order to integrate the evolution system several numerical methods are applied to achieve accurate results. A small collection of methods used in BAM, like the high resolution shock capturing (HRSC) to handle shocks and the mesh-refinement technique to handle large scale grid configurations, are presented in chapter 4. In addition the time integrators used and boundary conditions are discussed briefly.

The validation of the matter implementation is presented in chapter 5. Here the HRSC technique is verified by using the shock tube test. The hydrodynamic code implementation is tested by simulating a static matter configuration. Convergence and conservation of the model is investigated. The coupling between the vacuum and matter parts of BAM is tested using boosted neutron star initial data.

The collapse of a perturbed neutron star to a black hole with the puncture gauge is investigated in chapter 6. The spacetime of the collapse is compared with the puncture spacetime. It is shown why and in which way the matter disappears from the numerical grid.

Finally in chapter 7 binary neutron star systems are studied. The dynamics of the neutron stars for different resolutions and numerical methods are discussed. Gravitational waves for cold and hot EoS are presented and analyzed.

In chapter 8 all results are summarized and discussed.

2. Evolution equations

Einstein equations can be solved as an initial value problem, by introducing the 3+1 decomposition of the spacetime and casting them in a PDE system. A popular strategy used in numerical relativity is to consider free evolution. In this approach the constraints are solved in the initial slice (at $t = 0$) and are not enforced during evolution. Due to the Bianchi identity it is guaranteed that the constraints are always satisfied up to numerical errors. In order to have a well-posed initial value problem the PDE system has to be strongly or symmetric hyperbolic. Evolution equations for the gauge quantities α and β^i have to be specified since these are not prescribed by Einstein equations. This fact comes from the gauge freedom of the theory. The 3+1 splitting of the spacetime is presented in Appendix [A](#) which results in the ADM equations [\[15\]](#). These equations are expressed only in terms of quantities which are defined on a given spatial hypersurface.

Independently of the choice of gauge, the ADM equations are found to be weakly hyperbolic. This leads to numerical instabilities. Thus, other formulations are preferred in numerical relativity. In this chapter we describe the BSSNOK [\[129, 162, 34, 130\]](#) system and the gauge conditions typically used with it.

The field equations for the metric are coupled to the general relativistic hydrodynamic (GRHD) equations describing the matter as a relativistic fluid. GRHD equations follow from the local energy and barionic mass conservation and are typically written in first order conservation formulation. As in classical fluid dynamics the conservative form of the equations guarantee that the numerical scheme will converge to the “physical” solutions, i.e. entropy satisfying weak solutions.

2.1. BSSNOK

The BSSNOK method is based on a conformal decomposition of the ADM evolution system. The spacial metric γ_{ij} is conformally decomposed as

$$\tilde{\gamma}_{ij} = e^{-4\phi} \gamma_{ij}. \quad (2.1)$$

Here $e^{-4\phi}$ is called the conformal factor, which is strictly positive and it is chosen such that the conformal metric $\tilde{\gamma}_{ij}$ has determinant one, that is

$$e^\phi = \gamma^{1/12}, \quad (2.2)$$

where γ is the determinant of γ_{ij} . Additionally, the extrinsic curvature K_{ij} is split into a trace and trace-free part by

$$A_{ij} = K_{ij} - \frac{1}{3} \gamma_{ij} K. \quad (2.3)$$

It turns out that conformally transforming the trace free part of the extrinsic curvature is a ‘‘convenient choice’’ [162, 34]. Therefore one uses a transformation

$$\tilde{A}_{ij} = e^{-4\phi} A_{ij}, \quad (2.4)$$

as for the conformal metric. An important point of the BSSNOK formalism is the introduction of three auxiliary variables known as the conformal connection functions defined by

$$\tilde{\Gamma}^i = \tilde{\gamma}^{jk} \tilde{\Gamma}_{jk}^i = -\partial_j \tilde{\gamma}^{ij}. \quad (2.5)$$

The separate evolution of these functions simplifies the computation of the Ricci tensor. The second derivatives of the metric can be expressed in terms of the evolved conformal connection functions, with the addition of the scalar Laplacian of the conformal metric. Thus, the evolution equation (2.9) is closer to being hyperbolic which leads to more robust system [9, 7].

The five variables ϕ , K , $\tilde{\gamma}_{ij}$, \tilde{A}_{ij} and $\tilde{\Gamma}^i$ are called the BSSNOK variables. Now using these redefinitions and plugging them into the ADM evolution equations (A.18) give us evolution equations for the new system. The resulting system turned out to be more

stable than the ADM equations and do not show violent instabilities. This was first shown numerically by Baumgarte and Shapiro [35]. Note that in comparison with the ADM system the BSSNOK system has more variables, therefore the numerical cost of evolving the system is increased.

In [55], where the ‘moving puncture’ technique was introduced to simulate binary black holes, the conformal factor ϕ has been substituted in the evolution system by the variable χ , defined by

$$\chi = e^{-4\phi}. \quad (2.6)$$

With this redefined conformal factor the BSSNOK evolution system can be written as

$$(\partial_t - \mathcal{L}_\beta)\chi = \frac{2}{3}\alpha\chi K, \quad (2.7)$$

$$(\partial_t - \mathcal{L}_\beta)\tilde{\gamma}_{ij} = -2\alpha\tilde{A}_{ij}, \quad (2.8)$$

$$\begin{aligned} (\partial_t - \mathcal{L}_\beta)\tilde{A}_{ij} &= \chi[-D_i D_j \alpha + \alpha(R_{ij} - 8\pi S_{ij \text{ ADM}})]^{\text{TF}} \\ &\quad - \frac{1}{3}\tilde{\gamma}_{ij}\alpha(16\pi\rho_{\text{ADM}}) + \alpha\left(K\tilde{A}_{ij} - 2\tilde{A}_{ik}\tilde{A}_j^k\right), \end{aligned} \quad (2.9)$$

$$\begin{aligned} (\partial_t - \mathcal{L}_\beta)K &= -D^i D_i \alpha + \alpha\left(\tilde{A}_{ij}\tilde{A}^{ij} + \frac{1}{3}K^2\right) \\ &\quad + 4\pi\alpha(\rho_{\text{ADM}} + S_{\text{ADM}}), \end{aligned} \quad (2.10)$$

$$\begin{aligned} \partial_t \tilde{\Gamma}^i &= 2\alpha\left(\tilde{\Gamma}_{jk}^i \tilde{A}^{jk} - \frac{3}{2\chi}\tilde{A}^{ij}\partial_j \chi - \frac{2}{3}\tilde{\gamma}^{ij}\partial_j K - \frac{8\pi}{\chi}j_{\text{ADM}}^i\right) \\ &\quad + \tilde{\gamma}^{ik}\partial_j \partial_k \beta^j + \frac{1}{3}\tilde{\gamma}^{ij}\partial_j \partial_k \beta^k + \beta^j \partial_j \tilde{\Gamma}^i \\ &\quad - \tilde{\Gamma}^j \partial_j \beta^i + \frac{2}{3}\tilde{\Gamma}^i \partial_j \beta^j - 2\tilde{A}^{ij}\partial_j \alpha. \end{aligned} \quad (2.11)$$

This is the system we are using for all numerical simulations performed by BAM. There are several implementation details due to the usage of constraint equations in the evolution equations (see [52]). The combination of all these choices improves the stability of the code. The system has been successfully used in various simulations of vacuum spacetimes by many groups, e.g. [140, 29, 55] as well non-vacuum spacetimes [12, 184, 109, 77]. The matter terms used are defined in equation (2.28).

2.2. Gauge conditions

Using the above evolution system gives us an evolution equation for each of the BSS-NOK variables. But there are still no equations for the lapse and the shift which appear inside (2.7)-(2.11). They are free specifiable equations, and determine the evolution of the coordinates.

Their aim should be to choose “good” gauge conditions which simplifies the evolution system. The main point is to avoid the formation of coordinate singularities. This can be reached by freezing the time evolution of certain variables or introducing a time delay. Secondly, the gauge conditions should be numerically simple. Having, for example, an elliptic condition on the gauge generates a high computational effort which should be avoided. A commonly used solution is the Bona-Masso family of slicing conditions [44], which is a generalization of harmonic slicing. The lapse α evolves with a hyperbolic equation and can be evolved in a similar fashion to the metric equations. The general condition for the lapse reads

$$\frac{d}{dt}\alpha = -\alpha^2 f(\alpha)K \quad (2.12)$$

where $f(\alpha)$ is an arbitrary but positive function. One common choice for f is using $f(\alpha) = 2/\alpha$. This is the so-called 1+log slicing condition [45]. Therefore the equation for the lapse is

$$(\partial_t - \beta^i \partial_i)\alpha = -2\alpha K. \quad (2.13)$$

It only depends on the extrinsic curvature and the gauge quantities and is a pure gauge slicing condition, which means it tells how the slice is embedded in the spacetime. Equation (2.13) minimizes the lapse when the extrinsic curvature becomes too big. Therefore the evolution of the slice will slow down before a singularity is reached.

On the other hand the shift does not act on the slicing. It is a condition on the coordinate system inside the slice. It should counteract a rapidly growing or shrinking of the black hole horizon in coordinate space. This is directly related to the effective resolution of the simulation. If one does not impose a shift condition, namely using a vanishing shift vector, time lines tend to fall into the black hole. One common way

to avoid this is to use the "Gamma-driver"¹ condition [9]. There exist at least two common versions which are quite similar to each other. The first equation introduced in [9] tries to find a stationary gauge if the time derivative of $\tilde{\Gamma}^i$ vanishes. This is done by

$$\begin{aligned} (\partial_t - \beta^j \partial_j) \beta^i &= \mu_S B^i, \\ (\partial_t - \beta^j \partial_j) B^i &= \partial_t \tilde{\Gamma}^i - \eta B^i, \end{aligned} \quad (2.14)$$

where η and μ_S are positive parameters. On the other hand one can integrate the equations above and gets only one equation for the shift [185]

$$(\partial_t - \beta^j \partial_j) \beta^i = \mu_S \tilde{\Gamma}^i - \eta \beta^i. \quad (2.15)$$

Both choices give similar results and are successfully used for pure black hole evolutions and relativistic hydrodynamics (e.g. [24, 184]). In our simulations we fixed the μ_S parameter to 3/4 or 1. For the η parameter we always use constant values around $2/M_{ADM}$ depending on the kind of simulation.

The BSSNOK equations (2.7)-(2.11) in combination with the "1+log" slicing condition (2.13) are proven to be strongly hyperbolic [7, 153]. This leads to a well posed initial value problem.

2.3. GRHD

For the matter part of the Einstein equations we have to define a model for the stress-energy tensor. Here we assume a perfect fluid form given by

$$T_{\mu\nu} = \rho h u_\mu u_\nu + p g_{\mu\nu}, \quad (2.16)$$

where ρ is the rest-mass density, ϵ is the specific internal energy, $h \equiv 1 + \epsilon + p/\rho$ is the specific enthalpy, p is the pressure, and u^μ is the 4-velocity ($u^\mu u_\mu = -1$) of the fluid. The total energy density is given by $e = \rho(1 + \epsilon)$. Here dimensionless units $G = c = M_\odot = 1$ are used and will be used in the whole work.

¹From the historical point of view it is often called "Gamma-freezing" condition.

The set of conservation equations for this kind of stress-energy tensor, the conservation law for the baryon number, and the equation of state of the fluid read

$$\nabla_{\mu} T^{\mu\nu} = 0, \quad (2.17)$$

$$\nabla_{\mu} (\rho u^{\mu}) = 0, \quad (2.18)$$

$$P(\rho, \epsilon) = p, \quad (2.19)$$

which in case of flat space are equivalent to the non-relativistic Euler equations. In case of linear systems of hyperbolic equations discontinuities can not arise if smooth initial data is used. However, the hydrodynamic equations above are a nonlinear system and shocks can occur even when starting from smooth initial data. Therefore it can happen that the solution is not differentiable in all regions and the differential equation is not valid. In this case it is necessary to consider generalized solutions of the integral form of the equations i.e. weak or integral solutions [104]. Weak solutions are not unique. The physical unique solutions are selected according to “entropy” criteria.

The Lax-Wendroff theorem says that a numerical scheme for a hyperbolic system of conservation laws converges towards the entropy satisfying weak solution [102, 104]. On the other hand if we have a numerical scheme based on a non-conservative formulation it will converge to the unphysical solution [94] (LeFloch Theorem). Thus we have to use a conserved formulation to obtain the correct solution. Following [31] we rewrite Eq. (2.17) and (2.18) in first-order flux-conservative form

$$\partial_t \vec{q} + \partial_i \vec{f}^{(i)}(\vec{q}) = \vec{s}(\vec{q}), \quad (2.20)$$

by introducing the conservative variables

$$\vec{q} = \sqrt{\gamma} \{ D, S_k, \tau \}, \quad (2.21)$$

where

$$\begin{aligned} D &\equiv W\rho, \\ S_k &\equiv W^2 \rho h v_k, \\ \tau &\equiv (W^2 \rho h - p) - D. \end{aligned} \quad (2.22)$$

The simple physical interpretation of these variables is that they represent the rest-mass density (D), the momentum density (S_k) and an internal energy ($\tau = \rho_{\text{ADM}} - D$) as viewed by Eulerian observers. Above v^i is the fluid velocity measured by the Eulerian observer

$$v^i = \frac{u^i}{W} + \frac{\beta^i}{\alpha} = \frac{1}{\alpha} \left(\frac{u^i}{u^0} + \beta^i \right), \quad (2.23)$$

and W is the Lorentz factor between the fluid frame and the Eulerian observer given by $W = 1/\sqrt{1-v^2}$, with $v^2 = \gamma_{ij}v^iv^j$. The fluxes in Eq. (2.20) are

$$\vec{f}^{(i)} = \sqrt{-g} \left\{ D \left(v^i - \frac{\beta^i}{\alpha} \right), S_k \left(v^i - \frac{\beta^i}{\alpha} \right) + p\delta_k^i, \tau \left(v^i - \frac{\beta^i}{\alpha} \right) + pv^i \right\} \quad (2.24)$$

while the source terms are

$$\vec{s} = \sqrt{-g} \left\{ 0, T^{\mu\nu} (\partial_\mu g_{\nu k} - \Gamma_{\mu\nu}^\delta g_{\delta k}), \alpha (T^{\mu 0} \partial_\mu \ln \alpha - T^{\mu\nu} \Gamma_{\mu\nu}^0) \right\} \quad (2.25)$$

$$\begin{aligned} &= \sqrt{-g} \left\{ 0, \right. \\ &T^{00} \left(\frac{1}{2} \beta^i \beta^j \partial_k \gamma_{ij} - \alpha \partial_k \alpha \right) + T^{0i} \beta^j \partial_k \gamma_{ij} + T_i^0 \partial_k \beta^i + \frac{1}{2} T^{ij} \partial_k \gamma_{ij}, \\ &T^{00} (\beta^i \beta^j K_{ij} - \beta^i \partial_i \alpha) + T^{0i} (2\beta^j K_{ij} - \partial_i \alpha) + T^{ij} K_{ij} \left. \right\}. \end{aligned} \quad (2.26)$$

Above $g \equiv \det g_{\mu\nu} = -\alpha^2 \gamma$ with $\gamma \equiv \det \gamma_{ij}$. From straightforward calculations we obtain the stress-energy tensor as a function of the primitive variables $\vec{w} = \{p, \rho, \epsilon, v^i\}$ and the four metric as

$$\begin{aligned} T^{00} &= \frac{\rho h W^2 - p}{\alpha^2}, \\ T^{0i} &= \frac{\rho h W^2 (v^i - \frac{\beta^i}{\alpha})}{\alpha} + \frac{p \beta^i}{\alpha^2}, \\ T^{ij} &= \rho h W^2 (v^i - \frac{\beta^i}{\alpha})(v^j - \frac{\beta^j}{\alpha}) + p(\gamma^{ij} - \frac{\beta^i \beta^j}{\alpha^2}), \\ T_i^0 &= \frac{\rho h W^2}{\alpha} v_i. \end{aligned} \quad (2.27)$$

With this the standard York-ADM matter variables [185] are easily recovered

$$\begin{aligned}
\rho_{\text{ADM}} &\equiv n^\mu n^\nu T_{\mu\nu} = \rho h W^2 - p = \tau + D, \\
j^i_{\text{ADM}} &\equiv -n^\mu \gamma^{i\nu} T_{\mu\nu} = \rho h W^2 v^i = S^i, \\
S^ij_{\text{ADM}} &\equiv \gamma^{i\mu} \gamma^{j\nu} T_{\mu\nu} = \rho h W^2 v^i v^j + \gamma^{ij} p,
\end{aligned} \tag{2.28}$$

which are used inside the the metric evolution system. Note that the source terms in the BSSNOK equations as in the GRHD equations do not depend on the derivatives of $T_{\mu\nu}$. We only need the derivatives of the metric.

The system in Eq. (2.20) is strongly hyperbolic provided that the EoS is causal (the sound speed is less than the speed of light) [31]. Eigenvalues (in direction x) are given by

$$\lambda_0 = \alpha v^x - \beta^x, \tag{2.29}$$

$$\begin{aligned}
\lambda_\pm &= \frac{\alpha}{1 - v^2 c_s^2} \left[v^x (1 - c_s^2) \pm \right. \\
&\quad \left. c_s \sqrt{(1 - v^2) [\gamma^{xx} (1 - v^2 c_s^2) - v^x v^x (1 - c_s^2)]} \right] - \beta^x.
\end{aligned} \tag{2.30}$$

The quantities in the other directions are obtained by permutation of indexes. In the above the sound speed is defined by

$$\begin{aligned}
c_s^2 &= \left(\chi + \frac{P}{\rho^2} \kappa \right) \frac{1}{h}, \\
\chi &\equiv \frac{\partial P}{\partial \rho}, \\
\kappa &\equiv \frac{\partial P}{\partial \epsilon}.
\end{aligned} \tag{2.31}$$

2.3.1. Conversion between primitive and conservative variables

The conservative variables are evolved by constructing the fluxes at the given time slice. Since the fluxes are computed by using the primitive variables

$$\vec{w} = \{ \rho, \epsilon, p, v^i \}, \tag{2.32}$$

we have to recover \vec{w} from \vec{q} . With the definition of the conserved variables in Eq. (2.22) it is possible to construct the inversion [119, 65, 72, 24]

$$v^i(p) = \frac{S^i}{\tau + D + p}, \quad (2.33)$$

$$W(p) = \frac{\tau + p + D}{\sqrt{(\tau + p + D)^2 - S^2}}, \quad (2.34)$$

$$\rho(p) = \frac{D}{W}, \quad (2.35)$$

$$\epsilon(p) = D^{-1} \left[\sqrt{(\tau + p + D)^2 - S^2} - Wp - D \right]. \quad (2.36)$$

The solution is not explicit. All variables depend on the pressure which is used on the left side too. Once the pressure is known the inversion can be done. The pressure is determined by the EoS looking for the root of the nonlinear algebraic equation

$$f(p) = p - P(\rho(p), \epsilon(p)). \quad (2.37)$$

To determine the root we use a simple Newton-Raphson method

$$p^{\text{new}} = p^{\text{old}} - \frac{f(p)}{f'(p)}, \quad (2.38)$$

which is generally used for this purpose. The derivative of f is given by

$$f'(p) = 1 - \chi \frac{\partial \rho}{\partial p} - \kappa \frac{\partial \epsilon}{\partial p}, \quad (2.39)$$

$$\frac{\partial \rho}{\partial p} = \frac{DS^2}{(D + p + \tau)^2 \sqrt{(D + p + \tau)^2 - S^2}}, \quad (2.40)$$

$$\frac{\partial \epsilon}{\partial p} = \frac{pS^2}{D((D + p + \tau)^2 - S^2)^{3/2}}. \quad (2.41)$$

Since the conserved variables are consistent the scheme is always able to find the corresponding primitive variables. However, for low densities small numerical errors can generate negative arguments inside the square roots or vanishing denominators in the expressions above. In order to prevent unphysical inversion we set atmosphere values whenever we reach the atmosphere level.

Specific procedures can be designed once a specific form of the EoS is given. In the case of a one-parameter EoS, $p = P(\rho)$, the quantities $h = h(\rho)$, $\epsilon = \epsilon(\rho)$, and

$$W = \sqrt{1 + \frac{S^2}{(Dh)^2}}, \quad (2.42)$$

are functions of the density ρ and the conservative variables only. Primitive variables can be computed from the ρ , once the latter is determined by

$$g(p) = W(\rho)\rho - D \quad (2.43)$$

using again a Newton-Raphson root finder and

$$g'(\rho) = W(\rho) - \rho \frac{S^2 h'(\rho)}{W D^2 h^3}, \quad (2.44)$$

$$h'(\rho) = \epsilon'(\rho) - \frac{P}{\rho^2} + \frac{\chi}{\rho}. \quad (2.45)$$

Note that $h'(\rho) = \frac{\chi}{\rho}$ if the principle of thermodynamics at zero temperature is applied.

2.3.2. Equation of state

In order to close the system of hydrodynamic equations we have to use an equation of state (EoS) which gives an algebraic relation between the pressure p , the rest-mass density ρ and the internal energy ϵ . The exact nature of the internal structure of a NS is unknown. There are many attempt to use particle physics to construct EoS models. The latter are provided by tables (e.g. [163]) or phenomenologically constructed by means of a piecewise polytropic EoS [141, 136]. In this work we consider “only” simple analytic EoS. Here we discuss three well known equations of state: dust EoS, a polytropic EoS and an ideal-fluid EoS. These are often used in the literature.

The dust EoS is simply given by the fact that the pressure is everywhere zero. Since dust are non interacting point particles the specific internal energy vanishes too. Therefore we have

$$p = P(\rho(p), \epsilon(p)) = 0, \quad (2.46)$$

$$\epsilon = 0. \quad (2.47)$$

In case of the dust EoS the conserved variable τ vanishes (see equations (2.22) and (2.24)) and the inversion from conservative to primitive is possible analytically without the root finding (2.37). This EoS is used to simulate collapse or collisions of galaxies.

The polytropic EoS is given by

$$p = P(\rho(p), \epsilon(p)) = K\rho^\Gamma, \quad (2.48)$$

$$\epsilon = \frac{K}{\Gamma - 1} \rho^{(\Gamma-1)}. \quad (2.49)$$

characterized by two parameters the adiabatic exponent Γ and the polytropic coefficient K . This EoS is an isotropic EoS and does not simulate thermal effects. It is quasi isotropic. As in the dust EoS, the evolution equation for τ is fulfilled analytically and does not have to be evolved. Since transfer of kinetic energy to thermal energy is not allowed there will be no shock formation. The inspiral phase of binary neutron star simulations is approximately adiabatic from the fluid point of view. So this EoS can realistically describe the matter of the system in this phase.

The ideal-gas EoS is the most general of these three. It is given by

$$p = P(\rho(p), \epsilon(p)) = (\Gamma - 1)\rho\epsilon. \quad (2.50)$$

and allows entropy changes in the fluid. This means that shocks can occur, which makes it more difficult to evolve numerically such configurations.

3. Initial data

In order to solve consistently the initial value problem for Einstein equations, the initial data have to satisfy the constraint equations in Appendix [A](#). The initial data problem [\[61, 78\]](#) amounts to solving the elliptic part of Einstein equations in order to provide (quasi) equilibrium configurations of black holes and neutron stars. Equilibrium configurations are typically characterized by a few parameters like mass, spin, equation of state (EoS) Those values have to be chosen according to astrophysical observations. Initial data for numerical relativity evolutions are selected in this configuration space.

The simplest solution concerning matter is the Tolman-Oppenheimer-Volkoff (TOV) solution. It is an equilibrium configuration describing a static star completely determined by the EoS and the central density (or equivalently the mass). The EoS for a single star in equilibrium is known to be cold since it is the result of a supernova explosion which radiated all heat away. The full solution can be obtained by a straightforward integration of a system of ordinary differential equations discussed below. For a given EoS there exists an equilibrium configuration with a maximal possible mass. This configuration marks the threshold between the stable and the unstable TOV solutions. Unstable models are expected to undergo a non-trivial evolution, e.g. to collapse to a black hole, if perturbed.

After looking at a (stable) TOV star, we will discuss initial data for a boosted star, constructed by performing a Lorentz boost transformation of the TOV data [\[72\]](#). A boosted star has a non-trivial evolution which will be analyzed later in the thesis using different gauge conditions. The evolution of a boosted star also provides a testbed for the high resolution shock capturing (HRSC) algorithm with moving boxes adaptive mesh refinement (AMR).

Finally, quasi-equilibrium initial data for binary neutron stars are discussed. The system has no symmetry, thus the problem has to be treated in three dimensions. The

setup of binary neutron star initial data is complicated by the fact that gravitational radiation does not allow closed orbits, but it circularizes the orbits and causes them to shrink. These requirements are technically realized by imposing an approximately helical symmetry (Killing vector) which becomes exact for infinite separation of the bodies. The constraint system is typically solved in the conformally flat approximation [123]. The fluid describing the matter is assumed to be either a corotational [32, 33, 122, 116, 175] or an irrotational [46, 79, 117, 178, 118, 168, 170, 179, 180] state, because both admit a first integral of motion. In comparison to corotational data, the irrotational model is believed to be astrophysically realistic since the spin period of the neutron stars tend to be larger than the orbital frequency even in late inspiral. In other terms, the time of coalescence due to gravitational radiation is shorter than that of synchronization due to viscosity. Furthermore the temperature of these neutron stars can be neglected since we use data at late inspiral. The time between birth of neutron stars and the merger is very long (10^8 yr). Therefore the stars in equilibrium are described by a cold EoS.

3.1. TOV initial data

To provide equilibrium star initial data we use the Tolman-Oppenheimer-Volkoff (TOV) solution [176]. This is a static, spherically symmetric solution of the Einstein equations for a single star which is fully determined by its central density value ρ_c (or central total energy density e_c).

Consider the line-element in Schwarzschild coordinates $(t, \bar{r}, \theta, \phi)$,

$$ds^2 = -e^{2\phi} dt^2 + \left(1 - \frac{2m(\bar{r})}{\bar{r}}\right)^{-1} d\bar{r}^2 + \bar{r}^2 d\Omega^2, \quad (3.1)$$

with $d\Omega^2 = d\theta^2 + \sin^2 \theta d\phi^2$ and a stress-energy tensor given by

$$T_{\mu\nu} = \rho h u_\mu u_\nu + p g_{\mu\nu} = (e + p) u_\mu u_\nu + p g_{\mu\nu}. \quad (3.2)$$

where $g_{\mu\nu}$ is the metric and u^μ the 4-velocity of the fluid. In combination with the

Einstein equations the hydrostatic equilibrium is given by [56]

$$\frac{dp}{d\bar{r}} = -\frac{(e+p)[m(\bar{r}) + 4\pi\bar{r}^3p]}{\bar{r}[\bar{r} - 2m(\bar{r})]}. \quad (3.3)$$

where the Wigner mass-function $m(r)$ is given by

$$m(\bar{r}) = 4\pi \int_0^{\bar{r}} e\tilde{r}^2 d\tilde{r}. \quad (3.4)$$

In equation (3.3) the relation between the total energy density e and the pressure p is needed. This relation is determined by a particular EoS which closes the system. The final result for the matter fields does only depend on the central value e_c and the EoS.

The metric potential ϕ of Eq. (3.1) is defined by

$$\frac{d\phi}{d\bar{r}} = -\frac{m(\bar{r}) + 4\pi\bar{r}^3p}{\bar{r}[\bar{r} - 2m(\bar{r})]}. \quad (3.5)$$

for a Schwarzschild metric with matter inside the radius R . The boundary conditions are given at the surface of the star, $\bar{r} = R$, defined by $p(R) = 0$. For the metric potential, this amounts to

$$\phi(R) = \frac{1}{2} \ln(1 - 2M/R), \quad (3.6)$$

with $m(R) = M$ coming from the matching of the matter solution inside to the Schwarzschild solution outside.

The constructed spacetime is given in Schwarzschild coordinates. However, for some approximations, isotropic instead of Schwarzschild coordinates are preferred. Therefore we have to perform a coordinate transformation from the Schwarzschild coordinates to isotropic ones. In these coordinates the general line-element is given by

$$ds^2 = -e^{2\phi} dt^2 + e^{2\psi} (dr^2 + r^2 d\Omega^2). \quad (3.7)$$

Now r is the radial component in isotropic coordinates. Comparing both metrics (3.1)

and (3.7) one finds

$$\begin{aligned} e^{2\psi} r^2 &= \bar{r}^2, \\ e^{2\psi} dr^2 &= \left(1 - \frac{2m(\bar{r})}{\bar{r}}\right)^{-1} d\bar{r}^2. \end{aligned} \quad (3.8)$$

Combining these equation one obtains a differential equation

$$\frac{dr}{r} = \left(1 - \frac{2m(\bar{r})}{\bar{r}}\right)^{-1/2} \frac{d\bar{r}}{\bar{r}} \quad (3.9)$$

which has to be solved in order to obtain the isotropic radius $r(\bar{r})$ as a function of the Schwarzschild radius. From (3.8), the metric potential $e^{2\psi}$ is given by

$$e^{2\psi} = \frac{\bar{r}}{r}. \quad (3.10)$$

Exterior solution. Solving equation (3.9) outside the star ($\bar{r} > R$) is a straightforward task due to the fact that the mass $m(\bar{r} > R) = M$ is constant. The integration constant can be set by matching both coordinates r and \bar{r} at infinity. Since we are looking for asymptotic flat solutions they have to be identical and one finds

$$r = \frac{1}{2} \left(\sqrt{\bar{r}^2 - 2M\bar{r}} + \bar{r} - M \right). \quad (3.11)$$

Interior solution. For the interior $\bar{r} < R$ the analytic integration of (3.9) is not possible due to the unknown function m which is defined by (3.4). The integration of (3.9) has a singular point at $\bar{r} = 0$ since $m \sim r^3$ for $\bar{r} \rightarrow 0$. The integral can, however, be written as [181]

$$r = C\bar{r} \exp \left[\int_0^{\bar{r}} \frac{1 - \sqrt{1 - 2m/\tilde{r}}}{\tilde{r}\sqrt{1 - 2m/\tilde{r}}} d\tilde{r} \right], \quad (3.12)$$

which is regular at the origin. To obtain the integration constant C one evaluates the exterior solution (3.11) at the star surface $\bar{r} = R$ which yields

$$C = \frac{\sqrt{R^2 - 2MR} + R - M}{2R} \exp \left[\int_0^R \frac{1 - \sqrt{1 - 2m/\tilde{r}}}{\tilde{r}\sqrt{1 - 2m/\tilde{r}}} d\tilde{r} \right]. \quad (3.13)$$

Full solution. The full solution can be constructed by computing the mapping $r(\bar{r})$ for the interior (3.12) and exterior (3.11) parts by simultaneously integrating (3.3) and (3.4). In all these equations we need the central energy density e_c and an EoS which maps between pressure and density. The solution is the radial coordinate and the matter fields (ρ, e, p) in this coordinate system. Finally, one has to use Eq. (3.5) and (3.10) to determine the full line-element.

The calculation of the ADM variables in Cartesian coordinates (used inside evolution equations in chapter 2) is straightforward. All variables depend on the radius only. According to (3.7) the metric components for the Cartesian coordinates are

$$\alpha = e^{2\phi(r)}, \quad (3.14)$$

$$\beta^i = 0, \quad (3.15)$$

$$\gamma_{ij} = e^{2\psi(r)} \delta_{ij}, \quad (3.16)$$

$$K_{ij} = 0. \quad (3.17)$$

Here we used the fact, that, due to the stationarity of the metric and the vanishing shift vector, the extrinsic curvature is vanishing. The matter variables (ρ, e, p) are given by the equations above. The 4-velocity is defined by $u^\mu = (1/\alpha, 0, 0, 0)$.

Properties of a spherical star. The discussed method results in an equilibrium configuration for a given equation of state. The solution space, obtained by varying e_c (or ρ_c) is characterized by stable and unstable branches (e.g. [181]). Fig. 3.1 presents the dependence between mass and radius as between mass and central density for a simple polytropic EoS. While equilibrium sequences can be computed for a very large range of ρ_c corresponding to different star models, we show the part associated with neutron star models. The equilibrium sequence with central rest-mass $\rho_c \in 10^{14..16} \text{ gcm}^{-3}$ has two branches. One is stable, the other is unstable with respect to linear perturbations. The branches are shown in Fig. 3.1 by the different colors, blue for the stable branch, red for the unstable one. Here the maximum denotes the maximum possible mass for this particular EoS, $M_{max} \sim 1.65M_\odot$. A larger gravitational mass can not be obtained due to the fluid pressure. For other EoS the picture changes only quantitatively, in particular the maximum mass is different for different EoS. Additionally, there can be another stable branch for higher densities [88, 126, 14].

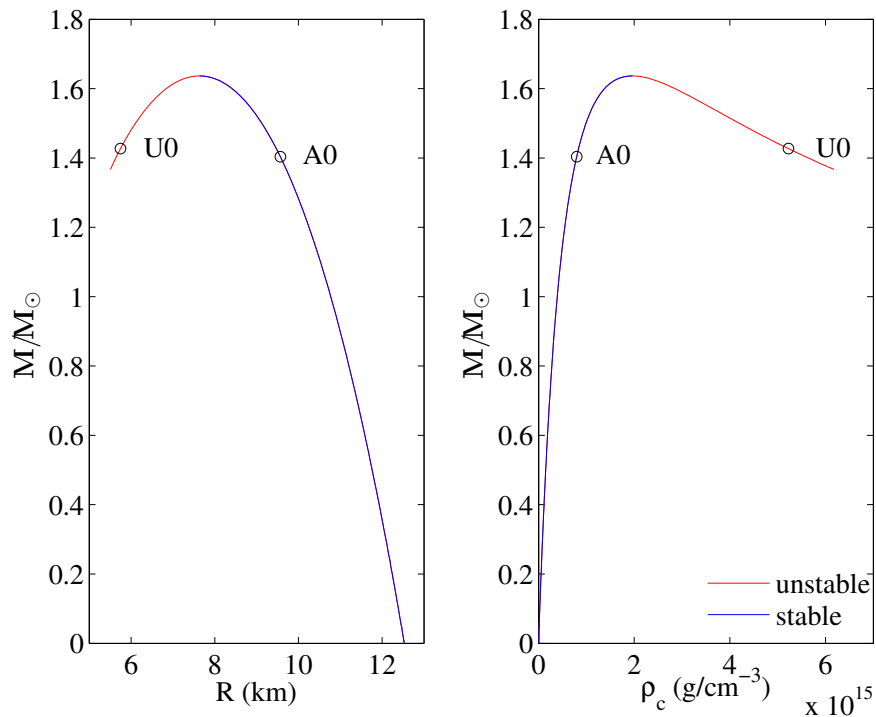


Figure 3.1.: Equilibrium neutron star configurations for polytropic equation of state. The left panel shows the mass of the star normalized by M_{\odot} for given radii. There are no neutron star configurations for too small radii. The right panel shows the mass versus the central density. The blue line denotes the branch where the configuration is stable, whereas the red line denotes the unstable branch. The two configurations U0 and A0 (see Tab. 3.1) are used in chapter 5 and 6.

In case of stable star simulations within this thesis we consider only polytropic EoS. The two initial data configuration we use are marked by a circle in Fig. 3.1, the stable model called A0 and the unstable model U0. The main properties of the initial data are listed in Tab. 3.1.

3.2. Boosted TOV initial data

In order to generate a moving star we use a stable TOV solution boosted by a Lorentz boost in some random direction. The Lorentz-boost in an arbitrary direction is given

Table 3.1.: Initial data used in single-star evolutions. Columns: name, EoS, gravitational (ADM) mass M (see Appendix A), rest-mass M_0 , equatorial proper radius R , angular momentum J scaled by the square of the ADM mass, central rest-mass density ρ_c . Polytropic models are computed with $\Gamma = 2$ and $K = 100$.

Name	EoS	M/M_\odot	M_0	R (km)	J/M^2	ρ_c (gcm $^{-3}$)	r_p/r_e
A0	polytropic	1.400	1.506	9.586	0	0.79×10^{15}	1
U0	polytropic	1.448	1.506	5.838	0	4.94×10^{15}	1

by

$$\begin{bmatrix} t' \\ x' \\ y' \\ z' \end{bmatrix} = \begin{bmatrix} \gamma_b & \gamma_b \xi_x & \gamma_b \xi_y & \gamma_b \xi_z \\ \gamma_b \xi_x & 1 + \frac{(\gamma_b - 1)\xi_x^2}{\xi^2} & \frac{(\gamma_b - 1)\xi_x \xi_y}{\xi^2} & \frac{(\gamma_b - 1)\xi_x \xi_z}{\xi^2} \\ \gamma_b \xi_y & \frac{(\gamma_b - 1)\xi_x \xi_y}{\xi^2} & 1 + \frac{(\gamma_b - 1)\xi_y^2}{\xi^2} & \frac{(\gamma_b - 1)\xi_y \xi_z}{\xi^2} \\ \gamma_b \xi_z & \frac{(\gamma_b - 1)\xi_x \xi_z}{\xi^2} & \frac{(\gamma_b - 1)\xi_y \xi_z}{\xi^2} & 1 + \frac{(\gamma_b - 1)\xi_z^2}{\xi^2} \end{bmatrix} \begin{bmatrix} t \\ x \\ y \\ z \end{bmatrix}, \quad (3.18)$$

where ξ_i is vector pointing in the direction of the boost. The Lorentz-factor according to the boost is given by $\gamma_b = 1/\sqrt{1 - \xi^2}$ with $\xi^2 = \xi_x^2 + \xi_y^2 + \xi_z^2$. Now the Lorentz-boost mixes space and time components, which has an effect on all variables. Since the boost is applied on the full four dimensional metric, the shift vector, the extrinsic curvature and the fluid velocity of the boosted TOV star will not vanish any longer. The new tensors can be computed by the simple coordinate transformation

$$g_{\mu'\nu'}(t', x', y', z') = \frac{\partial x^\alpha}{\partial x^{\mu'}} \frac{\partial x^\beta}{\partial x^{\nu'}} g_{\alpha\beta}, \quad (3.19)$$

$$u^{\mu'}(t', x', y', z') = \frac{\partial x^{\mu'}}{\partial x^\alpha} u^\alpha, \quad (3.20)$$

$$p(t', x', y', z') = p, \quad (3.21)$$

$$\epsilon(t', x', y', z') = \epsilon, \quad (3.22)$$

$$\rho(t', x', y', z') = \rho. \quad (3.23)$$

The extrinsic curvature can be computed from its definition using the transformed variables,

$$\begin{aligned}
-2\alpha K_{ij} &= \partial_t \gamma_{ij} - \partial_i \beta_j - \partial_j \beta_i + 2^3 \Gamma_{ij}^k \beta_k \\
&= \partial_0 g_{ij} - \partial_i g_{0j} - \partial_j g_{0i} + 2\beta_k \frac{\gamma^{kl}}{2} (\partial_j \gamma_{il} + \partial_i \gamma_{jl} - \partial_l \gamma_{ij}) \\
&= -\alpha^2 g^{00} (\partial_0 g_{ij} - \partial_i g_{0j} - \partial_j g_{0i}) \\
&\quad + 2\alpha^2 \frac{g^{0l}}{2} (\partial_j g_{il} + \partial_i g_{jl} - \partial_l g_{ij}) \\
&= 2\alpha^2 \frac{g^{0\sigma}}{2} (\partial_j g_{i\sigma} + \partial_i g_{j\sigma} - \partial_\sigma g_{ij}) = 2\alpha^2 \Gamma_{ij}^0,
\end{aligned} \tag{3.24}$$

which leads to

$$K_{ij} = -\alpha \Gamma_{ij}^0. \tag{3.25}$$

The transformation law of the Christoffel symbols is well known (see e.g. [6]),

$$\begin{aligned}
\Gamma_{\mu'\nu'}^{\sigma'}(t', x', y', z') &= \frac{\partial x^{\sigma'}}{\partial x^\gamma} \frac{\partial x^\alpha}{\partial x^{\mu'}} \frac{\partial x^\beta}{\partial x^{\nu'}} \Gamma_{\alpha\beta}^\gamma + \frac{\partial x^{\sigma'}}{\partial x^\gamma} \frac{\partial^2 x^\gamma}{\partial x^{\mu'} \partial x^{\nu'}} \\
&= \frac{\partial x^{\sigma'}}{\partial x^\gamma} \frac{\partial x^\alpha}{\partial x^{\mu'}} \frac{\partial x^\beta}{\partial x^{\nu'}} \Gamma_{\alpha\beta}^\gamma.
\end{aligned} \tag{3.26}$$

The second part vanishes due to the fact that the boost is a linear transformation.

3.3. Binary neutron star initial data

The construction of binary neutron star initial data has been investigated by many groups [32, 122, 116, 175, 46, 79, 178, 118, 170]. The Meudon group provides a large number of relevant initial data configurations for two neutron stars with different masses, separations and equation of states [69]. All data we are considering here are computed by LORENE [80, 169]. They are constructed with the assumption that the spacetime is conformally flat and the fluid in a quasi-equilibrium irrotational or corotational configuration.

We restrict our investigation to irrotational configurations because, as mentioned before, they are astrophysically most relevant. The stars are set on circular orbits by

imposing an approximated helical killing vector. The fluid equilibrium is obtained from the local energy conservation equations ($\nabla^\mu T_{\mu\nu} = 0$) together with the irrotational and helical symmetry assumption.

Helical symmetry Binary neutron stars during the inspiral stage at a separation of about 50 km are expected to be approximately in equilibrium, and the orbits are close to circular [43]. These assumptions can be translated to the existence of a helical Killing vector field l^μ for the spacetime geometry. In particular, assuming helical symmetry means to neglect ingoing and outgoing gravitational waves. Considering binary neutron star data with an exact Killing vector would violate asymptotic flatness. Since we want asymptotic flatness to hold, we will not obtain an exact solution for the Killing vector. Since gravitational reaction shows up at 2.5 post-Newtonian (PN) order, our solution will be exact up to 2PN order. The helical Killing vector field is given by [46, 79]

$$l^\mu = k^\mu + \Omega m^\mu \quad (3.27)$$

where Ω is the orbital angular velocity with respect to an inertial observer at infinity. The vector k^μ is timelike far away from the binary and coincides with the four velocity at infinity. The vector m^μ , on the other hand, is spatial for closed (exactly circular) orbits and vanishes on the rotation axis.

In the 3+1 formulation the Killing vector can be expressed by

$$l^\mu = \frac{\partial}{\partial t} + \Omega \frac{\partial}{\partial \phi} = \alpha n^\mu - \beta^\mu + \Omega m^\mu, \quad (3.28)$$

where n^μ is the normal vector and m^μ is a spacelike normalized vector which has closed orbits. Here β^i is defined as the shift vector inside the non-moving coordinate system and Ω is identified with the orbital velocity. The shift vector for the co-orbiting coordinates is then

$$B^\mu = \beta^\mu - \Omega m^\mu \quad (3.29)$$

and the Killing vector can be expressed by

$$l^\mu = \alpha n^\mu - B^\mu. \quad (3.30)$$

The Killing vector l^μ is required to be a symmetry generator for the matter as well as for the metric.

Irrotational flow The energy-momentum conservation equation $\nabla^\mu T_{\mu\nu} = 0$ is equivalent to the uniformly canonical equations of motion [106, 57, 173]

$$u^\mu \nabla_\mu (hu_\nu) + \nabla_\nu h = 0, \quad (3.31)$$

$$\nabla_\mu (nu^\mu) = 0, \quad (3.32)$$

where u^μ is the 4-velocity and h being the specific enthalpy. We use the baryon density n instead of the density defined by $\rho = nm_B$. Irrotational fluid corresponds to imposing that the vorticity of hu_μ vanishes, $\epsilon_\rho^{\mu\nu} \nabla_\nu (hu_\mu) = 0$, with the Levi-Civita symbol ϵ_{ijk} . Therefore it can be expressed by the gradient of a potential Ψ ,

$$hu_\mu = \nabla_\mu \Psi, \quad (3.33)$$

$$d\Psi = \nabla_\mu \Psi dx^\mu. \quad (3.34)$$

With this potential the equation of continuity for the baryon density can be written as

$$\nabla^\mu \nabla_\mu \Psi + (\nabla^\mu \Psi)(\nabla_\mu \ln(n/h)) = 0. \quad (3.35)$$

The motion of the fluid is fully determined by the scalar potential Ψ .

By definition the Lie derivative of any field along the Killing vector has to vanish

$$\mathcal{L}_l(hu_\mu dx^\mu) = \mathcal{L}_l(d\Psi) = d(\mathcal{L}_l \Psi) = 0. \quad (3.36)$$

Therefore, $\mathcal{L}_l \Psi$ is constant along l^μ . From Cartan's identity [181] we obtain the first integral of motion

$$hu_\mu l^\mu = \text{const}. \quad (3.37)$$

This version for an irrotational flow in presence of a Killing vector was first found by the authors of [57].

Combining the equation of continuity, (3.35), with the first integral of motion, (3.37),

gives an equation for the scalar potential Ψ [46, 79],

$$\begin{aligned} D^i D_i \Psi &= -\frac{1}{n} D^i n D_i \Psi - \frac{hW}{n\alpha} B^i D_i n + \left(D^i \Psi + \frac{hW}{\alpha} B^i \right) D_i \ln h \\ &\quad - D^i \Psi D_i \ln \alpha - \frac{B^i}{\alpha n} D_i (hW) + KhW, \end{aligned} \quad (3.38)$$

where K is the trace of the extrinsic curvature and $W = -u^\mu n_\mu$ is the Lorentz factor of the fluid with respect to Eulerian observer who moves perpendicularly to the spatial slices. This was first found by Teukolsky [173] and Shibata [160] independently.

Conformally flat approximation To benefit from the helicoidal symmetry, we use coordinates which are adapted to the Killing vector l^μ . Therefore, these coordinates are co-orbiting. A next simplification would be to use a conformally flat three-metric. This was first done by Wilson and Mathews [183] and is used to construct binary black hole initial data. In comparison to the standard ADM form (A.5) the line element is now given as

$$ds^2 = (-\alpha^2 + B_i B^i) dt^2 + 2B_i dt dx^i + A^2 \eta_{ij} dx^i dx^j, \quad (3.39)$$

where η_{ij} is the flat three-metric. The spacetime is thus described by only five functions, the lapse α , the co-moving shift B^i and the conformal factor A . Additionally we choose a maximal slice, $K = 0$.

The definition for the extrinsic curvature is given by (A.10) and with the use of the Killing equation we get

$$\begin{aligned} K^{ij} &= -\frac{1}{2} \mathcal{L}_{\vec{n}} \gamma_{\mu\nu} = -\frac{1}{2} \left(\mathcal{L}_{\vec{l}/\alpha} \gamma_{\mu\nu} + \mathcal{L}_{\vec{B}/\alpha} \gamma_{\mu\nu} \right) \\ &= -\frac{1}{2\alpha} (D^i B^j + D^j B^i) \\ &= \frac{1}{2\alpha A^2} \left(\bar{\nabla}^i \beta^j + \bar{\nabla}^j \beta^i - \frac{2}{3} \eta^{ij} \bar{\nabla}_k \beta^k \right). \end{aligned} \quad (3.40)$$

Using the quantities $\chi \equiv \ln \alpha$ and $\sigma \equiv \ln(A\alpha)$ we can write rewrite the Hamilton

constraint (A.12) and the trace of the Einstein equations as two new elliptic equations

$$\bar{\Delta}\chi = A^2 K_{ij} K^{ij} - \bar{\nabla}_i \chi \bar{\nabla}^i \sigma + 4\pi A^2 (E + S), \quad (3.41)$$

$$\bar{\Delta}\sigma = \frac{3}{4} A^2 K_{ij} K^{ij} - \frac{1}{2} (\bar{\nabla}_i \chi \bar{\nabla}^i \chi + \bar{\nabla}_i \sigma \bar{\nabla}^i \sigma) + 4\pi A^2 (S). \quad (3.42)$$

This is also an elliptic equation for β^i . On the other hand the momentum constraint in combination with the relation for the extrinsic curvature (3.40) yields

$$\bar{\Delta}\beta^i + \frac{1}{3} \bar{\nabla}^i (\bar{\nabla}_j \beta^j) = 2\alpha A^2 K^{ij} \bar{\nabla}_j (3\sigma - 4\chi) - 4\pi \alpha A^2 (E + p) v^i. \quad (3.43)$$

Above, $\bar{\nabla}$ is the covariant derivative associated with the three-metric η_{ij} , and $\bar{\Delta} = \bar{\nabla}_i \bar{\nabla}^i$ is the corresponding Laplace operator. According to [46, 79] we use the notation for the fluid energy density $E = W(e+p) - p$, the trace of the stress tensor $S = 3p + (E+p)v^i v_i$ and the fluid 3-velocity $v^i = \nabla^i \Psi / (hW)$. All three expressions are measured by the Eulerian observer. The Lorentz factor given above can be computed according to

$$W = \sqrt{1 + \frac{1}{A^2 h^2} \eta^{ij} \bar{\nabla}_i \Psi \bar{\nabla}_j \Psi} = \frac{1}{\sqrt{1 - v_i v^i}}. \quad (3.44)$$

By introducing $H \equiv \ln h$ and $\zeta \equiv \frac{d \ln h}{d \ln n}$, the equation for the fluid velocity potential (3.38) takes the final form

$$\begin{aligned} \zeta H \bar{\Delta} \Psi &= -\bar{\nabla}^i H \bar{\nabla}_i \Psi - A^2 h W \frac{B^i}{\alpha} \bar{\nabla}_i H \\ &+ \zeta H \left[\bar{\nabla}^i \Psi + A^2 h W \frac{B^i}{\alpha} \right] \bar{\nabla}_i H \\ &- \zeta H \left[\bar{\nabla}^i \Psi \bar{\nabla}^i \sigma + A^2 \frac{B^i}{\alpha} \bar{\nabla}_i (hW) \right]. \end{aligned} \quad (3.45)$$

3.3.1. Numerical method

To solve the realistic binary system in quasi-equilibrium one has to solve the elliptic equations (3.41)-(3.43) for the metric quantities, and equation (3.45) for the velocity potential. To close the system we need an equation of state which provides the quantities n, e and p depending on $\ln h$. The four equations and the EoS together constitute a system of coupled partial differential equations. They are solved iteratively until the

norm of the enthalpy $\ln h$ is smaller than a certain threshold. A detailed description of the method and the implementation can be found in [46, 79]. At a given iteration the following steps are done

- i. Determine angular velocity, the location of the stars and the rotation axes. The location is given by the maximum of the enthalpy, the other two are found by solving the first integral of Eq. (3.37).
- ii. Compute orbital velocity and the velocity with respect to the Eulerian observer.
- iii. Compute the potential Ψ from the Lorentz factor.
- iv. Solve the elliptic equation (3.45) to obtain H .
- v. Compute n, e, p from the EoS and determine the source terms E and S .
- vi. Solve elliptic equations (3.41), (3.42), (3.43) for the metric fields χ, σ and β^i .
- vii. Update all fields by means of the relaxation algorithm: $F^j \leftarrow \lambda F^j + (1 - \lambda) F^{j-1}$ with $\lambda \in [0, 1]$ relaxation factor.

The elliptic PDE system is solved with a multi-domain spectral solver. The code is based on the LORENE library [69] and provided by the NR group in LUTH (Meudon). These initial data represent to date the most accurate computation of equilibrium BNSs and they are publicly available on the web.

4. HRSC on moving boxes AMR

In this chapter we discuss the numerical methods implemented to handle matter in numerical simulations. The fluid motion is treated in an Eulerian framework and solved by mean of a high-resolution-shock-capturing scheme (HRSC) [177, 105]. HRSC schemes are nonlinear grid schemes (either finite differencing or volume) able to capture physical (entropy satisfying [177, 105]) weak solutions of the hydrodynamic equations.

The HRSC method is based on the approximate solution of local Riemann problems using the characteristic structure of the equations. They are the state of the art scheme for GRMHD codes [121, 70]. The HRSC scheme employed here is implemented by the method of lines for the time integration on a 3D Cartesian grid with adaptive mesh refinement (AMR) using the “moving boxes” technique. We describe the time integrators employed and implementation of the AMR grid.

4.1. High resolution shock capturing scheme

We solve the matter equations described above introducing a uniform staggered spatial grid of spacing $\Delta_x, \Delta_y, \Delta_z$, and N_x, N_y, N_z points and consider the semi-discrete form of the equations (2.20) by

$$\frac{d\vec{q}_{ijk}}{dt} = \frac{1}{\Delta x} \left(\hat{f}_{i-\frac{1}{2}} - \hat{f}_{i+\frac{1}{2}} \right) + \frac{1}{\Delta y} \left(\hat{f}_{j-\frac{1}{2}} - \hat{f}_{j+\frac{1}{2}} \right) + \frac{1}{\Delta z} \left(\hat{f}_{k-\frac{1}{2}} - \hat{f}_{k+\frac{1}{2}} \right) + \vec{s}_{ijk} \quad (4.1)$$

where the $\hat{f}_{i\pm\frac{1}{2}}$ (five component vectors) are the numerical fluxes computed from the physical ones in (2.24).

The HRSC method adopted for the computation of the right side of (4.1) is described in [187, 186] and it is based on point values discretization (instead of cell averages), high-order non-oscillatory reconstructions [89, 166, 165] and central schemes [133, 101].

The method consists in essence of two “cores” : a high-order non-oscillatory interpolation of the primitive variables to cell interfaces and a high-order approximation of the flux derivatives obtained taking appropriate (eventually non-oscillatory) numerical derivatives of the inter-cell fluxes to compute the numerical fluxes. Here we use the method at second-order. The flux derivatives procedure is not implemented.

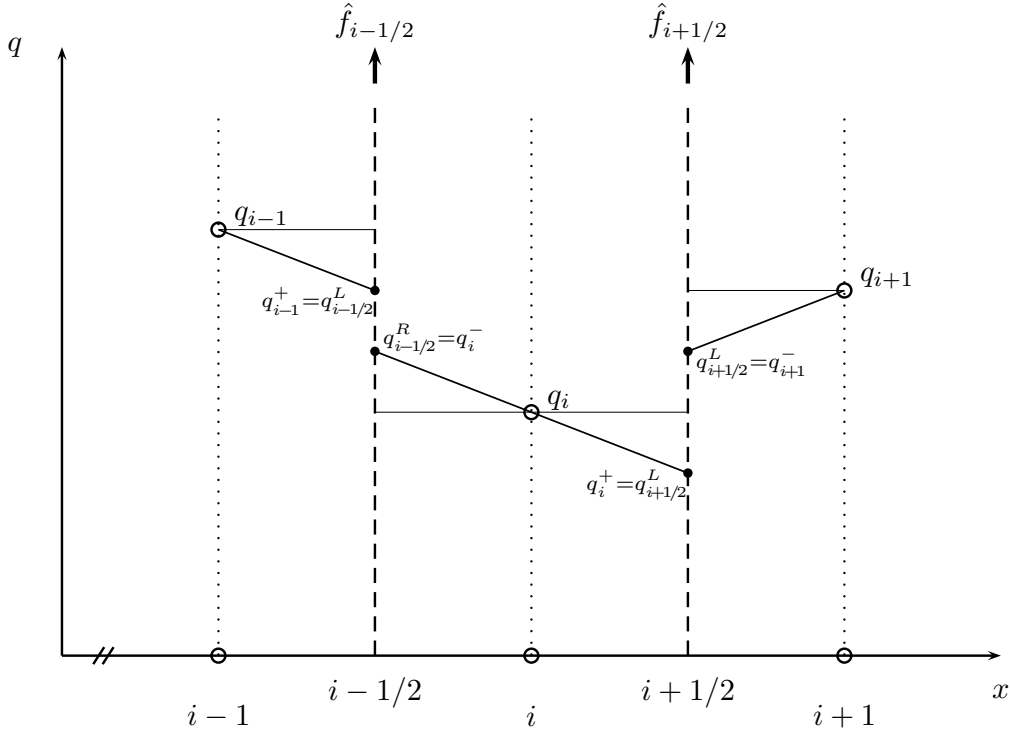


Figure 4.1.: Illustration of the cell and interface labeling.

Since the reconstruction and the fluxes routines operate along one dimension at each time all the computation is in principle one dimensional and can be computed for each direction separately. Note that we have physical points denoted by the letter i and interfaces between the points at $i+1/2$. At each interfaces we have a left state denoted by L and a right state denoted by R . The $+/-$ denotes whether it is the right or left interface value at the point. The basic steps of the algorithm are:

- i. Recovery of the primitive variables \vec{w} from the conservative ones \vec{q}

$$\vec{q}_{ijk} \mapsto \vec{w}_{ijk}, \quad \forall ijk.$$

This is already described in section [2.3.1](#).

- ii. Reconstruction of the primitive variables at interfaces $i + \frac{1}{2}$:

$$\mathcal{R} \left(w_{i-\frac{1}{2}(s-1)}, \dots, w_{i+\frac{1}{2}(s-1)} \right) \mapsto \left\{ \vec{w}_{i+\frac{1}{2}}^L, \vec{w}_{i+\frac{1}{2}}^R \right\}, \quad \forall i = 0, \dots, N_x.$$

where $s = 1, 3, 5, \dots$ is the stencil used. The different methods used (MC2, PPM, CENO3) are described in section [4.1.1](#) and Appendix [C](#). The routines implemented actually reconstruct the cell's edges and store them in vectors \vec{w}_i^\pm such that: $\vec{w}_{i+\frac{1}{2}}^L = \vec{w}_i^+$ and $\vec{w}_{i+\frac{1}{2}}^R = \vec{w}_{i+1}^-$.

- iii. Computation of the numerical fluxes $\hat{f}_{i+\frac{1}{2}}$:

$$\mathcal{F}(\vec{w}_{i+\frac{1}{2}}^L, \vec{w}_{i+\frac{1}{2}}^R) \mapsto \hat{f}_{i+\frac{1}{2}}, \quad \forall i = 0, \dots, N_x,$$

applying approximate Riemann solvers (HLLC [\[90\]](#), LLF [\[133\]](#), [\[101\]](#)) described in section [4.1.2](#). The eigenvalues in [\(2.29\)](#) are used in this step to determine the local characteristic speed(s) used to determine the flux.

- iv. Computation of source terms \vec{s} using [\(2.25\)](#):

$$\vec{w}_{ijk} \mapsto \vec{s}_{ijk}.$$

- v. Time-(sub)-step .

4.1.1. Reconstruction methods

Here the reconstruction methods used are shortly summarized. We implemented three different methods: the Total Variation Diminishing (TVD) linear MINMOD (MM2) and Monotonized Centered (MC2), reconstruction of the Piecewise Parabolic Method (PPM), and Convex-ENO of 3rdorder. The first two are the simplest, where PPM is a standard choice in numerical relativity. The third method is not routinely used in BNS simulations but we found in our case it is the best choice according to the tests in section [5.2](#).

The idea behind the reconstruction is to make an adaptive interpolation which selects the stencil according to the gradient of the solution. As an example we describe the MM2 method. The other methods used are described in Appendix [C](#).

A second order accurate method can be obtained by using a TVD (slope limited) linear reconstruction (Piecewise Linear Method) [177, 105], around the i th point by

$$L_i(x) = w_i + \Delta_i \frac{x - x_i}{\Delta x}, \quad (4.2)$$

where Δ_i is the limited slope. Note that the reconstructed values at the i th cell boundaries $x = x_{i \mp \frac{1}{2}}$ are $w_{i \mp \frac{1}{2}}^R = w_i \pm \frac{1}{2} \Delta_i$. Two ghost zones per side (and per dimension) are required.

The MINMOD function is defined as

$$\text{MM}(a_1, a_2, \dots) \equiv \left\{ \begin{array}{ll} \min_k(a_k) & a_k > 0 \quad \forall k \\ \max_k(a_k) & a_k < 0 \quad \forall k \\ 0 & \text{otherwise} \end{array} \right\}. \quad (4.3)$$

Given the undivided differences at the point i

$$\Delta_i^- \equiv w_i - w_{i-1}, \quad (4.4)$$

$$\Delta_i^+ \equiv w_{i+1} - w_i, \quad (4.5)$$

the MINMOD (MM2) slope is

$$\begin{aligned} \Delta_i &= \text{MM}(\Delta_i^-, \Delta_i^+) \\ &= \begin{cases} \text{sign}(\Delta_i^+) \min(|\Delta_i^-|, |\Delta_i^+|) & \text{if } (\Delta_i^+ \Delta_i^-) > 0 \\ 0 & \text{otherwise} \end{cases} \\ &= \frac{1}{2} [\text{sign}(\Delta_i^-) + \text{sign}(\Delta_i^+)] \min(|\Delta_i^-|, |\Delta_i^+|). \end{aligned} \quad (4.6)$$

The aim of this TVD limiter is to minimize the slope of the given function by choosing the smallest value. This results in numerical dissipation by smoothing the given function. The positive effect is that unwanted oscillations around corners will not be created. In case of extrema the MM2 function gives zero, which results in flattening of a function.

4.1.2. Fluxes

There are two different kinds of fluxes. The hat denotes the numerical fluxes which is an approximation for the physical flux (2.24). The arrow denotes inter-cell fluxes which are the time integral averages of the physical fluxes which are used to construct the numerical fluxes. The inter-cell fluxes $\vec{f}_{i+\frac{1}{2}}$ in equation (4.1) are computed from the reconstructed variables on the left and right of $i + \frac{1}{2}$ using an approximate Riemann solver. We consider the two simplest: the HLLC formula [90, 68], which is a two-wave approximate Riemann solver, and the LLF formula [133, 101, 113], prototype of the central schemes.

To obtain the numerical fluxes $\hat{f}_{i+\frac{1}{2}}$, is necessary to include a certain number of terms depending on $\vec{f}_{i+\frac{1}{2}}$ given by the Taylor expansion of the derivative of \vec{f} up to the right accuracy ¹

$$\Delta x \vec{f}'(x_i) \sim a(\vec{f}_{i+\frac{1}{2}} - \vec{f}_{i-\frac{1}{2}}) + b(\vec{f}_{i+\frac{3}{2}} - \vec{f}_{i-\frac{3}{2}}) + c(\vec{f}_{i+\frac{5}{2}} - \vec{f}_{i-\frac{5}{2}}) + \dots \quad (4.7)$$

where the coefficients are left indicated. In practice the computation of the numerical fluxes reduces to apply some finite differences operators to $\vec{f}_{i+\frac{1}{2}}$:

$$\hat{f}_{i+\frac{1}{2}} = \vec{f}_{i+\frac{1}{2}} + \sum_{j=1}^{(r-1)/2} c_{2j} D^{(2j)} \vec{f}_{i+\frac{1}{2}} \quad (4.8a)$$

$$= \vec{f}_{i+\frac{1}{2}} + \mathcal{O}(\Delta x^2) \quad (4.8b)$$

$$= \vec{f}_{i+\frac{1}{2}} + c_2 D^{(2)} \vec{f}_{i+\frac{1}{2}} + \mathcal{O}(\Delta x^4) \quad (4.8c)$$

$$= \vec{f}_{i+\frac{1}{2}} + c_2 D^{(2)} \vec{f}_{i+\frac{1}{2}} + c_4 D^{(4)} \vec{f}_{i+\frac{1}{2}} + \mathcal{O}(\Delta x^6) \quad (4.8d)$$

with $c_2 = -1/24$ and $c_4 = 3/640$. The operators $D^{(2j)}$ are finite difference operator either based on a fixed central stencil, e.g.

$$D^{(2)} \vec{f}_{i-\frac{1}{2}} = \vec{f}_{i-\frac{3}{2}} - 2\vec{f}_{i-\frac{1}{2}} + \vec{f}_{i+\frac{1}{2}} \quad (4.9)$$

$$D^{(4)} \vec{f}_{i-\frac{1}{2}} = \vec{f}_{i-\frac{5}{2}} - 4\vec{f}_{i-\frac{3}{2}} + 6\vec{f}_{i-\frac{1}{2}} - 4\vec{f}_{i+\frac{1}{2}} + \vec{f}_{i+\frac{3}{2}} \quad (4.10)$$

or decided with a CENO-like algorithm [186, 132]. The computation of the derivatives

¹This step does not appear in the original ENO high-order schemes because reconstruction is done directly on the fluxes. Here we follow [186].

require us to add ghost points in addition to those necessary for the reconstruction procedure (e.g. CENO3 reconstruction and $D^{(4)}$ derivation requires $3+1 = 4$ ghosts per side).

HLLE

The HLLE [90, 68] flux is an approximate Riemann solver which takes into account only the (two) highest speeds of the Riemann

$$\vec{f}_{i+\frac{1}{2}}^{(\text{HLLE})} = \frac{a^+ \vec{f}^L + a^- \vec{f}^R - a^+ a^- (\vec{q}^R - \vec{q}^L)}{a^+ + a^-}, \quad (4.11)$$

where $L(R)$ denotes the physical flux computed from the reconstructed values from the left(right) of $i + \frac{1}{2}$, e.g. $\vec{f}^L \equiv \vec{f}(\vec{w}_{i+\frac{1}{2}}^L)$, and

$$a^\pm \equiv \max \left[0, \pm \lambda_\pm(\vec{w}_{i+\frac{1}{2}}^L), \pm \lambda_\pm(\vec{w}_{i+\frac{1}{2}}^R) \right]. \quad (4.12)$$

LLF

The Local Lax-Friedrichs flux (e.g. [133, 101, 113]) is the most common central scheme. It reads

$$\vec{f}_{i+\frac{1}{2}}^{(\text{LLF})} = \frac{1}{2} \left[\vec{f}^L + \vec{f}^R - a (\vec{q}^L - \vec{q}^R) \right], \quad (4.13)$$

where $a \equiv \max(a^+, a^-)$.

The HLLE flux in (4.11) reduces to the LLF flux if $a^+ = a^-$. The maximal dissipative scheme is obtained for $a = 1$.

4.2. Time integrators

In order to solve our PDE system we use the method of lines (MoL) [155] technique. It allows to separate the time evolution from the spacial discretization. This leads to a system of ordinary differential equations (ODE) which can be integrated by a suitable time integrator under a certain Courant-Friedrichs-Lewy (CFL) condition. Having a

set of coupled ODE's for the time dependence of the variables \vec{u} at a given grid point, the system can be written in the simplified form

$$\partial_t \vec{u} = \vec{f}(t, \vec{u}). \quad (4.14)$$

There exist a large number of different time integrators, for example Euler, Leap-Frog and Rung-Kutta. All are classified by the order of accuracy. The time integrators used in this work belong to the class of explicit Runge-Kutta schemes [3, 75]. They are expected to be the fastest time integrators by giving high accuracy. They are mostly the first choice if one have to integrate a generic system of ODE's since they are easily structured.

Given \vec{u}^n at a fixed time t^n the approximation \vec{u}^{n+1} at the next time step $t^{n+1} = t^n + \Delta t$ is given by s substeps:

$$\vec{k}_1 = \vec{f}(t^n, \vec{u}^n) \quad (4.15a)$$

$$\vec{k}_2 = \vec{f}(t^n + c_2 \Delta t, \vec{u}^n + a_{21} \vec{k}_1 \Delta t) \quad (4.15b)$$

...

$$\vec{k}_s = \vec{f}\left(t^n + c_s \Delta t, \vec{u}^n + \Delta t \sum_{i=1}^{s-1} (a_{si} \vec{k}_i)\right) \quad (4.15c)$$

$$\vec{u}^{n+1} = \vec{u}^n + \Delta t \sum_{i=1}^s (b_i \vec{k}_i). \quad (4.15d)$$

The approximation is determined by the coefficients a_{ij} , b_i and c_i . They can be conveniently written as a table, known as Butcher tableau [139].

$$\begin{array}{c|cccc} 0 & & & & \\ c_2 & a_{21} & & & \\ c_3 & a_{31} & a_{32} & & \\ \vdots & \vdots & \vdots & \ddots & \\ c_s & a_{s1} & a_{s2} & \dots & a_{s,s-1} \\ \hline & b_1 & b_2 & \dots & b_{s-1} & b_s \end{array} \quad (4.16)$$

For our simulations we use two different methods: a third order Runge-Kutta (RK3)

method given by

$$\begin{array}{c|ccc}
 0 & & & \\
 1/2 & 1/2 & & \\
 1 & -1 & 2 & \\
 \hline
 & 1/6 & 2/3 & 1/6
 \end{array} \tag{4.17}$$

which is Heun's third order method [165]. On the other hand we use the standard fourth-order method (RK4)

$$\begin{array}{c|cccc}
 0 & & & & \\
 1/2 & 1/2 & & & \\
 1/2 & 0 & 1/2 & & \\
 1 & 0 & 0 & 1 & \\
 \hline
 & 1/6 & 1/3 & 1/3 & 1/6
 \end{array} \tag{4.18}$$

mainly used since this is method has the highest order for the minimum of substeps.

It is found [165, 145] that third order Runge-Kutta schemes are stable iff $|\frac{\Delta t}{h}c| \leq \sqrt{3}$ and fourth order schemes iff $|\frac{\Delta t}{h}c| \leq 2\sqrt{2}$. This restriction on the time step Δt is called the CFL condition where c is the Courant factor.

For black hole simulations (see [52]) the latter version were used in the past and it can be used for matter simulations as used by [97]. However, it is mentioned in [21, 12] that a third order scheme is more stable and shows better results. The RK3 method satisfies the total variation diminishing (TVD) condition [165], which plays an important role in avoiding spurious oscillations around shocks. The RK4 method on the other hand does not have this property. We tested both mentioned schemes without finding noticeable differences between the results. It was not possible to argue which scheme is the best. The numerical effort between both schemes is approximately the same since we used an optimized RK4 scheme and a generic third-order scheme, which has one step less. We decided to use consistently the RK3 with a Courant factor of 0.25 which leads to convincing results.

4.3. Finite differencing and dissipation

The metric evolution equations (2.7)-(2.11) and the gauge conditions (2.13) and (2.14) are discretized using the standard finite difference technique. The first thing is to approximate the continuum functions by a finite number of values, thus $\vec{u}(t, \vec{x})$ is represented by the values u_{ijk} at a set of discrete points (x_i, y_j, z_k) called the grid. We use the simplest and most general form namely a Cartesian grid with uniform distances between the points in all three dimensions. The differential operators are translated into finite differencing operators by means of Taylor expansions. The first derivative in the x -direction can be obtained by a second order accurate approximation

$$\begin{aligned}
 u_{i+1,jk} &= u_{ijk} + h(\partial_x u)_{ijk} + O(h^2), \\
 u_{i-1,jk} &= u_{ijk} - h(\partial_x u)_{ijk} + O(h^2), \\
 \Rightarrow (\partial_x u)_{ijk} &= \frac{1}{2h}(u_{i+1,jk} - u_{i-1,jk}) + O(h^2) \\
 &= (D_0^i u)_{ijk} + O(h^2).
 \end{aligned} \tag{4.19}$$

The result is a second order accurate centered first derivative where D_0 is the central difference operator. A second derivative needs an additional term in the Taylor expansion

$$\begin{aligned}
 u_{i+1,jk} &= u_{ijk} + h(\partial_x u)_{ijk} + h^2(\partial_x^2 u)_{ijk} + O(h^3), \\
 u_{i-1,jk} &= u_{ijk} - h(\partial_x u)_{ijk} + h^2(\partial_x^2 u)_{ijk} + O(h^3), \\
 \Rightarrow (\partial_x^2 u)_{ijk} &= \frac{1}{h^2}(u_{i+1,jk} - 2u_{ijk} + u_{i-1,jk}) + O(h^2) \\
 &= (D_+^i D_-^i u)_{ijk} + O(h^2).
 \end{aligned} \tag{4.20}$$

denoting by D_+ and D_- the forward and backward difference operator. Note, $D_+ D_-$ is not the same as D_0^2 . A mixed second derivative is created by using D_0 in different directions, e.g. $D_0^i D_0^j = \partial_x \partial_y u$. For our simulations we used fourth order accuracy for the metric evolution equations. These derivatives can be obtained in a similar way by using more points and more terms of the Taylor expansion.

Since all level of the mesh refinement are evolved separately communication between the levels are done by interpolation. This always leads to numerical errors at the box boundaries and a high frequency noise is created. In order to avoid these grid modes

we use artificial dissipation added to the right-hand-sides (RHS) of the time evolution. We only use this for the metric variables. For the matter parts we do not use artificial dissipation at all since the HRSC scheme is dissipative enough that grid modes become measurable. According to [52] we use the standard Kreiss-Oliger dissipation [100, 83] operator Q of order $2r$

$$Q = \sigma \frac{(-h)^{2r-1}}{2^{2r}} (D_+)^r \rho (D_-)^r \quad (4.21)$$

for a $(2r - 2)$ accurate scheme. Here σ denotes the strength of the dissipation and ρ the weight function which is set to identity. Thus the dissipation operator is similar to a $2r$ derivative

$$Q = \sigma \frac{(-h)^{2r-1}}{2^{2r}} (\partial_x^{2r} + \partial_y^{2r} + \partial_z^{2r}). \quad (4.22)$$

4.4. Moving boxes AMR

So far all the discussion did not say anything about the grid structure. A numerical simulation requires the resolution of at least two scales: the strong field region $L \sim M$ and the radiation region $L \sim \lambda_{GW}$. Additional scales are given by unequal mass-ratios for binary simulations and turbulence/micro-physics in case of matter simulations. In absence of symmetries the computational cost for such 3D simulations is large. The absolute computational cost of such a simulation is proportional to the number of point in one dimension to the power of four which unfortunately limits the grid-size to a few hundred points per direction.

Here we avoid this problems by using the adaptive mesh refinement (AMR) technique, where the numerical domain consists of a dynamical hierarchy of uniform grids with increasing resolution and fixed number of points. The numerically important region, which in our case is a neutron star or the black hole, is covered by the highest resolution available on the numerical grid whereas the rest of the grid is resolved less depending on the separation to the objects.

AMR was invented in 1984 by Berger and Olinger [38]. It was first applied to numerical relativity by Choptuik [58] to study the critical collapse of a massless scalar field in spherical symmetry. The AMR used here is described and tested in detail in [54, 48, 50, 52].

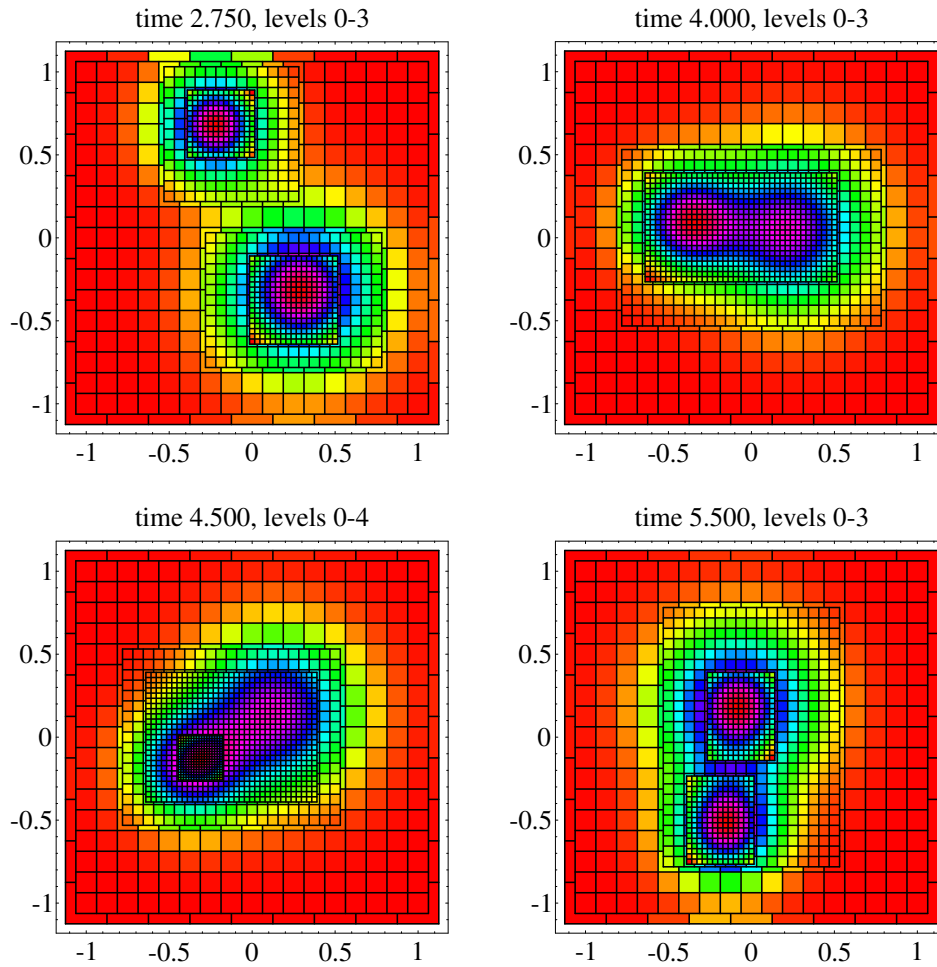


Figure 4.2.: Adaptive mesh refinement example for different grid configuration. The figure is taken from [48].

The numerical domain consists of a set of nested Cartesian grids. The hierarchy consists of $l_{max} + 1$ levels. The level l has the resolution $h_l = h_0/2^l$ and can consist out of one or more Cartesian grids called boxes. The coarsest level l_0 is fixed in space and the physical boundary coincides with the level boundary. All finer levels are able to consist out of several separated boxes which are aligned with the parent box in a coarser level. For simplicity we do not allow overlapping boxes in one level unlike in the original work [38]. If this happens boxes will automatically merge to one extended box covering both. With this technique it is possible to obtain high resolution at several distinct regions on the grid (see Fig. 4.2). The grid is cell centered, there are no points in two different levels which are at the same location. Between the levels

the data is transferred by interpolation (prolongation and restriction). For the metric variables we use standard n -th order Lagrangian interpolation obtained by successive one-dimensional interpolations. Since we can not assume smooth matter functions we use a non-oscillatory interpolation (WENO) for the conserved variables described later. The implemented AMR has the possibility to move boxes over the grid to follow the movement of either neutron stars or black holes.

We use Berger-Oliger time stepping which is a recursive process starting at the coarsest level $l = 0$ going successive through all finer levels by

- i. Evolve the actual level l .
- ii. Call twice the recursive function for the next finer level $l + 1$, if the level exists.
- iii. Do prolongation and restriction between the actual level l and the coarser level $l - 1$ by using Lagrange or WENO interpolation, if the level exists.
- iv. Perform a regrid on the actual level l . This includes moving, merging and/or splitting of the boxes in level l depending on the box locations in the finer level $l + 1$. If this is the finest level the locations of the neutron stars or black holes are used. The aim is to use hierarchies as centered as possible.

Note that time stepping is adjusted to the resolution. Therefore, level l is evolved twice as many times as the next coarser level $l - 1$. We use different approaches to follow either black holes or neutron stars. In black hole simulations we integrate the shift function to track the location of the puncture. This is not possible in case of neutron stars. A possibility is to use the maximum of the density to define the center of a neutron star. In order to additionally locate/follow a puncture formed after the collapse we found it convenient to use the minimum of the lapse function to define the center of the neutron star.

According to [156] a constant damping parameter η in (2.14) can cause stability problem due to too large time-steps in the outer region. We cure this by switching off Berger Oliger time stepping at the outer levels, which then allows us to fulfill the stability condition for η .

Finally I comment about the spatial interpolation used for the conservative variables in the mesh refinement, i.e. between levels. A non-oscillatory interpolation is necessary in order to avoid Gibbs phenomenon. Different methods are adopted in different codes, see e.g. [132, 27]. I implemented a fourth and sixth order WENO algorithm as described in [114]. Since I try to use fourth order everywhere I restricted myself to using fourth

order WENO consistently. The one dimensional scheme is summarized in the following. Given the four points $x_{i-1}, x_i, x_{i+1}, x_{i+2}$ and the corresponding data $f_{i-1}, f_i, f_{i+1}, f_{i+2}$, two candidate interpolating polynomials are constructed as

$$\begin{aligned} p_1(x) &= f_i + \frac{f_{i+1} - f_{i-1}}{2h}(x - x_i) + \\ &\quad \frac{f_{i+1} - 2f_i + f_{i-1}}{2h^2}(x - x_i)^2, \\ p_2(x) &= f_i + \frac{-f_{i+2} + 4f_{i+1} - 3f_i}{2h}(x - x_i) + \\ &\quad \frac{f_{i+2} - 2f_{i+1} + f_i}{2h^2}(x - x_i)^2. \end{aligned} \quad (4.23)$$

The final interpolated value is given by

$$p(x) = w_1(x)p_1(x) + w_2(x)p_2(x), \quad (4.24)$$

where the weights are

$$w_i = \frac{\alpha_i(x)}{\alpha_1(x) + \alpha_2(x)}, \quad (4.25)$$

$$\alpha_i = \frac{C_i(x)}{(\varepsilon + IS_i)^2}. \quad (4.26)$$

The weights are defined in term of the smoothness indicators

$$\begin{aligned} IS_1 &= \frac{25}{12}f_{i+1}^2 + \frac{64}{12}f_i^2 + \frac{13}{12}f_{i-1}^2 + \\ &\quad \frac{26}{12}f_{i+1}f_{i-1} - \frac{52}{12}f_i f_{i-1} - \frac{76}{12}f_{i+1}f_i, \\ IS_2 &= \frac{25}{12}f_i^2 + \frac{64}{12}f_{i+1}^2 + \frac{13}{12}f_{i+2}^2 + \\ &\quad \frac{26}{12}f_{i+2}f_i - \frac{52}{12}f_{i+2}f_{i+1} - \frac{76}{12}f_{i+1}f_i. \end{aligned} \quad (4.27)$$

and the optimal weights

$$C_1(x) = \frac{x_{i+2} - x}{3h} \quad (4.28)$$

$$C_2(x) = \frac{x - x_{i-1}}{3h}. \quad (4.29)$$

In case the of a smooth function, the interpolation reduces to standard fourth order Lagrangian interpolation. For less regular functions the order of interpolation drops based on the local continuity of the derivatives (see discussions in e.g. [96, 172]). In the implementation we set $\varepsilon = 10^{-6}$ to avoid division by zero. The algorithm has been slightly modified in order to enforce monotonicity in the solution [184]. If $p_i(x)$ at a given point is larger or smaller than all four function values f , we set the corresponding α_i to zero. If all α_i are zero we use linear interpolation instead.

4.5. Vacuum treatment

A difficult part of hydrodynamic evolutions is outside the matter, i.e. in the vacuum region. Since the density is going to very small values or even vanish the conversion from conserved variables to primitive variables described in subsection 2.3.1 is singular.

A correct, general and robust solution is not currently available even without the complication of dynamical spacetimes. A standard approach, largely employed in the literature, is instead to substitute the vacuum with a minimal atmosphere of density several orders of magnitudes smaller than the typical densities in the system. Since the density is quite small the resulting effect of the atmosphere on the star should be negligible. In case of neutron stars things are complicated by the presence of gravity and of a stiff fluid.

I implemented a simple vacuum algorithm based on a cold and static atmosphere. The main ideas come from [72, 65, 24]. It consists of the following main prescriptions:

- i. The atmosphere density value, $\rho_{\text{atm}} \equiv f_{\text{atm}} \max \rho$, is chosen as a fraction, f_{atm} , of the maximum density.
- ii. The atmosphere pressure and internal energy are chosen according to the cold (polytropic) part of the EoS of the evolved fluid. In terms of the dust EoS the internal energy is always set to zero.
- iii. The atmosphere velocity v^i is zero.
- iv. The atmosphere is added to initial data in vacuum regions before starting the time evolution.
- v. During the evolution, while recovering the primitives variables, a point is set to atmosphere if it is below a threshold density, $\rho_{\text{thr}} \equiv f_{\text{thr}} \rho_{\text{atm}}$.

Typical values used are $f_{\text{atm}} = 10^{-10}$ and $f_{\text{thr}} = 10^2$. In all my tests I found it general and robust enough for our purposes.

4.6. Boundary condition

All numerical simulations are performed on numerical grids with finite size. Since computational resources are limited it is mostly not possible to disconnect the boundary from the physically interesting domain. In order to deal with this issue there exist several strategies.

One option is by using a compactified coordinate system to spatial-infinity, which is used in the generalized harmonic evolutions in [140]. Another way is to use hyperboloidal slices going to null-infinity [189, 146, 74]. Both techniques have the advantage that the exact Minkowski boundary condition can be employed. However both conditions show numerical complications when following outgoing waves.

A simpler way is by using a boundary enclosing a finite region. Finding a boundary condition in this case satisfying all conditions for the evolution system is not straight forward. The weak-field Einstein equations reduce to a wave equation. Therefore a first naive way to find a boundary condition is by assuming that all fields behave as spherical waves traveling outwards which can be approximated by $f \sim f_0 + u(r - vt)/r$ where f_0 is an asymptotic value for the fields and v is the particular wave speed. In principle one can use this formulation by interpolating the evolved quantities and compute the expected values at the boundary [162]. However, usually one uses a version which is evolved in time [9]

$$\partial_t f + v \partial_r f + v(f - f_0)/r = 0, \quad (4.30)$$

which is the so-called radiative (Sommerfeld) boundary condition. Both methods are analytically similar. However, from the numerical point of view, one will obtain different results due to truncation error.

If the boundary is sufficiently far out it can be approximated as being in flat space-time. Therefore the coordinate speed of light is close to 1 and the velocity can be approximated as the speed of light by $v = 1$. In case of gauge conditions the velocity can be faster than the speed of light. This depend on the particular slicing. For

the Bona-Masso slicing family (see eq. (2.12)) this would be $v = \alpha\sqrt{f(\alpha)}$. Looking at 1+log slicing with $f = 2/\alpha$ the gauge speed for the lapse is $v_\alpha = \sqrt{2}$ in the asymptotic region (where $\alpha \sim 1$) [9]. The longitudinal gauge speed for the shift is given by $v_{long} = 2\sqrt{\mu_S/3}$. Choosing the free function as $\mu_S = 3/4\alpha$ sets this gauge speed to the speed of light.

In order to satisfy the constraints we have to assume that we are in the asymptotic region, where the spacetime is asymptotically flat, the shift is very small and the source of gravitational fields is located in a small region. However, if the constraints are violated, the boundary conditions can have a serious negative effect on stability. There is ongoing work in obtaining better conditions like constraint preserving boundary conditions (see e.g. [147, 39, 152]).

Finally, note that this approach did not include matter parts because the region covered by the matter in our simulations has typically compact support at the center of the computational domain. The matter never comes close to the boundary. Thus it is sufficient to set atmosphere values.

5. Code validation

In order to know whether all components of the hydrodynamic code works correctly I performed a series of test evolutions to validate the code.

First the HRSC is tested with a relativistic one dimensional shock tube in flat space-time. Despite its simplicity, the central scheme for the fluxes capture properly all the elementary waves of the Riemann problem.

Secondly we tested the evolution of a single TOV star with (full-GR) and without (the Cowling approximation) coupling to the metric quantities in order to fine tune the numerical setup to obtain longtime stable simulation. The preservation of the star shape (and of all other fields) and convergence is proved in detail. I tested a boosted TOV star to see how well the code can handle matter dynamics and all couplings between the metric and matter part.

5.1. Shock tube

The first code test is one of the standard tests in fluid dynamics, discussed in e.g. [119]. The fluid is initially separated in to two thermodynamic states on each side of an interface. The system evolves in such a way that three different waves appear, a shock wave, a contact discontinuity and a rarefaction wave. In case of a flat background metric the time-depended problem has an exact solution provided in [121].

The initial states of the Riemann problem is as follows [72]. The left side is specified by $p_L = 13.3$, $\rho_L = 10$, $v_L = 0$ and the right side by $p_R = 0.66 \times 10^{-6}$, $\rho_R = 1$, $v_R = 0$. The domain extends from -0.5 to 0.5 , where the interface is at $x = 0$. As equation of state we use an ideal gas with $\Gamma = 5/3$. Fig. 5.1 shows the numerical and the exact solution at $t = 0.4$ for the shock tube in one dimension. We used 400 grid points and the LLF flux with CENO reconstruction. The exact solution is computed by the code of Marti and Müller [121]. The figure shows good agreement between exact

and numerical solution. All features of the solution, a shock wave (left), a contact discontinuity (center) and a rarefaction wave (right) are well resolved. The same result is obtained in different directions as well as along the diagonal. The HLL did not show major differences. In the following we consistently used the LLF solver.

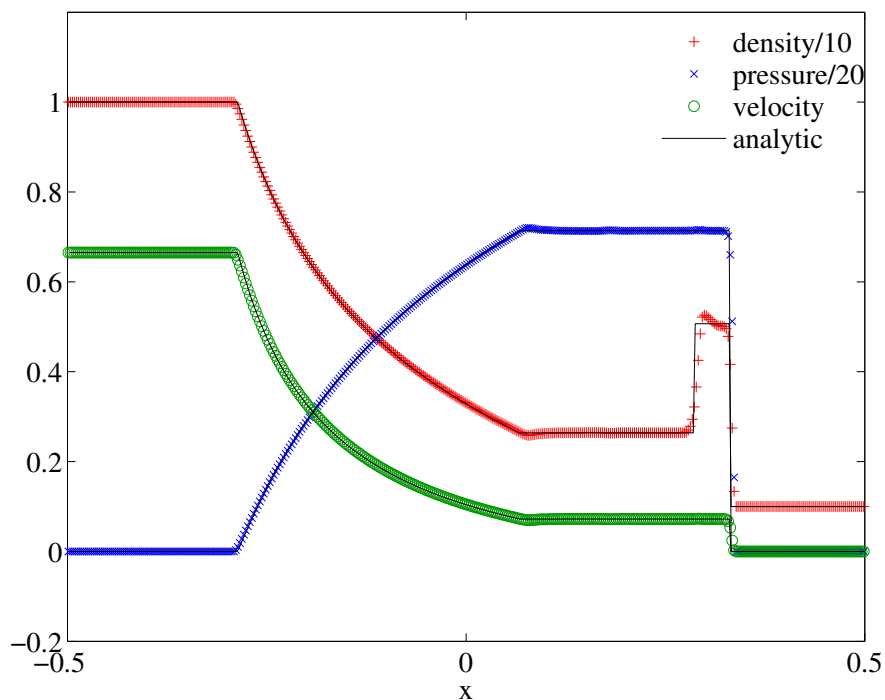


Figure 5.1.: Solution of the shock tube test at $t = 0.4$. The colored signs denote the density, pressure and velocity for the numerical simulation. The black lines correspond to the exact solution.

5.2. Stable TOV

In this part I discuss the simulations of the stable model A0 which I investigated in [MTH2]. The grid is composed of three boxes (two refinement levels), the finest box covers entirely the star. Simulations are performed employing resolutions of $h = 0.295, 0.443, 0.591, 0.738$ km for the finest box and lasts about 10 ms. The model A0 is a stable equilibrium configuration which means that its evolution is trivial. The continuum solution can not evolve, it has to remain at the initial condition. Therefore the dynamics of the numerical solution is governed by truncation errors and spurious

effects due to the usage of an artificial atmosphere. This gives the possibility to study the long term stability and convergence of the code.

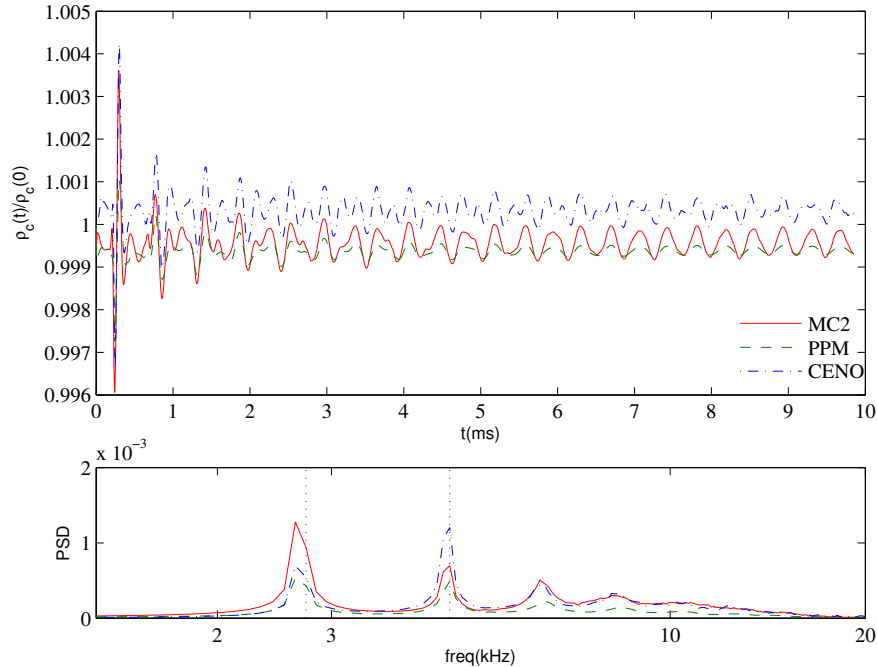


Figure 5.2.: Evolution of the central rest-mass density of model A0. The top panel shows the normalized central density for a stable star simulated with different reconstructions (MC2,PPM,CENO3) in the Cowling approximation. The lower panel presents the power spectrum of all three simulations. The first two perturbative pulsation frequencies are denoted by dotted black lines.

It is well known, e.g. [71], that numerical errors trigger small amplitude pulsations of the star which oscillate at the proper radial mode frequency. The phenomenon is depicted in Fig. 5.2 for the Cowling approximation and Fig. 5.3 for full-GR where the evolution of the central rest mass density normalized to its initial value is shown for different reconstruction schemes and for the highest resolution. The result is similar in both cases but the physical values of the oscillation frequency differ. In the Cowling approximation the result is more stable and truncation errors are smaller. Both figures demonstrate the ability of the code to maintain the initial configuration. For instance the pulsations amplitude is less than 0.5% over 10 ms. The two frequencies shown in the lower panel dominate the pulsations both for Cowling and full-GR. In the Cowling

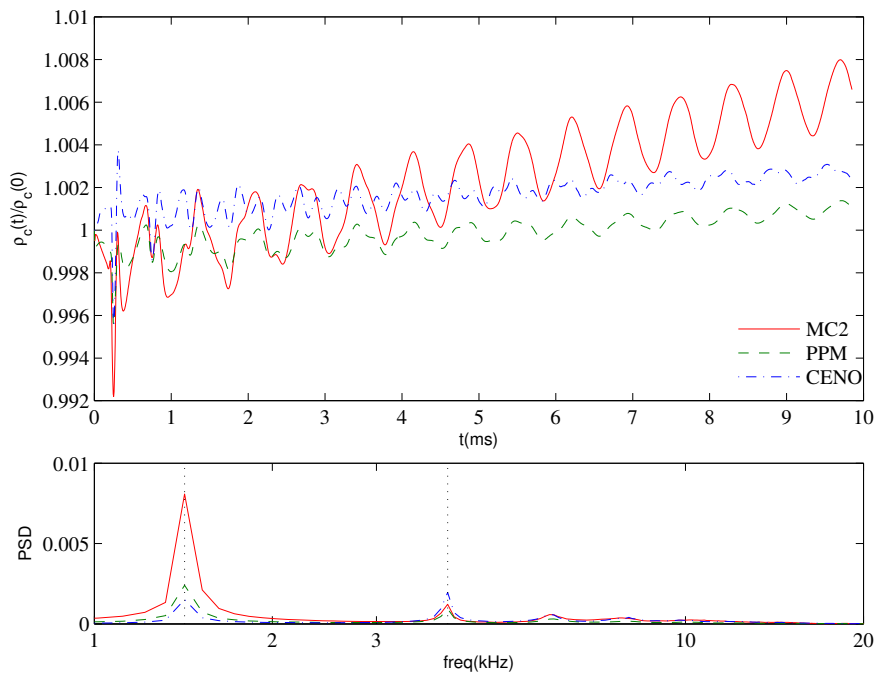


Figure 5.3.: Same plot as Fig. 5.2 but results are computed in full-GR.

approximation we find $\nu_F = 2639$ Hz and $\nu_H = 4568$ Hz, whereas for the general case we get $\nu_F = 1421$ Hz and $\nu_H = 3959$ Hz. They agree within the errors estimated from the output time sampling (2%) with the fundamental radial linear mode and its first overtone as computed by perturbative methods [99, 40]. Both figures highlight that different reconstruction methods (MC2, PPM and CENO) give slightly different results which do not change the physical values. As one can see the peaks of the two dominant frequencies do not change within the error bars. In both figures one can see that the numerical scheme is dissipative, which results in a damping of the pulsation. For all three reconstruction methods the dissipation is in the same order. However, the MC2 scheme shows slightly less dissipation which could be a result from the bigger truncation error.

In case of full-GR (Fig. 5.3) a secular drift of the central density using MC2 reconstruction is observed. A similar drift is observed also in simulations with PPM and CENO at lower resolutions. This secular drift is a feature related to the evolution of the geometry together with the fluid. Looking at simulations in the Cowling approximation (Fig. 5.2) it is or almost absent at all resolutions.

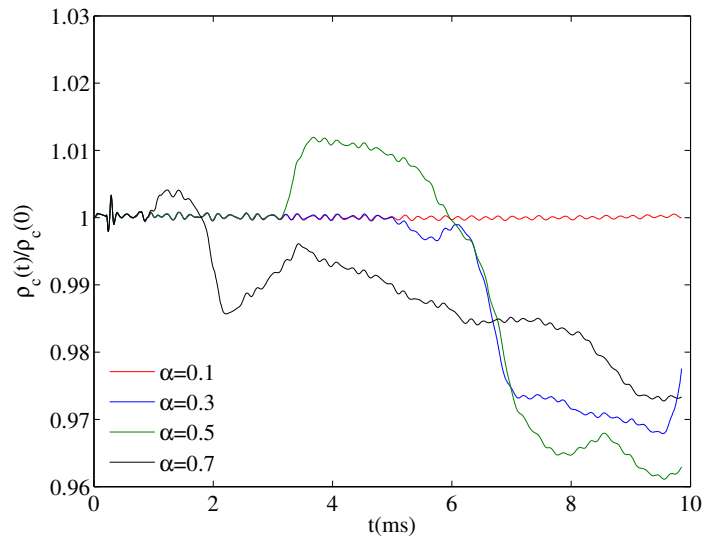


Figure 5.4.: Comparison of the normalized central rest-mass density using CENO reconstruction for different values of the parameter α^0 .

In general the amplitude of the pulsations is also larger in the case of MC2 indicating that truncation errors are bigger, as expected for a linear reconstruction. Notice that in the simulations with CENO reconstruction the overtone of the radial mode at frequency ν_H is more clearly visible. During preliminary tests with CENO reconstruction I observed a loss of stability between 2 and 6 ms depending on the resolution employed. I found that for a compact star solution and a standard implementation of the CENO reconstruction, the limiter tends to select in some points the lower order sub-stencils. A similar effect is also discussed in [12]. The problem is easily fixed in our set up by choosing a different weight in the weighted differences between the linear reconstruction and the quadratic polynomial with centered stencil in equation (C.5). Fig. 5.4 shows the normalized central density for different values of the parameter α^0 with the same resolution as in the previous test. Here we can see that for this resolution $\alpha^0 = 0.1$ is the best choice. Going to lower resolution shows that one can use larger values. I found the value $\alpha^0 = 0.1$ sufficient and robust for all the resolutions and used this value in all problems in this work. In that way the limiter selects the central stencil which corresponds to a higher order stencil, thus minimizing truncation errors. The PPM reconstruction has several free parameters to tune, I did not attempt to do it but instead used the prescription given in [120].

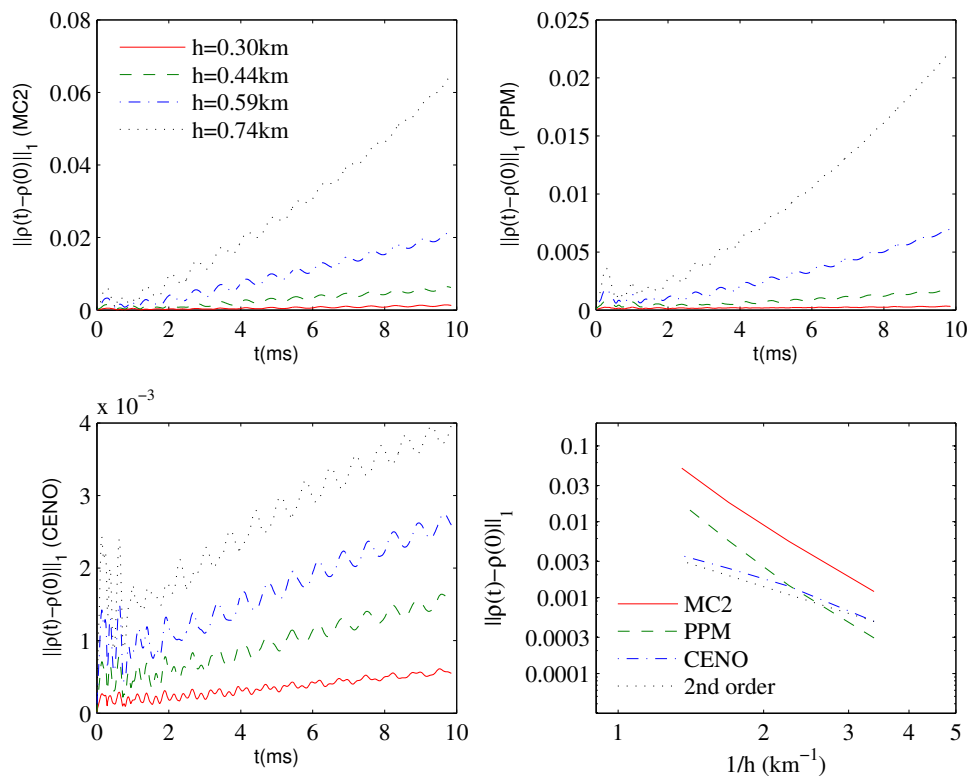


Figure 5.5.: Convergence in L1 norm of model A0. The upper panels and the lower left panel show the L1 distance $\|\rho(t) - \rho(0)\|_1$. Different panels refer to the different reconstruction methods: MC2, PPM and CENO. The lower right panel shows the convergence order for the three reconstruction methods using the highest resolution $h = 0.30$ km and $t = 8$ ms. The black dotted line is the reference for 2nd order convergence.

Figure 5.5 reports the evolution of the L1 distance between the evolved rest-mass density and the initial data. The different curves refer to different resolutions, at every time the difference between the two curves behaves as $\|\rho(t) - \rho(0)\|_1 \propto h^r + \mathcal{O}(h^{r+1})$ since the initial data represents the solution for the evolution problem. The three panels from top left to bottom left refer to different reconstructions. In all cases we observe convergence with increasing resolution. Overall 2nd order convergence is found at early times $t \sim 2$ ms. In principle we expect 2nd order since the matter part is second order accurate for solutions with no shocks. At late times however the MC2 and PPM reconstructions show larger truncation errors. The curves present a quadratic behavior. This leads to apparent over-convergent results, which indicates the simulations are

not yet in the convergent regime. By contrast the use of CENO reconstruction gives 2nd order convergence over the whole simulated time. The last panel (bottom right) summarizes the observed convergence rate by showing in log-log plot the L1 distances as a function of $1/h$ at a given late time $t = 8$ ms for different reconstructions. The slope of the lines gives the convergence rate. The over-convergent behavior for MC2 and PPM as well as the 2nd order convergence of CENO are evident. Note that MC2 and PPM is formal 2nd order and CENO 3rd order. However, the overall convergence order of the used HRSC scheme is “only” 2nd order. Therefore we do not expect higher convergence rates.

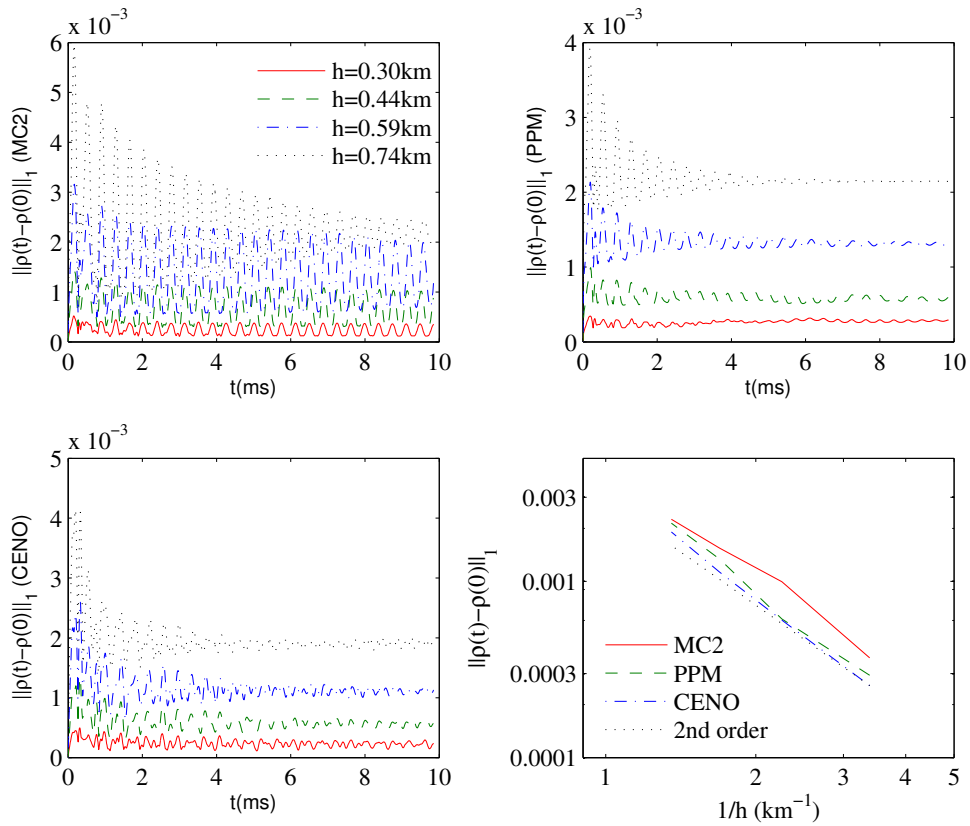


Figure 5.6.: Same plot as Fig. 5.5 but results are computed in the Cowling approximation.

To interpret these results we recall here that in a HRSC scheme the truncation errors strongly depend on the degree of smoothness of the solution and on the specific limiters employed. While the formal convergence rate of the methods employing different reconstruction is the same, the truncation errors for this problem are simply different in

the three cases. PPM and MC2 reconstructions are only first order at smooth extrema thus they are expected to be less accurate on smooth solution than CENO, but more robust in presence of strong shocks. More importantly, the apparent over-convergence behavior is not simply related to the HRSC method employed to solve the GRHD equations but it seems a genuine aspect of evolving the GRHD equations coupled to Einstein equations. To show this we consider Fig. 5.6 which is the same as Fig. 5.5 but in the Cowling approximation. From an inspection of the figure is clear that, once the metric is not evolved, all the reconstructions performs quite similarly showing perfect 2nd order convergence in norm at all times. Specifically one can observe how CENO and PPM have similar performances and with all the reconstructions the convergent regime is reached at the considered resolutions. This means that in case of full-GR the faster convergence observed for MC2 and PPM is a combination of numerical errors from various parts of the algorithm rather than to an effect only related to the reconstruction methods. The rest-mass conservation is guaranteed by the flux-conservative form of the GRHD equations. In all the simulations reported here we observe that the deviation is of the order of $\Delta M_0/M_0 \sim 10^{-6}$.

Due to numerical errors the Einstein constraints are violated independent of the formulation or the method adopted. Having a converging code the constraint violations will be reduced by increasing resolution, but they will never vanish. When free-evolution schemes are adopted, the constraints are only monitored (not solved) and typically the violation (i) grows in time, (ii) converges with increasing resolution. In our simulations we observe this behavior. The biggest violations on the grid are registered in the region covered by the matter and at the boundary since we do not adopt a sophisticated method yet.

Figure 5.7 summarizes this results. The three panels from top-left to bottom-left show the evolution of the L2 norm of the Hamiltonian constraint (A.15) for several resolutions in the cases when MC2, PPM and CENO reconstruction are employed. The violation converges to zero in all the cases. From the figures it is clear that the absolute value of the violation is larger for MC2 and PPM reconstruction while it is about a factor 10 smaller for CENO reconstruction when compared to MC2 and PPM. A summation of effects and errors as the one described above contribute to this behavior. It is difficult to clearly identify them due to the complexity of the equations and the numerical method employed.

The bottom-right panel displays the spatial profile in x -direction of the Hamiltonian

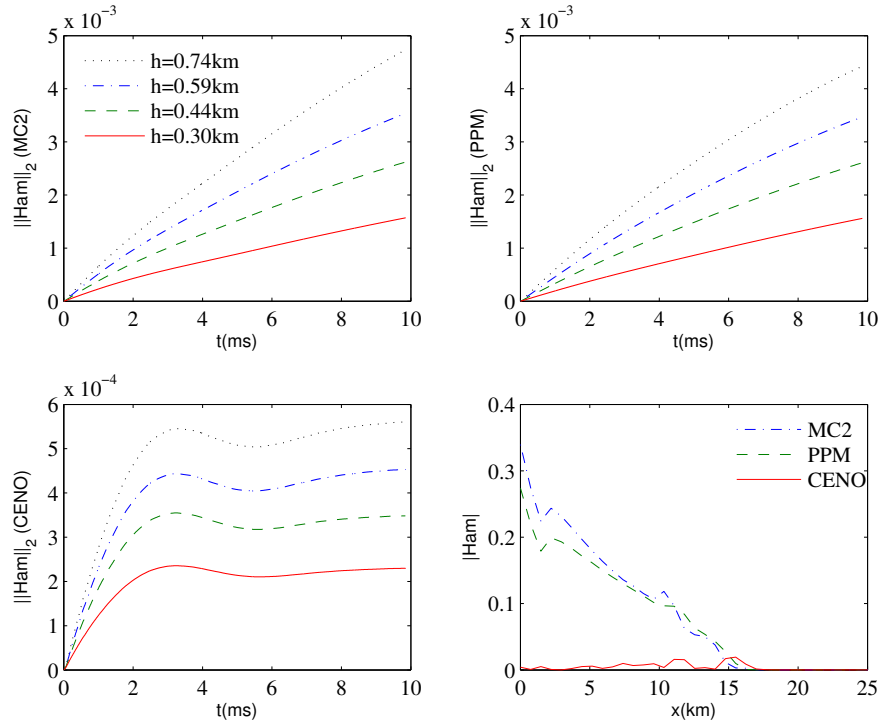


Figure 5.7.: Hamiltonian violation during the evolution of model A0. The first three panels from the top-left to the bottom-left show the time evolution of the 2-norm of the Hamiltonian constraint computed on the finest grid level. Different lines refer to different resolutions $h = 0.295, 0.443, 0.591, 0.738$ km. Different panels refer to the three different reconstructions considered: MC2, PPM and CENO. The last panel shows the profile in x -direction of the Hamiltonian constraint at time $t \sim 10$ ms for the maximum resolution and three reconstructions. Note the different scales of the plots.

constraint at late time, $t \sim 10$ ms, for simulations employing the highest resolution and different reconstruction schemes. The Hamiltonian violation accumulates in time around the region of the matter. Comparing CENO with PPM and MC2 we see that CENO has a better overall performance.

We observe a difference in using mesh refinement or unigrid. In both cases the star is covered by one box with the same resolution, the only difference is that two more boxes are added outside to set the boundary of the computational domain further out ($r_{\text{boundary}} \sim 94$ km for AMR and $r_{\text{boundary}} \sim 23$ km for unigrid). Note that the surface of the star is approximately at $r_{\text{TOV}} \sim 12.5$ km. We observe that for unigrid the norms of the Hamiltonian constraint show an anti-convergence behavior at early times. This

feature is due to the initial non-convergent constraint violation at the boundary which at early times dominates the violation in the interior. The use of mesh refinement is thus very important to minimize the boundary effect.

These tests should convince us to prefer the CENO reconstruction. I stress that if a different setting is used, e.g. a different method to solve Einstein equations, a different numerical flux, much higher resolutions, etc., the whole picture may significantly change.

The constraint accumulation and boundary condition effects discussed here are related to the use of BSSNOK and Sommerfeld boundary condition (see [4.6](#)). They have been pointed out in [\[39, 152\]](#) where the Z4c formulation was proposed as an alternative solution, however, both references are restricted to spherical symmetry.

Furthermore tests for a rotating neutron star were performed. The results are comparable with the literature (see e.g. [\[73, 23, 66\]](#)). However, due to the limitation of the work the results are not included.

5.3. Boosted TOV

Here we discuss the evolution of model A0 boosted in the x -direction at a speed of $v = 0.5$ corresponding to a Lorentz factor of $W = 1.16$. The setup of the initial data is described in chapter [3](#). The test is interesting because it gives the possibility to perform several tests within a simple scenario, namely: (i) fully dynamical and nonlinear evolutions, (ii) the performances of the moving boxes with matter and (iii) different gauge conditions. We use five refinement levels, all except the coarsest are moving and the finest box covers the star entirely. The different resolutions employed for the finest box are $h = 0.306, 0.408, 0.588$ km.

The solution of the evolution problem depends on the gauge conditions employed. If one analytically advects the lapse and shift over the grid, the full solution is just the shifted analytic initial data in space. However, when the conditions in equation [\(2.13\)](#) are applied the solution is not analytic. In order to investigate the numerical solution obtained under the 1+log and Gamma-driver condition we consider evolutions with different values of the parameter η . A similar investigation has been carried out for BNS. Figure [5.8](#) summarises my findings. It shows the profiles of the rest-mass density in x -direction at the final time of $t = 1.72$ ms from evolutions using different values of

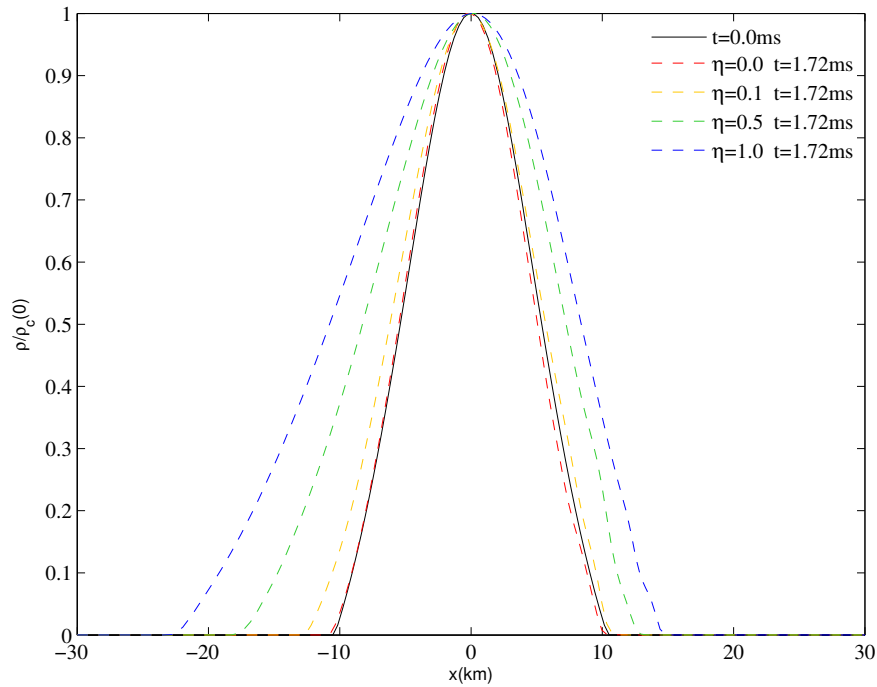


Figure 5.8.: Profile of rest-mass density for the evolved boosted model A0. The picture shows the rest-mass density profile normalized to the initial value at time $t = 1.72$ ms for evolutions corresponding to different values of the η parameter in the Gamma-driver shift condition (dashed colored lines). The profiles are shifted back to the the initial position of the star, the initial data is also plotted (black solid line).

η . All the profiles are shifted back to the initial position of the star by aligning the maximum of the density, the initial profile is also plotted. As apparent from the figure, the choice $\eta = 0$ corresponds to be closest to the analytic solution. For higher values the star profile is progressively more distorted in the direction of motion. Here this does not tell that the solution is wrong. This is only a coordinate effect which will have an effect on the effective resolution of the simulation.

We finally comment about convergence. Figure [5.9](#) shows the point-wise self convergence of the spatial profile of ρ at $t = 3.95$ ms for $\eta = 0$. We show the differences between the rest-mass density profile computed at different resolutions. The difference between the medium and the high resolution is scaled by a convergence factor for 1st(dotted line) and 2nd(dashed line) order convergence. Point-wise convergence is lost at early times and improves with time. However, the magnitude of the errors scales

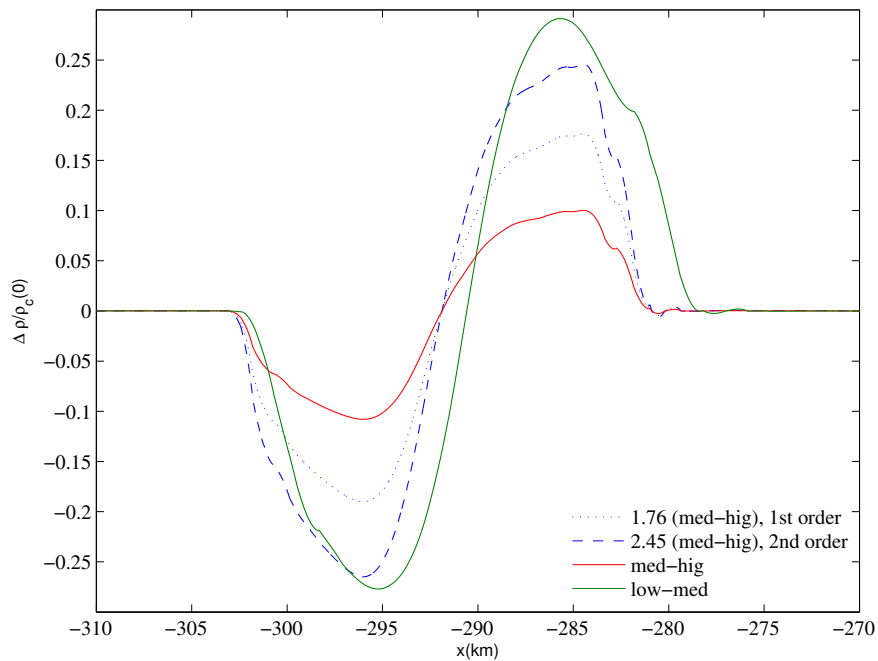


Figure 5.9.: Self-convergence test of the evolution of boosted star. The picture shows the differences between the profiles of the rest-mass density at $t = 3.95$ ms evolved with different resolutions. The labels of the solid lines “low”, “med” and “hig” in the legend correspond to resolutions $h = 0.306, 0.408, 0.588$ km. The difference between medium and high resolution is scaled for 1st (dotted line) and 2nd (dashed line) order convergence. The gamma-driver condition employs $\eta = 0$.

at about 2nd order thus indicating convergence in L1 norm as expected. The same test was done in [72]. In our case the evolution time is a factor about 10000 longer and higher resolution is employed.

6. Collapsing TOV stars with puncture gauge

Simulated binary neutron star systems will arrive at a point where both stars touch and merge to a single star. The final star will eventually become too massive to be stable and therefore it is forced to collapse. Given conservation of momentum quasi-circular binary inspirals will finally create a rapid rotating neutron star. A fraction of these objects are not stable and will collapse to a black hole with roughly the same amount of mass and angular momentum.

From the numerical point of view a single neutron star and a black hole are totally different. The single star has matter placed on a regular spacetime whereas the black hole has a physical singularity without any matter. Here the transition from a star to a black hole has to handle (i) collapsing matter fields onto a single point in combination with a dramatic increase of the values at this location (ii) a physical singularity is formed in the metric fields and (iii) the matter inside the horizon has to vanish from the spacetime and into the singularity.

In this chapter we investigate the simplified problem of a unstable non-rotating neutron star forced to collapse to a Schwarzschild black hole by radial perturbation. We discuss results from [\[MTH1\]](#), adapted to the present context.

6.1. Collapsing spacetime

The collapse of an unstable TOV is triggered by introducing a radial perturbation of the velocity field with an amplitude larger than the truncation errors. Since we are only interested in testing the ability of the code to handle the formation of singularities, to keep the set up simple we do not solve the constraints after imposing the perturbation. From our experience this procedure does not introduce relevant unphysical effects,

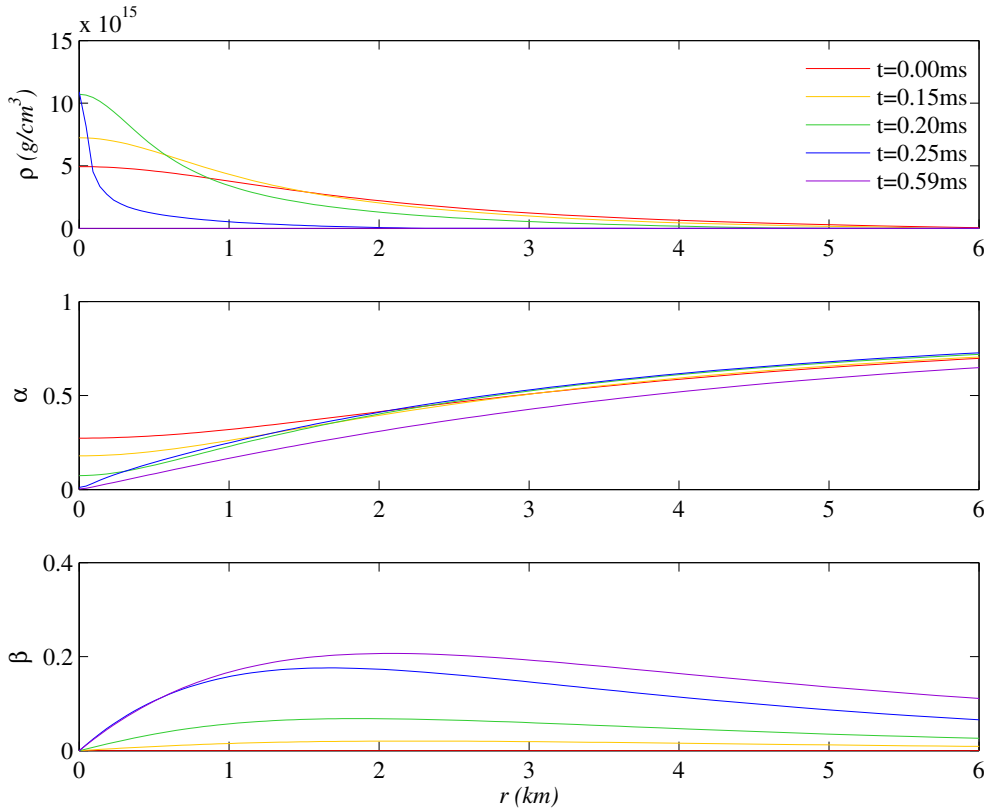


Figure 6.1.: Radial profiles of the rest-mass density ρ (top panel), of the lapse function α (middle panel), and of the shift $\beta \equiv \beta^r$ (bottom panel) at some representative times of the evolution. Note that at $t_{\text{AH}} \sim 0.23 \text{ ms} \sim 35 M$ an apparent horizon is first found and that at $t = 1.47 \text{ ms} = 207 M$ the amount of matter on the final time slice is essentially that in the atmosphere.

while it is clearly an inconsistent way to solve Einstein equations (see also discussions in [24, 25, 12]). Furthermore the results obtained are in close qualitative agreement with [71, 62] where the constraints were solved. To investigate the transition to a black hole we need high accuracy around the center. According to [55] we should use a resolution of at least $h = 1/16M = 0.09 \text{ km}$ to obtain long time stable simulations of the final BH. Therefore we employ eight refinement levels with maximum resolutions of $h = 0.0369, 0.0461, 0.0738 \text{ km}$ at the finest level. The outer boundary is at around 200 km. As initial data we use the unstable star model U0.

The collapse happens in the first 0.3 ms of the simulation. The matter falls towards the symmetry center while the metric varies rapidly adapting itself to the matter distri-

bution. At about $t_{\text{AH}} \sim 0.23 \text{ ms}$ we find an apparent horizon with an initial coordinate radius of $r_{\text{AH}}(t_{\text{AH}}) \lesssim 1.4 \text{ km}$. The larger part of the matter is outside the horizon but is rapidly accreted. Figure ?? shows the evolution of the rest-mass density (top panel), the shift in radial direction (central panel) and the lapse (bottom panel) for different times. The central density increases of a factor two at t_{AH} while the lapse collapses towards zero. After t_{AH} the gauge conditions play the main role in handling the singularity. The final stage is similar to a single black hole, all matter is accreted from the grid.

6.2. Comparison with the puncture solution

Here the question occurs whether the final black hole is the same solution as the end state of an evolved single puncture using the same slicing condition (2.13). Figure 6.2 shows the shape of four different metric components for the collapse of a single TOV star and an evolved puncture. As puncture initial data we use [47] with lapse equal to one and vanishing shift. The evolution of the puncture is described in [87, 85]. Here we plot the trace of the extrinsic curvature (K), the conformal factor (χ), the lapse (α) and the shift (β) in radial direction at the time $t = 1.47 \text{ ms} = 207 \text{ M}$. For convenience we show dimensionless quantities since we want to compare the final states of both simulations which have a different mass. The time is well after the first occurrence of an apparent horizon ($t_{\text{AH}} \sim 0.23 \text{ ms} \sim 35 \text{ M}$). Both solutions have become essentially stationary. Both spacetimes are very close to each other and can not be distinguished close to the center by visual inspection. Going to later times both curves will come even closer. In [MTH1] we did the same comparison with a 1D code [39] code. The results are similar except that the truncation errors are smaller since we used higher accuracy.

In order to have a more quantitative comparison we computed the behavior of the fields in the collapsing spacetime close to the origin and obtained fitting functions for

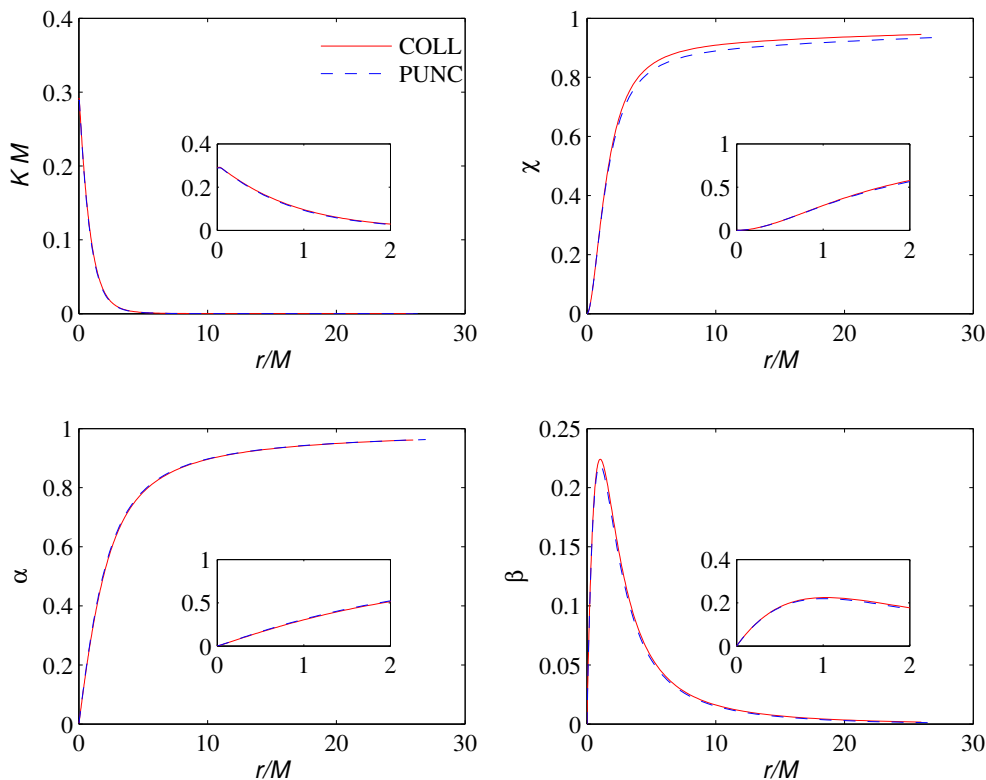


Figure 6.2.: Radial profiles of representative field variables at time $t = 207 M$ of the puncture and the collapsing star. From top left to bottom right: trace of extrinsic curvature (K), conformal factor (χ), lapse (α) and shift ($\beta \equiv \beta^r$).

the stationary solution for $r \ll 1$:

$$K M \sim 0.30 - 0.37 \left(\frac{r}{M} \right), \quad (6.1)$$

$$\chi \sim 1.22 \left(\frac{r}{M} \right)^{2.0}, \quad (6.2)$$

$$\alpha \sim 0.54 \left(\frac{r}{M} \right)^{1.09}. \quad (6.3)$$

The fits for (6.2) and (6.3) contain the exponent of r as a fitting parameter, but not for (6.1). The result agrees well with the corresponding expressions in [51]. In particular, the non-integer exponent for the lapse in (6.3) is very close to the analytic expression for the trumpet solution in isotropic coordinates, which has the exponent 1.091 [51]. This result is non obvious since the numerical coordinates are not isotropic. It seems that the evolution and therefore the gauge condition (2.13) maintain the isotropy from

the initial data.

This result is confirmed when considered also in a coordinate-independent manner. Following the prescription suggested in [87], we analyze the dependence of the lapse versus the extrinsic curvature and report in Fig. 6.3 the differences at different times. More specifically, we show with solid lines the relative difference $\Delta\alpha/\alpha \equiv \alpha_{\text{punc}}/\alpha_{\text{coll}} - 1$, between the lapse of the puncture evolution, α_{punc} , and that of the collapsing star, α_{coll} , either when the apparent horizon has just formed ($t \sim 35$ M) or when the solutions have reached approximately a stationary stage ($t \sim 200$ M).

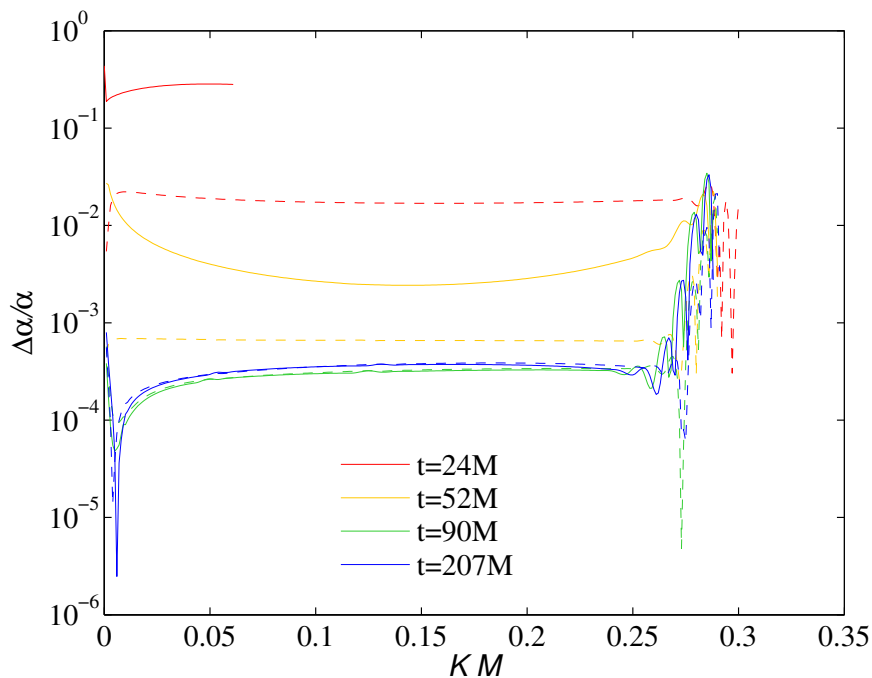


Figure 6.3.: Relative difference $\Delta\alpha/\alpha \equiv \alpha_{\text{punc}}/\alpha_{\text{coll}} - 1$, between the lapse of the puncture evolution, α_{punc} , and that of the collapsing star, α_{coll} , as a function of the trace of the extrinsic curvature, K , at different coordinate times. For a fair comparison, data at the same values of K are found by interpolation. The dashed lines refer to the relative differences between the analytic result and the puncture evolution. By construction, for early times this difference is much smaller than the difference between puncture and matter simulations.

It is clear that the relative difference decreases in time and, at time $t = 207$ M, it is below 1% except for large K . This is the part close to the puncture. Here the errors are large due to the non smooth behavior at the center. By performing

convergence tests we have also determined that the numerical errors are at the same level as the 1% disagreement. Note that after $t = 100$ M the truncation error does not improve further. The truncation does improve by going to higher resolutions (see the 1D case [MTH1]). Also reported in Fig. 6.3 with dashed lines is the relative difference between the puncture data and the analytic solution for the trumpet solution [51, 85]

$$\begin{aligned} K &= \beta\alpha'(R)/2 \\ &= \frac{\sqrt{2/R(\alpha) + \alpha^2 - 1} (4R(\alpha)\alpha^2 - 4R(\alpha) + 6)}{2R(\alpha) (R(\alpha)\alpha^2 - 2R(\alpha)\alpha - R(\alpha) + 2)} , \end{aligned} \quad (6.4)$$

where R is the Schwarzschild radius, α' is the derivative of α with respect to R and we set $M = 1$. Here the relative error at the beginning is much smaller. It becomes comparable with the one computed for the collapsing spacetime at later times.

Looking at the collapsing spacetime the behaviour of the extrinsic curvature around the origin for $t = 207$ M gives

$$K M \sim 0.30 - 0.92 \alpha . \quad (6.5)$$

For the analytic case one has to Taylor expand equation (6.4) around the center which is equivalent to $\alpha = 0$. This is possible by using the implicit function $R(\alpha)$ in [51] and one gets

$$K(\alpha) = 0.300937 - 0.930916\alpha + O(\alpha^2) , \quad (6.6)$$

which closely agrees with equation (6.5) and tells us that the end states of both numerical spacetimes are close to the analytic solution of a trumpet.

Finally we compare directly 1D (spherical symmetric) and 3D results. Fig. 6.4 presents α versus K at $t \sim 200$ M for the puncture and the collapse. The top panel shows that all curves are on top of each other. The lower panel shows the difference between the 1D and the 3D results. The relative error is below 1% and has the largest value at the puncture (small values of α) which is caused by the limited resolution. For larger radii (larger values of α) the difference drops to 10^{-4} . This shows that both versions give similar results.

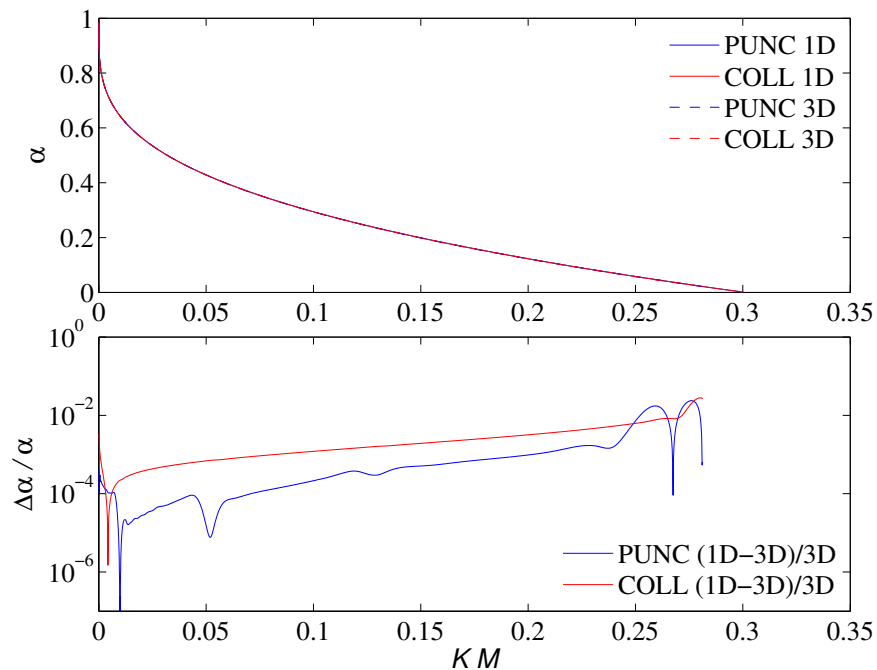


Figure 6.4.: Slicing from 1D and 3D simulations. Top panel: the lapse (α) is plotted versus the trace of the extrinsic curvature K at time $t = 200 M$ for the collapse in 1D (red solid line) and the puncture evolution in 1D (blue solid line), and the collapse in 3D (red dashed line) and puncture evolution in 3D (blue dashed line). The bottom panel shows the relative differences. Note that 1D results, computed on a finer grid, are interpolated for the comparison.

6.3. Behaviour of the matter inside the horizon

The results in the previous section show that the final stage of the collapse and puncture coincides. Looking at the foliation of the spacetime it is geometrically clear that matter will always stay on the slice. However, following the collapse numerically shows that the matter does vanish at a finite time. In order to find out in which way the matter disappears from the grid, we investigated a large range of resolutions in 1D and 3D and experimented with several reconstruction schemes. In these tests only the time of the fluid disappearance changed slightly. Since I use HRSC schemes my numerical methods should be good enough to handle extremely large gradients when the matter piles up. Therefore this cannot explain the matter disappearance.

In order to test whether slice stretching of the spatial coordinates can have an effect

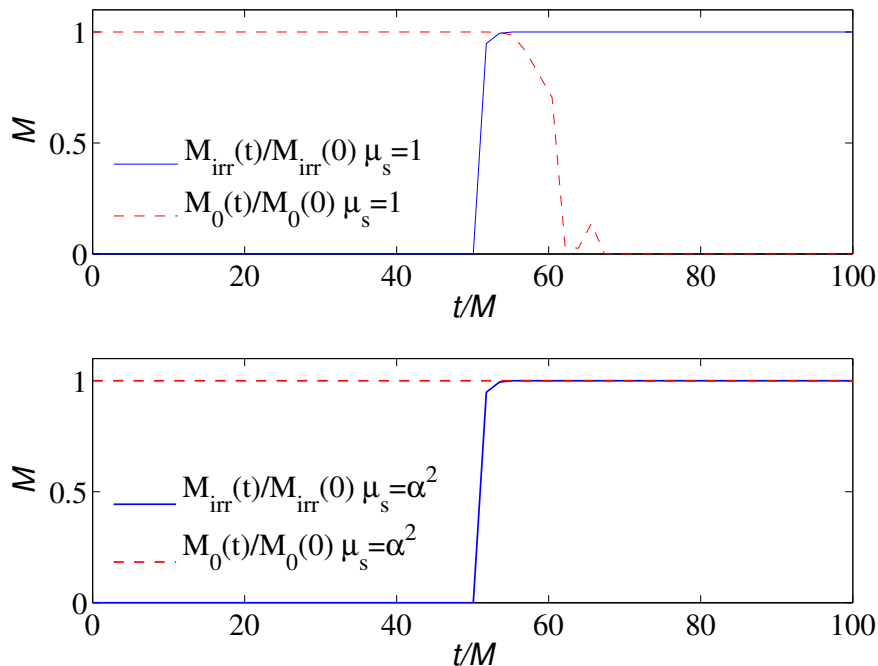


Figure 6.5.: Evolution of total rest-mass, $M_0(t)$, (red lines) and of the irreducible mass, $M_{\text{irr}}(t)$, (blue lines) normalized respectively to the initial value and to the ADM mass. The top panel refers to a simulation with gauge speed $\mu_s = 1$, and the bottom panel to evolutions with gauge speed $\mu_s = \alpha^2$.

in pushing the matter out of the numerical domain I investigated using Gamma-driver conditions. In case of puncture simulations it is well known that grid points are pushed out of the black hole (see e.g. [85]). I performed two different runs with the same slicing condition (2.13) but different shift condition (2.14): once with $\mu_S = 1$ and once with $\mu_S = \alpha^2$ which is similar to $\beta^i = 0$. Here the foliation is not changed since the “1+log” condition I used is a pure slicing condition [5] and is not effected by the radial gauge for the shift. Figure 6.5 shows the total rest-mass and the normalized irreducible mass determined by the apparent horizon [81, 8]. The total rest mass is computed by the conserved variable D integrated over the whole numerical domain. Clearly, while the behavior of the irreducible mass is independent of the choice for μ_S , that of the rest-mass is not. When using the $\mu_S = \alpha^2$ radial gauge, in fact, the matter remains on the numerical grid, so that the rest-mass is conserved well beyond the formation of the apparent horizon. The cause of this difference must therefore to be attributed to the large stretching of the spatial coordinates with $\mu_S = 1$.

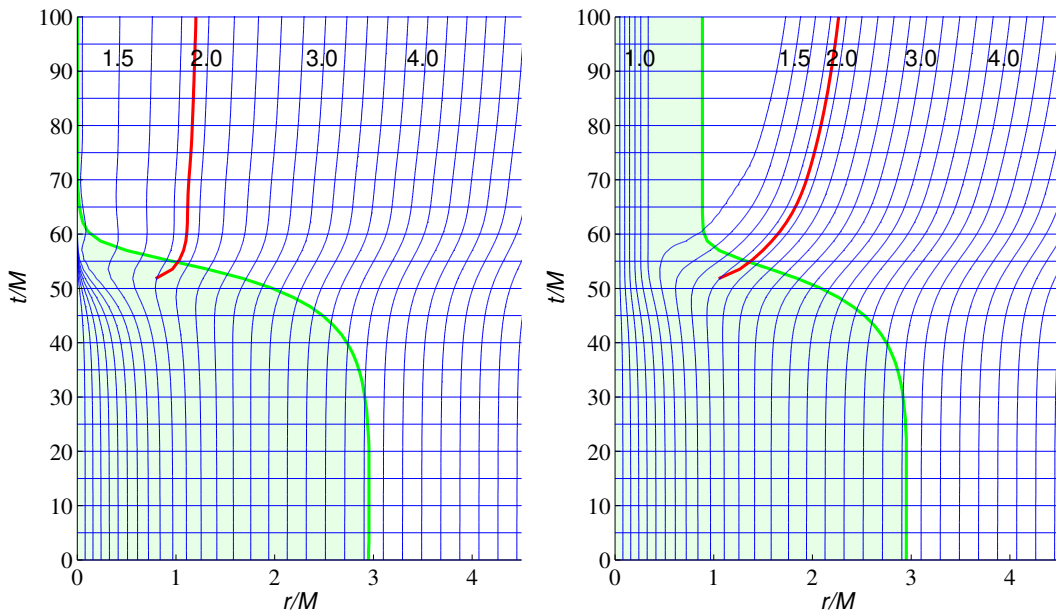


Figure 6.6.: Spacetime diagram of the collapsing star. Data are from 1D simulations with gauge speed $\mu_S = 1$ (left panel) and $\mu_S = \alpha^2$ (right panel). The horizontal blue lines are lines of constant coordinate time. The thick red line denotes the apparent horizon. The vertical blue lines are lines of constant Schwarzschild radius R which values are on top of the lines. The shaded green area bounded by the thick green lines shows the region of the matter.

Finally, Fig. 6.6 shows the spacetime diagrams for both simulation. In order to compute lines of constant Schwarzschild radius we need high resolution all over the numerical domain. Therefore we use simulations in 1D to gain good results. The left panel of Fig. 6.6 is the simulation for $\mu_S = 1$. The shaded green area corresponds to the region of the spacetime covered by matter, vertical lines are line of constant Schwarzschild radius while horizontal lines are lines of constant coordinate time. The thick red line emerging after $t \sim 50 M$ is the apparent horizon. Fig. 6.6 can be compared with other numerically-generated diagrams of collapsing spacetimes obtained either in other gauges [159], or with excision techniques [24], or for puncture evolutions of single black holes [85]. The figure clearly shows how the matter is “squeezed” from the numerical grid when $\mu_S = 1$, while it remains on the grid when $\mu_S = \alpha^2$. In both cases an apparent horizon is found. The comparison of the lines of constant Schwarzschild radius in the two panels highlights the stretching of the spatial coordinate discussed

before.

7. Binary NS

In this chapter binary neutron star systems are investigated. I evolve initial data generated for quasi-equilibrium configurations of irrotational equal-mass binaries in circular orbits. The equations to construct these initial-data are discussed in section 3.3. I discuss results from [MTH2], adapted to the present context. In particular I investigate the dynamics of the neutron stars for different equation of states and different damping parameters. Furthermore, I investigate the extraction of gravitational waves and the influence of the EoS on the waveform.

7.1. Numerical setup

The properties of the initial configuration are summarized in Tab 7.1 and were first computed in [80, 169]. The binary has ADM mass $M = 2.998$, angular momentum $J = 8.836$ and proper separation $d \simeq 36.582$ (54 km), thus the compactness of the system is $M/d \simeq 0.08$. The coordinate separation is 30.457 (45 km). The rest-mass and ADM mass of each star in isolation ($d \rightarrow \infty$, spherical configuration with same central rest-mass density) are $M_b = 1.625$ and $M_\star = 1.456$, respectively. Note the notation for the rest-mass of the star in isolation, M_b , and for the rest-mass of the binary, M_0 . The compactness of each star in isolation is $M_\star/R = 0.14$.

Table 7.1.: Parameters of the initial binary configuration. Columns: ADM mass M , rest mass M_b and ADM mass M_\star of each star in isolation, angular momentum J scaled by the square of the ADM mass, gravitational wave frequency ω_0 , proper separation d , central density of each star ρ_c . The parameters in the polytropic EoS are $\Gamma = 2$ and $K = 123.6489$.

M	M_b	M_\star	J/M^2	ω_0 [Hz]	d [km]	ρ_c
2.998	1.625	1.456	0.445	589	54.0	9.569

Table 7.2.: Grid configurations used in BNS simulations. Columns: name of the grid configuration, number of grid levels, number of levels containing moving boxes, resolution of finest level (dimensionless and km), number of points in finest box, resolution of coarsest level (dimensionless and km), number of points in coarsest box.

name	RL	MRL	h_5	h_5 [km]	N_5	h_0	h_0 [km]	N_0	boundary [km]
L	6	4	0.500	0.74	40	16.0	23.6	80	945
M	6	4	0.400	0.59	50	12.8	18.9	100	945
H0	6	4	0.313	0.46	64	10.0	14.8	128	945
H1	6	4	0.250	0.37	80	8.0	11.8	120	709
H2	6	4	0.200	0.29	100	6.4	9.4	210	982
H3	6	4	0.156	0.23	128	5.0	7.4	260	960

The grid configuration used for the evolution simulations are presented in Tab. [7.2](#). Simulations with configurations L and M can be run on a small machines. They need between 8 and 16 processors with 1GB of memory per core. While they can be carried out without any problem, thus proving the flexibility of the code, the results are too inaccurate to be considered in a sensible analysis. Here we need more resolution. Therefore we only use the configurations H0 to H3 to measure convergence. For each grid configuration the finest refinement level covers each star entirely. The H0 runs need 64 points in one direction, H3 runs use 128. In compare to BBH simulations, e.g. [52](#), [95](#), [84](#), the grid structure is different from BNS simulations. For BBH simulations roughly half the number of points per direction is used together with more grid levels (typically 9-11 levels). Higher resolutions are reached in the finest grid level in order to resolve the punctures, while comparable (or less) resolutions are used on level 5, where in our grid setup the neutron star is fully resolved. Therefore the horizon of the final BH in BBH simulations is resolved typically on level 6 or 7 with a resolution about two to four times better than in BNS simulations. One important consequence is that the final black hole is poorly resolved. All simulations show that the resolution is high enough to obtain a stable simulation but the precision of the apparent horizon finder (see [82](#), [8](#), [52](#) for details), and the extracted information, e.g. horizon mass and spin, is affected.

The performance of the code for each grid configuration is reported in Tab. [7.3](#). The BNS runs described here have an average speed of ~ 3 M/hr (H3) on 128 processors in the LRZ cluster (Munich) and ~ 9 M/hr (H0) on 32 processors. In physical units 10 M

Table 7.3.: Performances of BNS runs. Columns: name of the grid configuration, number of processor, CPU memory, total runtime, average speed. Runs last to $t = 5000$ (1666 M) on LRZ Munich. The numbers include LORENE initial data interpolation and checkpointing.

Name	nproc	mem [GB]	time [CPU hr]	speed [M/hr]
H0	32	90	192	8.7
H1	32	96	268	6.2
H2	128	120	254	6.5
H3	128	165	480	3.5

of the configuration selected corresponds to ~ 0.05 ms of simulation. All simulations do not have the optimal grid configuration. They were build in a generic way to preserve the box configuration while changing resolution. With some fine tuning we found good scaling up to 512 processors by using larger grid setups and higher resolutions. Production runs with resolutions of $h_5 \sim 0.12 - 0.10$ on 256-512 processors are thus definitely feasible in reasonable times with our code. Since computer time is restricted only a few long time simulations could be performed.

My grid settings are similar to those of other codes [27, 77]. The highest resolution employed here is 30 % lower than the maximum resolution used to date on BNS simulations employing mesh-refined-Cartesian-grid-based codes [18, 77] and are comparable to [97].

If not explicitly stated the data discussed refer to simulations employing RK3 time stepping, CFL factor of 0.25 and CENO reconstruction.

7.2. Dynamics for cold EoS

In this part I discuss the evolution of poly EoS, i.e. isentropic evolutions. The ideal gas $\Gamma = 2$ (hot EoS) is discussed in the next section. I tested my implementation of the code for this EoS since the results are easier to compare with other groups. Here I performed simulations for all configurations reported in Tab 7.3 which gives a wide range of resolutions. I found that all grid configurations give stable simulations. All simulations showed a convergent behavior. However, I found the two lower resolutions L and M had too low resolution. Both show a merger which is too early. They have between one and two orbits. On the other hand the higher resolution had more than

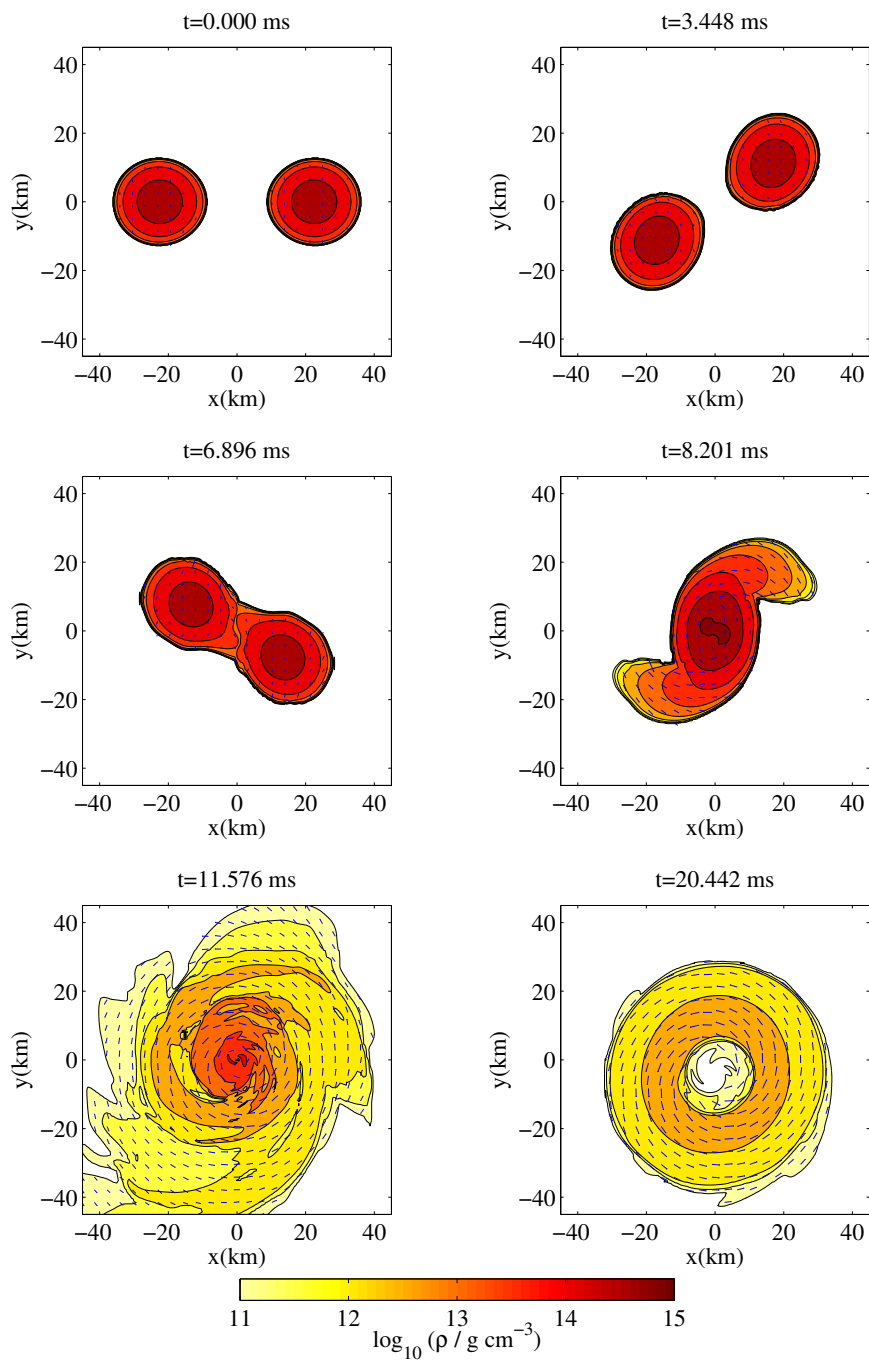


Figure 7.1.: Dynamics of the cold evolution. The picture shows contour plots in the $x - y$ plane of the rest-mass density ρ and the velocity v^i at different times. Data refer to run H3.

three orbits. Therefore only the runs H0 to H3 seem to qualitatively capture the correct physics according to [21, 77]. The main quantitative differences are found in the post-merger phase, in particular in the collapse time of the final neutron star. This is not very surprising since soon after the two stars come in contact convergence of this kind of simulation drops to first order, e.g. [22]. The post-merger phase is thus very dependent on the resolution and grid settings employed as well as on the specific HRSC scheme employed. Note that my highest resolution of $h_5 = 0.23$ km of H3 is about 30% below the resolution reported in [22]. Therefore I do not expect the same results.

Fig. 7.1 shows contour plots in the $x - y$ (orbital) plane of the rest-mass density and the velocity field at different times of the cold evolution. Data refer to run H3. The binary performs about three orbits before the merger. The merger time is not an obvious measurement since the surface of the star is determined by a certain threshold on the density and the first touch can happen long before the final neutron star is built. The GW amplitude seems to be a better indication. I define the merger time t_m as the peak of the (2,2) mode of the GW amplitude $|h_{22}|$, where $h \equiv h_+ - i h_\times$ (see section 7.7). From the H3 run we have $t_m = 1765$ (8.69 ms) while the contact time is about 1290 (6.3 ms). After the merger we observe a bar-shaped differentially rotating star with rest-mass $\sim 2M_b$: the hyper massive neutron star (HMNS). A HMNS is a differentially rotating NS. The mass is larger than a the maximal allowed mass of a stable uniformly rotating star. Note in Fig. 7.1 the initial rotational symmetry of the HMNS. It is obtained without imposing π -symmetry in the grid till short before the collapse to a black hole. Afterwards the symmetry is broken, especially inside the disk. The large non-axisymmetric deformation of the HMNS causes a strong GW emission [161, 20] which carries away matter angular momentum. As a result the HMNS becomes more compact and finally collapses at about $t_{\text{AH}} \sim 2118$ (10.43 ms) when an apparent horizon is first formed. A fraction of the matter ($\sim 1.2\%$) remains outside the horizon and forms an accretion disk. For late times the disk restores approximately the rotational symmetry. The mass and spin of the BH estimated from the apparent horizon are rather inaccurate due to a lack of resolution mentioned before. They first rapidly grow in time reaching local maximum, then the BH mass is observed to increase (see Fig. 7.11) while the angular momentum decreases. We estimate at the end of the evolution $M_{\text{BH}} \sim 2.77$ and $a_{\text{BH}} \equiv J_{\text{BH}}/M_{\text{BH}}^2 \sim 0.72$. They have discrepancies of about 7% and 25% from the expected value once the gravitational radiation emission has been

taken into account. Since the apparent horizon is defined locally, the gauge choice plays an important role by determining the coordinate size of the black hole. This has an additional effect on the accuracy of the apparent horizon finder. In comparison to the collapse discussed in Sec. 6 we do not have refinement inside the star. Therefore the finder has only a few points if the coordinate sphere is small.

The mesh refinement implementation is such that as soon as the two moving boxes come in contact (which happens before the contact of the two stars) a larger box with the same resolution is constructed. Before the two stars come to touch however it can happen that the boxes split back to the initial ones, evolve individually and merge again. The reason is that the evolution of a very large box is computationally not affordable in terms of memory and time. This behavior is well tested in BBH simulations [52]. However, it could lead to a lack of accuracy at the center of the grid but in practice it has a negligible impact since it happens when the main part of the matter is still distributed away from the center.

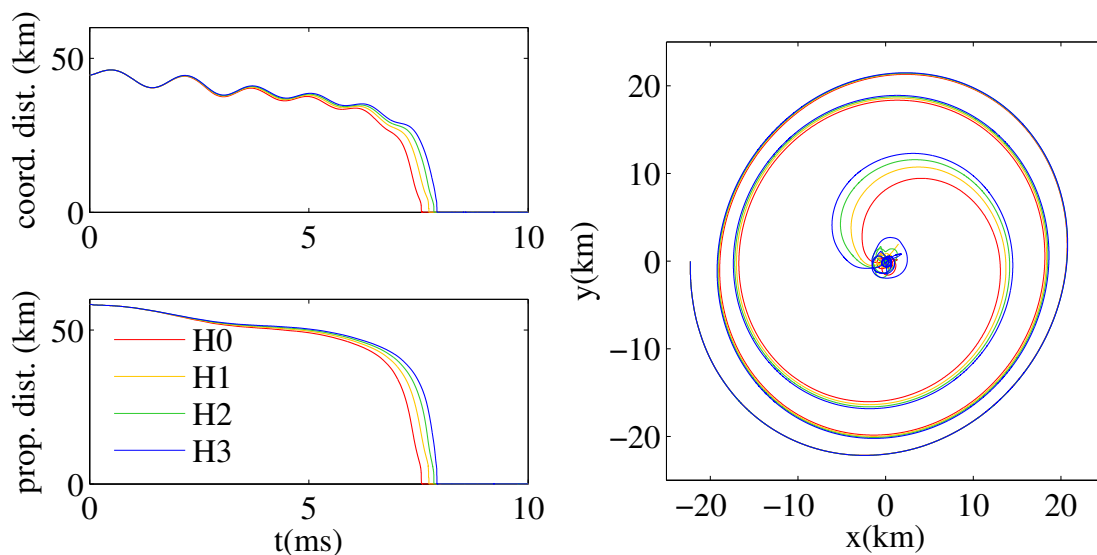


Figure 7.2.: Orbital motion of the cold configuration. The figure shows the evolution of the coordinate (top-left) and proper (bottom-left) separation of the binary and the star-tracks (right) of the two stars for different grid settings.

Fig. 7.2 reports the coordinate movement of the star binaries with different resolutions. The right panel shows the star tracks which are defined by the minimum of the lapse for resolutions H0,H1,H2 and H3. Tracking the maximum of the density seems to

be a more meaningful quantity to describe the center of a star. However, this quantity is badly behaved during the transition from a star to a black hole, and I found that the maximum of the density and the minimum of the lapse are always very close before the transition. Due to the gauge condition used the lapse function is everywhere smooth and ensures a suitable tracking. The left panel instead shows for the same resolutions the coordinate (top) and proper (bottom) spatial separation. As is evident from the figure, the orbital motion has some eccentricity due to the initial data (visible in the proper separation plot) and a coordinate eccentricity (visible in the star-tracks and as oscillations in the coordinate separation) due to the evolution itself. The eccentricity of the initial data is caused by the conformally-flat approximation; the effect becomes bigger at smaller separation. The contribution to the coordinate eccentricity is mainly due to the shift condition. As shown in Fig. 7.2 the use of a lower resolution results in an earlier merger. However all four resolutions enter “convergent regime” in the sense that we are able to estimate convergence.

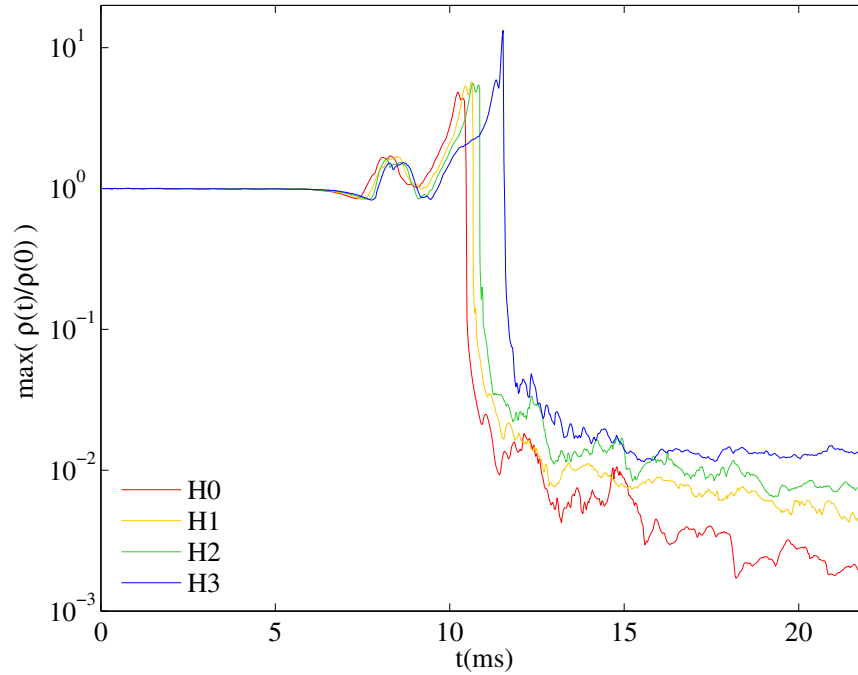


Figure 7.3.: Evolution of the central rest-mass density in BNS simulations for different resolutions.

In Fig. 7.3 the evolution of the maximum density for different resolutions is reported.

After the merger the HMNS is oscillating about two quasi-radial oscillations and finally collapses to a black hole because the HMNS becomes too compact. Here the highest resolution shows the tendency to oscillate longer. After the collapse the matter of the disk accretes onto the BH.

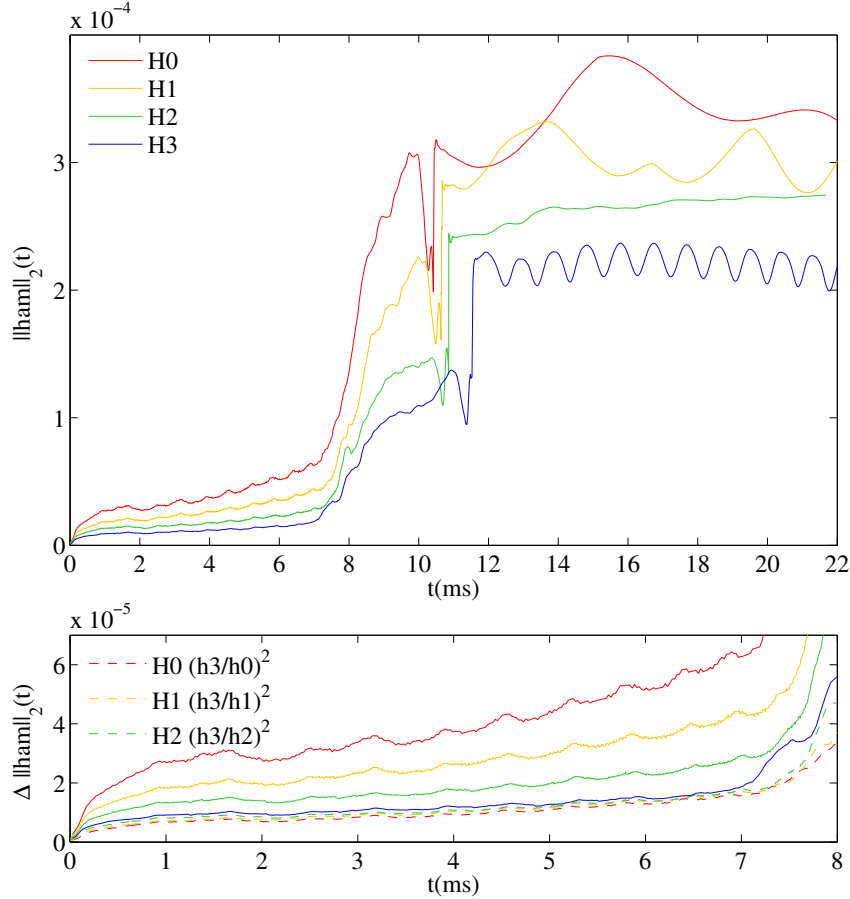


Figure 7.4.: Hamiltonian violation for cold evolution. The figure shows the evolution of the L2 norm of the Hamiltonian constraint for different resolutions. The lower panel shows the difference during the inspiral where convergence is expected. The dotted lines are multiplied by a factor for 2nd order convergence.

Concerning the constraints, the biggest violation is found in the Hamiltonian. The momentum constraint is generically one order of magnitude smaller and becomes comparable to the Hamiltonian constraint only after the formation of the “puncture”. Fig. 7.4 reports the L2 norm of the Hamilton constraint. As one can see the norm

improves with resolution. The lower panel shows the convergence. The curves are multiplied by the convergence factor corresponding to the expected 2nd order convergence. For the first 7 ms the curves agree very well. Most of the violation is observed in the region covered by matter, similar to what was discussed for the test involving a single star spacetime. After the two stars come in contact the violation rapidly increases and the convergence rate drops down. At the time when an apparent horizon first forms the constraint violation shows a peak, afterwards it stays approximately constant. This is related to the final BH where the matter influence is small in comparison to the puncture.

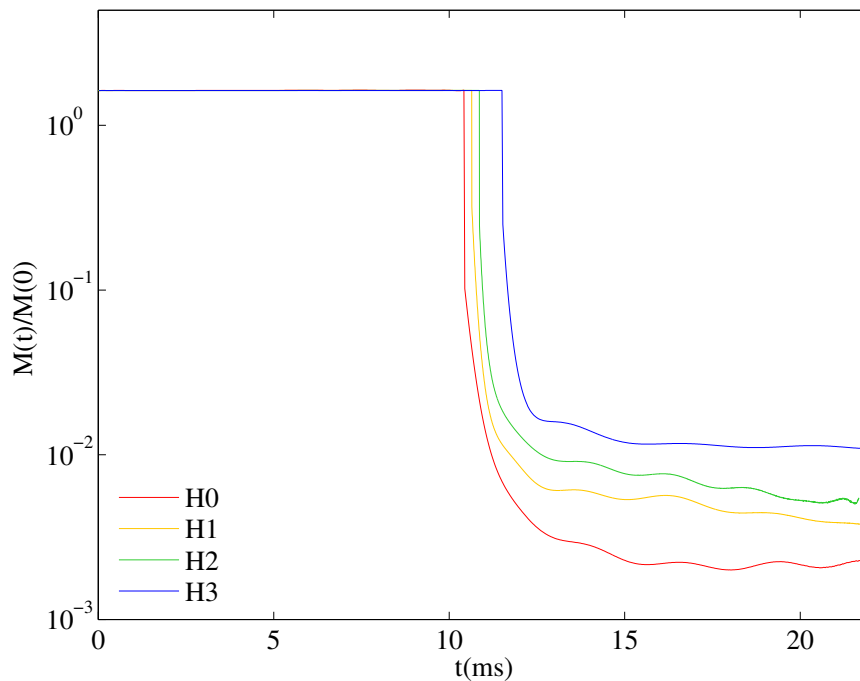


Figure 7.5.: Conservation of rest-mass in BNS simulations. The figure shows the evolution of the rest-mass normalized to the initial value for cold evolutions with different resolutions.

The conservation of the rest-mass is excellent until the BH forms with a largest deviation of $\Delta M_0/M_0 \sim 2\%$ in the H0 runs and lower than $\Delta M_0/M_0 \sim 0.5\%$ in the H3 runs. This behavior is illustrated in Fig. 7.5 which displays the evolution of $\Delta M_0/M_0$. One can also see the matter accretion after the collapse. From the figure it is clear that the rest-mass of the disk increases with resolution. In our case we have an

upper limit of about $M_d \lesssim 2 \times 10^{-2} M_0$ for H3 since we compute it by

$$M_0 = \int q^0 d^3x = \int \sqrt{\gamma} D d^3x \quad (7.1)$$

on the whole grid, including the interior of the BH. An final estimate for the disk using the data here would be very vague since the resolution is not high enough.

7.3. Effect of different reconstruction methods

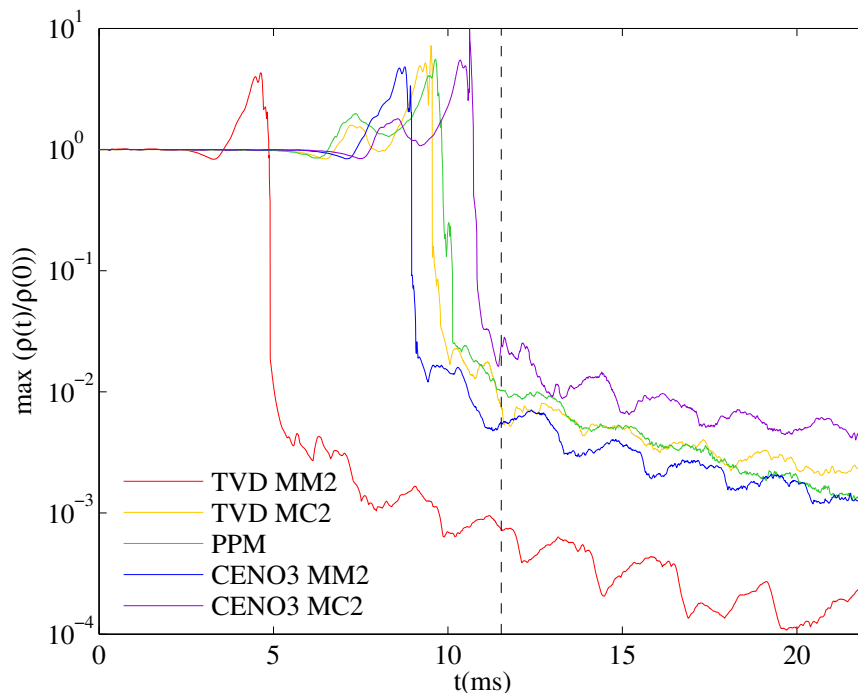


Figure 7.6.: Dependence of the dynamics on the use of different reconstruction schemes. The figure shows the maximum of the rest-mass density obtained from cold evolutions with different reconstruction methods. Reference vertical line corresponding to $\max \rho$ of run H3.

As pointed out in Sec. 5.2 the different reconstruction methods have a different effect on the truncation error. Therefore the result can be changed significantly. Ref. [76] already pointed out that the use of very dissipative limiters such as MM2 can lead to very different waveforms with respect to (formally) more accurate methods, while maintaining the same nominal order of convergence.

We tested our binary system at resolution H1 with the following reconstructions: MM2, MC2, PPM, CENO and CENO based on the MM2 sub-stencil (instead of the standard MC2 [186]). The resolution we used was far away from optimal therefore we achieved dramatic differences in the evolutions. In Fig. 7.6 we show the evolution of the maximum rest-mass density for the different methods. The vertical line shows the time of the maximum in the highest resolution run H3. As one can see the merger time are very different. As partially expected, the most diffusive schemes lead to an earlier merger and collapse. Formally higher order reconstruction are closer to the result obtained by using the highest resolution H3. The simulations with MM2 reconstruction show the shortest inspiral and no HMNS is formed. The simulations with MC2 has an early prompt collapse. On the other hand PPM and CENO show a later collapse and a HMNS is formed. Here CENO seems to be the best choice due to the latest merger time. Introducing a more dissipative component in the CENO limiter, i.e. the MM2 linear sub-stencil, the global results are significantly affected: an earlier prompt collapse is observed. The specific reason is obviously the fact that the linear sub-stencil MM2 is often selected by the limiter. Note that we did not obtain a guarantee for long-term-stability of an equilibrium spherical star. This was also mentioned in 1D [39].

Clearly the big differences shown here become progressively smaller when higher resolutions are considered. However, due to the slow (2^{nd}) order convergence of HRSC, we expect they play a major role also at the higher resolutions employed for standard production runs. Recently in [MTH4] we performed higher resolution runs for larger separation and therefore longer simulations. The CENO scheme is working well and shows the expected convergence behavior, which means we are inside the convergent regime. In comparison to the presented runs, these runs only approach the accuracy which is necessary for astrophysical relevant simulations (see the conclusion in [MTH4]).

7.4. Comparison with hot EoS

In hydrodynamic simulations physics inside the star is describe by the EoS. Till now we considered only a cold (polytropic) EoS. As discussed earlier this is a good approximation for the (late) inspiral before the stars touch. Subsequently thermal effects and micro-physics do play a important role during the merger and the HMNS phase.

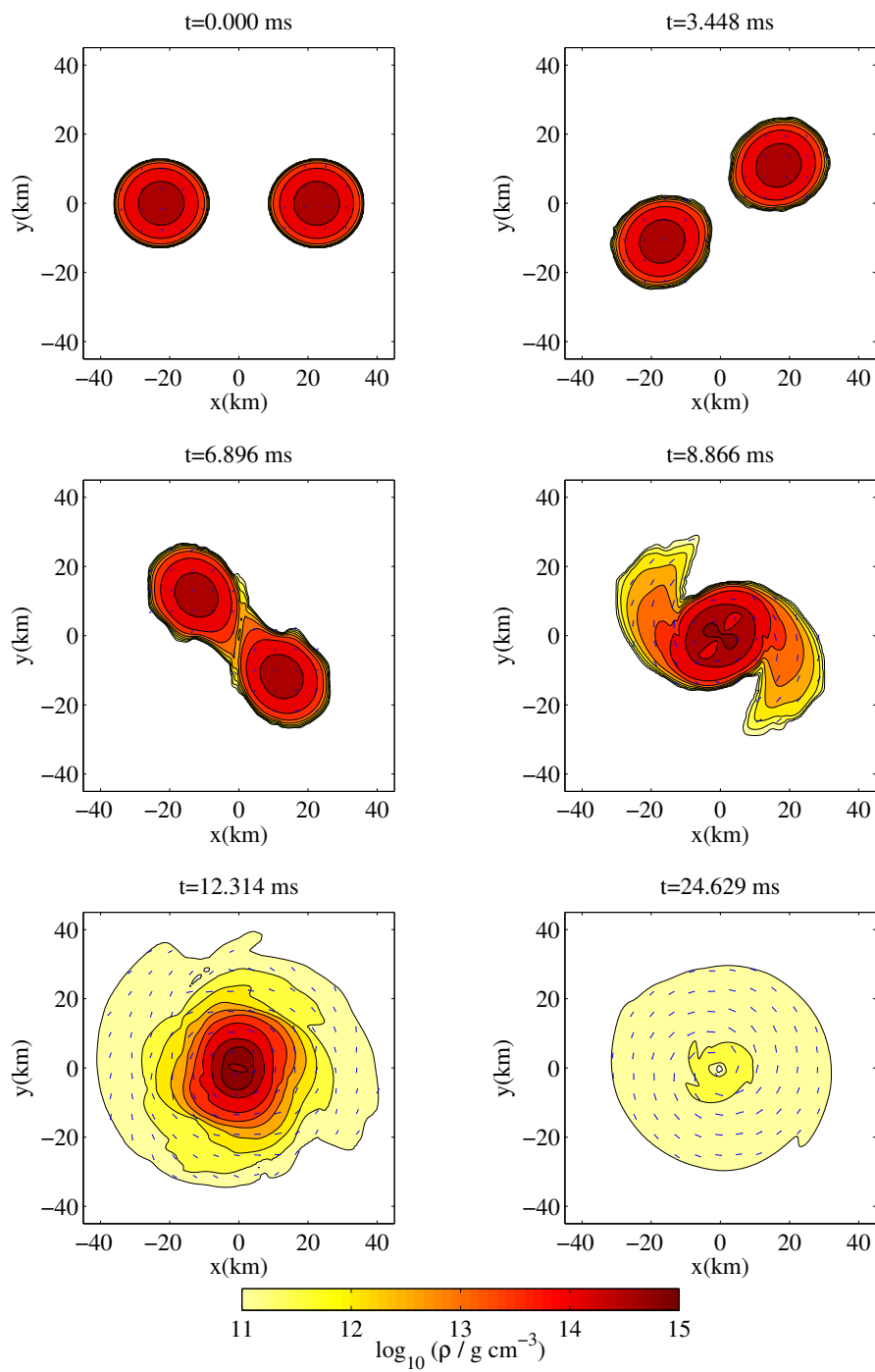


Figure 7.7.: Dynamics of the hot evolution. The picture is similar to Fig. 7.1. Data refer to run H1.

Therefore the cold EoS can not be used to describe the system after the merger and one has consider thermal effects by using a more realistic EoS which is denoted as a hot EoS. In my case I use the simplest analytic model namely an ideal gas (see chapter 2.3.2). I performed the same evolution as in the previous section. Fig. 7.7 shows contour plots in the $x - y$ (orbital) plane of the rest-mass density and the velocity field at different times. Data refer to the H1 resolution. The inspiral motion of the two binaries present small differences due to spurious numerical effects. Small errors, triggered by the artificial atmosphere treatment, propagate as simulation time advances and artificially heat the stars especially at their surface. The effects of these errors on the GWs are quantified in the following section. When the two stars touch physical effects dominate instead and the evolutions significantly differ.

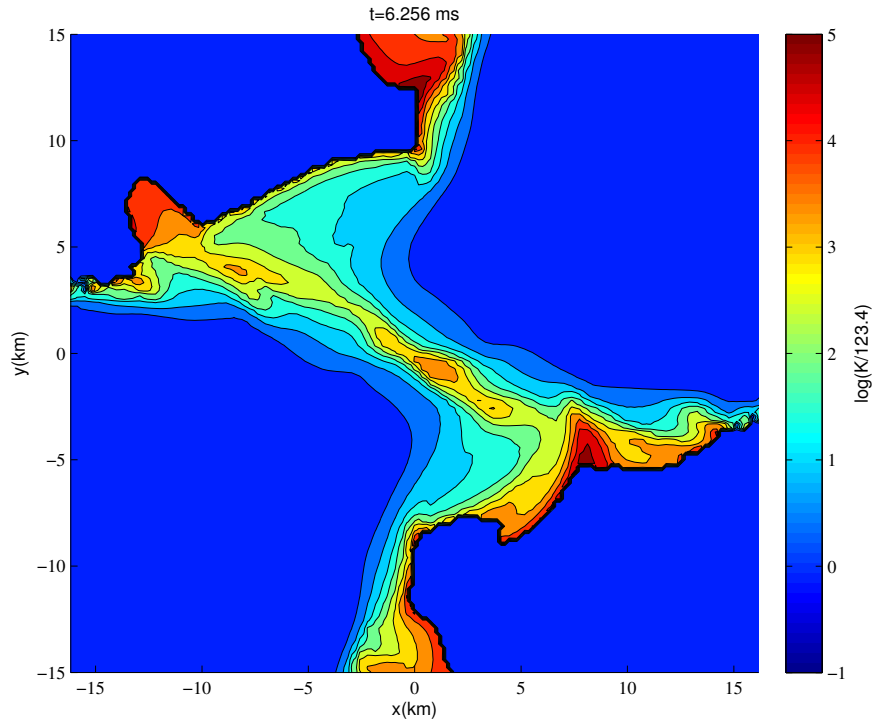


Figure 7.8.: Shock formation in hot evolution. The figure shows the quantity $K = p/\rho^\Gamma$ normalized by its initial value on the orbital plane at time $t = 1275$ (6.256 ms) in a \log_{10} scale. Data refer to run H1.

Fig. 7.8 shows the quantity $K = p/\rho^\Gamma$ (normalized by its initial value) as a contour plot in the $x - y$ plane. Here K is a simple measure for the entropy. The variation of this quantity indicates the presence of shocks. For the cold EoS this quantity is a constant

by construction. To determine whether there are shocks one has to use some “shock detector” [188] which I did not use in the following¹. During the evolution the included thermal effects result in shock formations when the two stars are touching each other. The quantity K is increased by around 5 order of magnitudes. The thermal energy of the fluid rapidly increases reaching peaks of $\epsilon^{\text{hot}} \sim 0.025 - 0.03$. This corresponds to a temperature of $T \sim 2 \times 10^{11}$ K. The average temperature is of the order $T \sim 6 \times 10^{10}$ K. The peak temperature goes up to $T \sim 2 \times 10^{12}$ K. These high values are appearing at the surface and could be an artifact of the atmosphere treatment. However, in the bulk the values are only 1 to 2 magnitudes lower, which results in temperatures around $T \sim \times 10^{10}$ K.

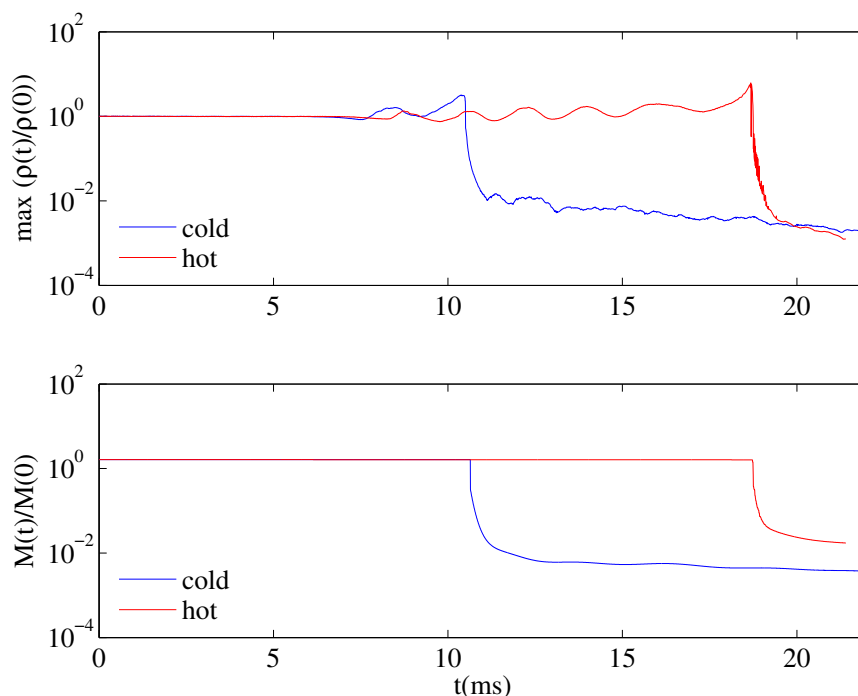


Figure 7.9.: Comparison of hot and cold evolution. The top panel shows the maximum of the normalized rest-mass density, the lower panel the rest-mass normalized to the initial value. Both runs refer to resolution H1.

Due to the additional pressure support provided by thermal effects the HMNS in the evolution collapses later. As shown in Fig. [7.9] the merger takes place around

¹A comparison showed similar results in the central region of Fig. [7.8]. However, most shocks are detected at the surface of the star which can be explained by the usage of artificial atmosphere.

~ 9 ms after the merger in the cold case. This means the HNMS is more stable and during this time interval several quasi-radial oscillations at a frequency $\nu_F \sim 473$ Hz are present. There is a strong GW emission which is discussed in the next section. The central density shows again a drift to larger values indicating that the star is becoming progressively more compact. Again the rest-mass conservation is quite as good as in the cold case. An estimate of the disk-mass is about 1% of the initial mass.

Comparing both evolutions for cold and hot EoS with the literature one obtains slightly different results. In [21] the evolution of cold EoS leads to a prompt collapse without the formation of a HMNS, while the evolution of hot EoS leads to a collapse at about $t \sim 14$ ms (simulations employ the PPM implementation described in [91] and the Marquina numerical flux). In [77], where a different grid setting is employed (but the same code with the HLL numerical flux), the evolution of the hot EoS leads to a collapse at about $t \sim 16 - 17$ ms. In both works [21, 77] π -symmetry was used. In our case we implied plane symmetry, only data with $z > 0$ is evolved. Therefore we see the break of the symmetry in the disk after the merger. It is expected that the simulation leads to a more persistent HMNS due to non-linear mode couplings (in particular $m = 1$ modes) [20]. It is therefore unlikely that this symmetry is the reason for the above mentioned differences. Applying π -symmetry in my simulations gave in principle similar results for the evolution of the maximal density.

7.5. Evolution with different damping parameters

Looking at the gauge equations (2.13) and (2.14) the damping parameter η in the Gamma-driver shift condition was well investigated for unequal mass BBH simulations [127, 111, 110, 112, 156, 128, 10]. In case of equal mass BBHs it is typically set to $\eta = 1/M$ or $\eta = 2/M$ to obtain properly resolved black holes on the grid [52]. Here M is the sum of both ADM masses. In case of neutron star simulations this is rarely investigated. For BNSs it has been suggested [27] that results are not significantly affected by this choice. Different values are adopted in the literature, e.g. $\eta = 3/M_b$ [184, 27], $\eta = 1$ [21], without a detailed analysis. Here we investigate the influence of the η parameter on the dynamics of the inspiral in case of binary neutron star systems.

We consider the same setup as before with grid configuration H1 and values $\eta = 0, 0.1, 0.3, 0.6, 0.9, 1.8$, i.e. $\eta \simeq 0/M, 0.3/M, 0.9/M, 1.8/M, 2.7/M, 5.4/M$ in dimen-

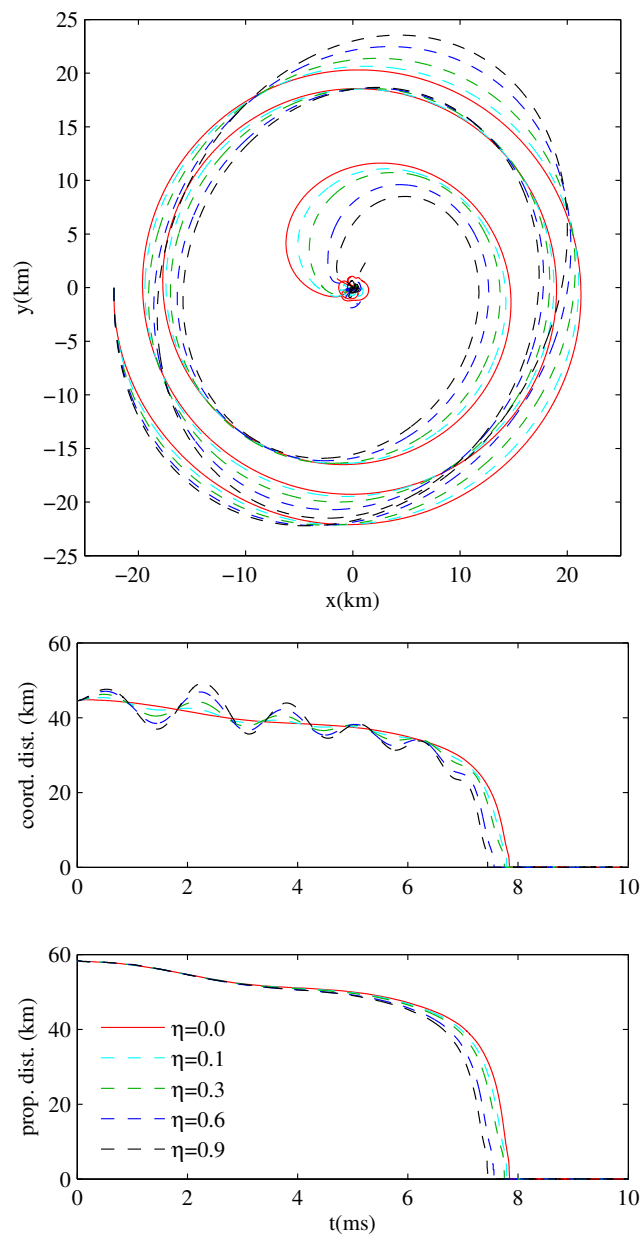


Figure 7.10.: Effect on orbital dynamics of different choices of the parameter η in the Gamma-driver shift condition. The top panel shows the star-track of one star. The central panel shows the evolution of the coordinate separation while the bottom panel shows the evolution of the proper separation of the binary. Each line refers to a different cold evolution with a different η . Data refer to H1 runs.

sionless units. Fig. 7.10 shows the star-track (top panel), the evolution of coordinate separation (central panel), and of the proper separation (bottom panel) from simulations with different values of η . One can see a clear correlation between an oscillation in the coordinate distance and the η parameter. This coordinate eccentricity is largely increased for higher values of η . This non-circular effect is an artifact from the conformally flat initial data. Additionally the merger time is systematic shifted to earlier times which comes from the effective coordinate resolution. When considering the gravitational wave emission the coordinate eccentricity does influence the extracted waves and it manifests itself in a phase difference accumulating during the inspiral. Taking as a reference the $\eta = 0$ case, the difference in the phase ϕ of $r \Psi_{22}^4$ computed with $\eta = 0$ is of $\Delta\phi = 0.43, 0.90, 2.25, 3.20$ rad respectively for $\eta = 0.1, 0.3, 0.6, 0.9$ at the merger time (see next section).

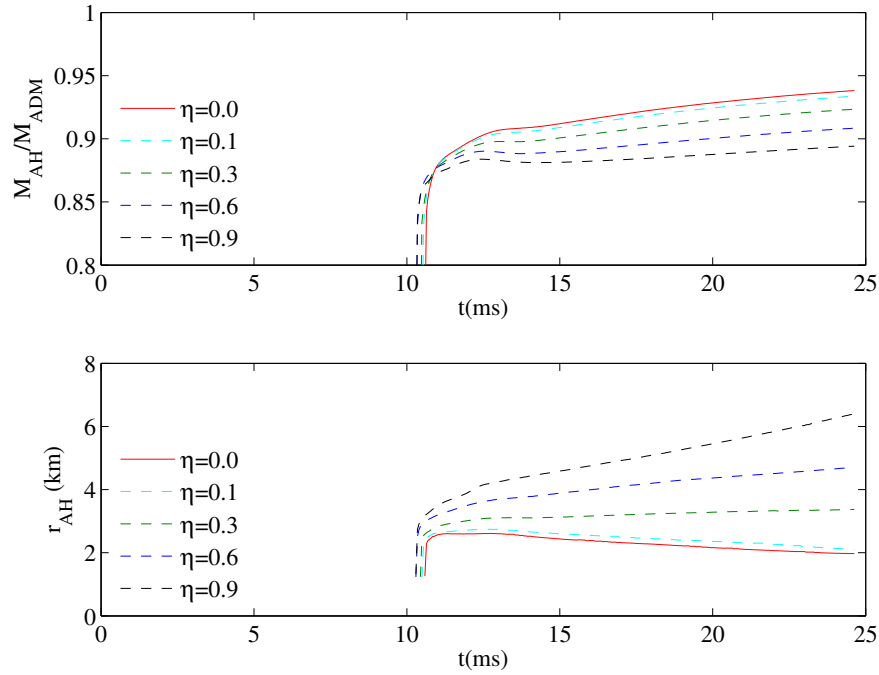


Figure 7.11.: Effect on the final BH mass and coordinate radius of the parameter η in the Gamma-driver shift condition. The top panel shows the irreducible mass of the final BH normalized by the ADM mass of the system as computed from the apparent horizon finder. The bottom panel shows the coordinate radius of the apparent horizon. Each line refers to a different cold evolution with a different η . Data refer to H1 runs.

The Gamma-driver shift condition tries to prevent slice stretching. Now the η parameter effects the amount of the stretching and therefore regulates the effective resolution. Therefore it will have an effect on the apparent horizon (AH) and the ADM quantities. Both are computed at a coordinate sphere. Fig. 7.11 shows the irreducible mass, M_{AH} (normalized to the ADM mass of the system), and the coordinate radius, r_{AH} , of the apparent horizon. As expected, both the ADM mass and the radius of the apparent horizon ($r_{\text{AH}} = \sqrt{A_{\text{AH}}/16\pi}$) depend on η . The coordinate size of the final BH is larger for higher values of η . Having this in mind one has to optimize η since we want to keep the ability of “correctly” resolving the final BH on the finest grid level while reducing the coordinate eccentricity. Increasing η would give us a better resolved BH. On the other side I did not plot the result for $\eta = 1.8$ due to the fact that I obtain an unacceptable eccentricity (see Fig. 7.10) and the size of the final BH is too large for the finest refinement box. This results in an inaccuracy of the apparent horizon finder which cannot use the highest possible resolution. In a similar way the usage of large η also affects the coordinate radius of the GW extraction spheres; smaller proper radii corresponds to higher η . Since we extrapolate the values measured at certain coordinate spheres to infinity this has a small effect compare to other errors (see next section).

However, looking at Fig. 7.11 and 7.10 I found a value around $\eta = 0.3/M$ as the best choice for my simulations. Note that different values of η only changes the coordinates, not the physical solution. Therefore coordinate independent parameters are in principle not effected.

7.6. Gravitational waves

Gravitational radiation plays the fundamental role driving the dynamics of the binary system. GWs encode information from each phase of the evolution from the inspiral to the collapse and the BH-disk formation. Here we focus on the cold EoS.

The main part of the GW emission is done by the $(\ell, m) = (2, 2)$ mode of the multipolar ($s = -2$ spin-weighted spherical harmonics) decomposition. The $(2, 2)$ mode includes about 97 % of the entire radiated energy. Thus, we focus the analysis on this particular mode. Fig. 7.12 presents the complex waveform $r\Psi_{22}^4$ computed from the Newton-Penrose scalar Ψ^4 for the highest resolution H3. The computation of the Ψ^4 is

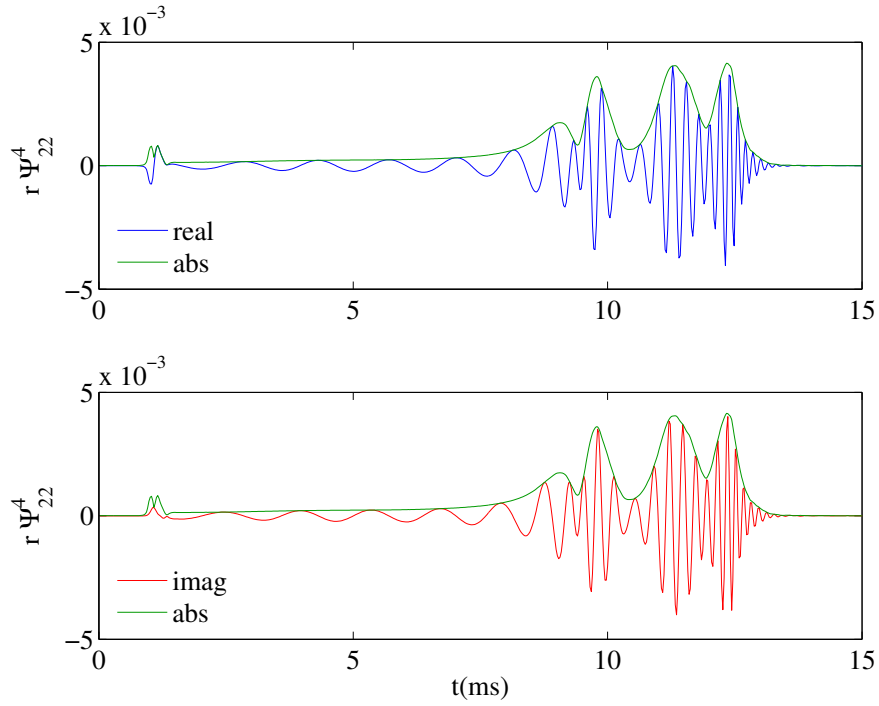


Figure 7.12.: Ψ^4 waveforms from cold evolution. The figure shows the real part (top panel) and the imaginary part (bottom panel) of the $r \Psi_{22}^4$ waveform extracted at $r = 294$ km from the H3 run. The amplitude is also shown in both panels.

given in [B.2](#). We multiply by the radius to get rid of $1/r$ behavior of the amplitude. The complex waveform is usually decomposed in amplitude and phase, $r \Psi_{22}^4 = A \exp(-i\phi)$. [Fig. 7.12](#) shows the real (blue solid line) and the imaginary part (red dashed line) as well as the amplitude (green solid line). The extraction is done at a sphere with the radius $r = 200$ (294 km). We also extracted at different radii, namely 50, 100 and 150. All values show the expected fall-off behavior. From the plot one clearly identifies the inspiral phase followed by the emission related to the HMNS oscillations and then the collapse. At early times (~ 1 ms) the well known initial “junk” radiation can be seen.

The Ψ^4 waveform is the second derivative of the metric waveform $h \equiv h_+ - i h_\times$. h represents the actual GW degrees of freedom. Since we compute Ψ^4 during the simulation we have to integrate twice by

$$h_{\ell m} = \int_{-\infty}^t \int_{-\infty}^{t'} \Psi_{\ell m}^4 dt'' dt', \quad (7.2)$$

to obtain h multi-poles from those of Ψ^4 . This integration requires some attention. In [138, 42, 28, 64, 17] h is computed via a direct (time domain) integration on the simulated time domain. In all cases the integration is affected by a polynomial drift, which is corrected by fitting, called corrected time domain integration (CTI). Analytically one expects a linear drift due to the two integration constants in Eq. (7.2). Anyhow the observed drift has a higher polynomial order. It originates from the integration of high-frequency noise in the data and has a stochastic nature [143]; they propose a better procedure by fixed-frequency integration (FFI). It is based on a spectral integration in the Fourier basis. To prevent spectral leakage a high-pass frequency filter is employed by simply cutting off frequencies below a certain threshold.

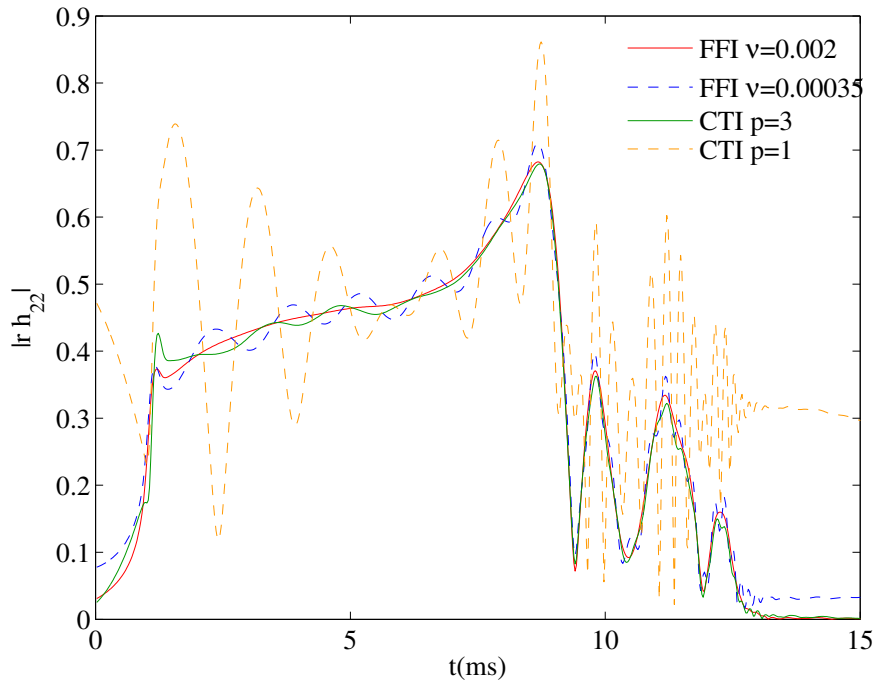


Figure 7.13.: Gravitational wave amplitude $|r h_{22}|$ from cold evolution. The figure shows the amplitude computed with the FFI $\nu_0 = 0.002$ (red solid line) and $\nu_0 = 0.00035$ (blue dashed line) and with the CTI where a cubic (green solid line) and linear polynomial (yellow dashed line) correction is used.

We tried both integration procedures (CTI and FFI) to compute h_{22} . The polynomial correction employed in the CTI is a 3rd order polynomial. This choice is preferred against a linear or quadratic correction since it minimizes experimentally the drift in the raw integrated waveforms and the oscillations in the modulus. For the FFI method we use

a cut off frequency of $\nu_0 = 0.002$ (406 Hz), which is around the GW frequency of the initial data. To avoid that this frequency is filtered we use a value slightly below this GW frequency. The phase difference between the two metric waveforms amounts to $\Delta\phi \lesssim 0.06$ from early times until the collapse. Since this value is so small compared as to the length of the signal it can be neglected (see error estimates below and Tab. 7.4). On the other hand the error in the amplitude is much larger. The maximal deviation is about $\Delta A/A < 5\%$ during the inspiral and grows to about 15% before the collapse. Fig. 7.13 presents the amplitude $r h_{22}$ of both integration methods: solid red line for FFI and solid green line for CTI. One can see an important effect between both. The amplitude computed with the CTI shows oscillations during the inspiral. They converge away for higher resolution but it is not possible to remove them completely. They are also reduced for larger extraction radii. Using a lower order integration method results in a completely different shape (see the orange dashed line). On the other hand the amplitude obtained by the FFI waveform integrated with $\nu_0 = 0.002$ is free from these oscillations for all the resolutions considered. Here it is important to find the correct cut off frequency. Going to $\nu_0 = 0.00035$ (71 Hz) oscillations appear again (blue dashed-dotted line). Note that a frequency of 71 Hz roughly corresponds to the finite length of the signal. As observed in [64, 143] the oscillations are an unphysical effect not related to eccentricity. However we find a correlation between the oscillations in the amplitude of $r h_{22}$ and those seen in the coordinate separation (Fig. 7.10) in the runs with different values of η . This could be an effect of the gauge on the location of the extraction spheres where h is calculated. Here a proper choice of ν_0 in the FFI can mostly eliminate them. The polynomial fitting in CTI is not as robust and does not perform as well for our data.

The analysis of h_{22} with both the CTI and the FFI procedure give comparable results. However, we used the FFI for all the analysis. Looking at Fig. 7.14 it shows the metric waveform $r h_{22}$ computed from $r \Psi_{22}^4$ as a function of the retarded time $t_{\text{ret}} \equiv t - r_*$. Here $r_* \simeq 222$ is the tortoise radius [2] corresponding to $r = 294$ km. The real and imaginary part are shown as well as the amplitude for the highest resolution H3. The merger time t_m is formally defined by the peak of the amplitude [41, 19]. Considering

² The tortoise radius is computed as $r_* = r_{\text{Schw}} + 2M \log(r_{\text{Schw}}/(2M) - 1)$, where r_{Schw} is the Schwarzschild radius corresponding to the isotropic radius r . The retarded time based on this coordinate, $t_{\text{ret}} = t - r_*$, is a useful but approximate quantity which becomes rigorous only at large radii when the spacetime becomes Schwarzschild. The correspondence dynamics-waveform in the simulation is thus biased by this approximation.

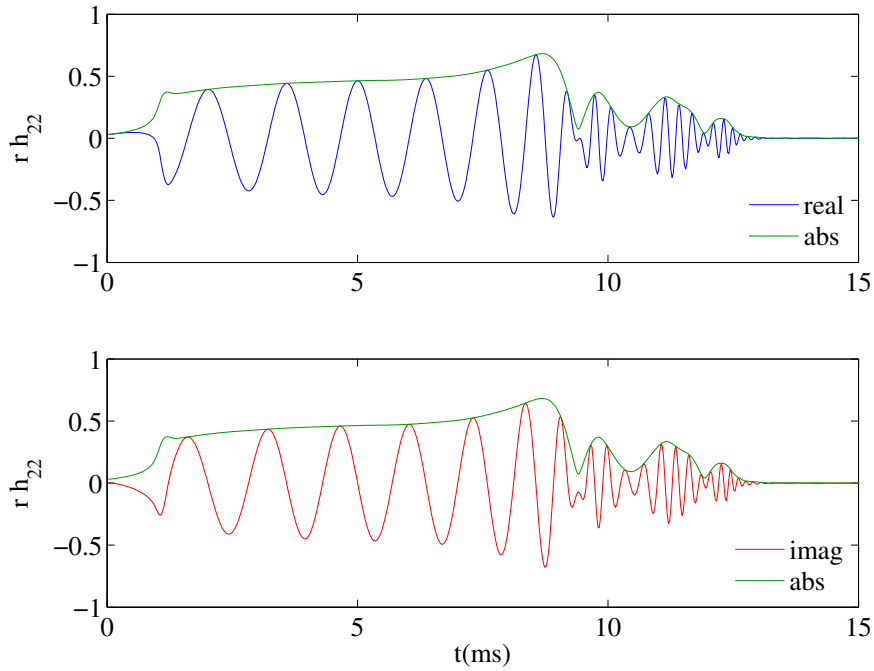


Figure 7.14.: Metric waveforms from cold evolution. The figure shows the real part (top panel) and the imaginary part (bottom panel) of the $r h_{22}$ waveform extracted at $r = 294$ km from H3 run. The amplitude is also shown in both panels. The waveforms are plotted versus the retarded time $t_{\text{ret}} \equiv t - r_*$ where r_* is the tortoise radius corresponding to r . The metric waveform is computed with the FFI and cutoff frequency $\nu_0 = 0.002$.

different resolutions we found $t_m = 1670, 1710, 1740$ and 1765 (8.23, 8.42, 8.57 and 8.69 ms), respectively, for runs H0-3. The corresponding retarded times are $t_{m,\text{ret}} = 1446, 1486, 1516, 1541$ (7.12, 7.32, 7.47, 7.59 ms). The metric waveform is composed at early times of six GW cycles emitted during the three orbit inspiral. After the merger the emission is dominated by the bar-deformed HMNS, and the signal has a typical frequency around 3 kHz which increases as the HMNS becomes more compact [40, 115]. Finally, after $t_{\text{ret}} > 2132$ (10.5 ms) the GW signal is composed of the quasi-normal-mode ringing of the BH. The fundamental frequency computed from the waves has a value of about $\nu_{\text{QNM}} \sim 6.5$ kHz. It is compatible with the estimate of the BH mass and spin from the apparent horizon [67, 21], i.e. $\nu_{\text{QNM}} \sim 3.23(10/M_{\text{BH}})[1 - 0.63(1 - a_{\text{BH}})^{0.3}]$. The value ν_{QNM} can be estimated by fitting the plateau of the GW frequency when it reaches its absolute maximum (see Fig. 7.18). A better estimate is provided by the frequency of the Ψ^4 waveforms because the signal is less noisy and not contaminated

by the integration procedure.

A detailed discussion about the accuracy and detectability of our waveforms for higher resolution and longer simulations can be found in [MTH4].

Now let us have a look at convergence of the waves. In the end this is the important thing if one want to extract waves and predict if they are correct. The waveforms are produced with the cold EoS for the runs H1, H2 and H3. Fig. 7.15 shows the real part of $r\Psi_{22}^4$ for the different resolutions. We focus on the inspiral part of the wave. We do not expect good convergence during the merger phase since the convergence order of our method drops to first order. Similar results are found for the series H0, H1 and H2, with larger absolute errors.

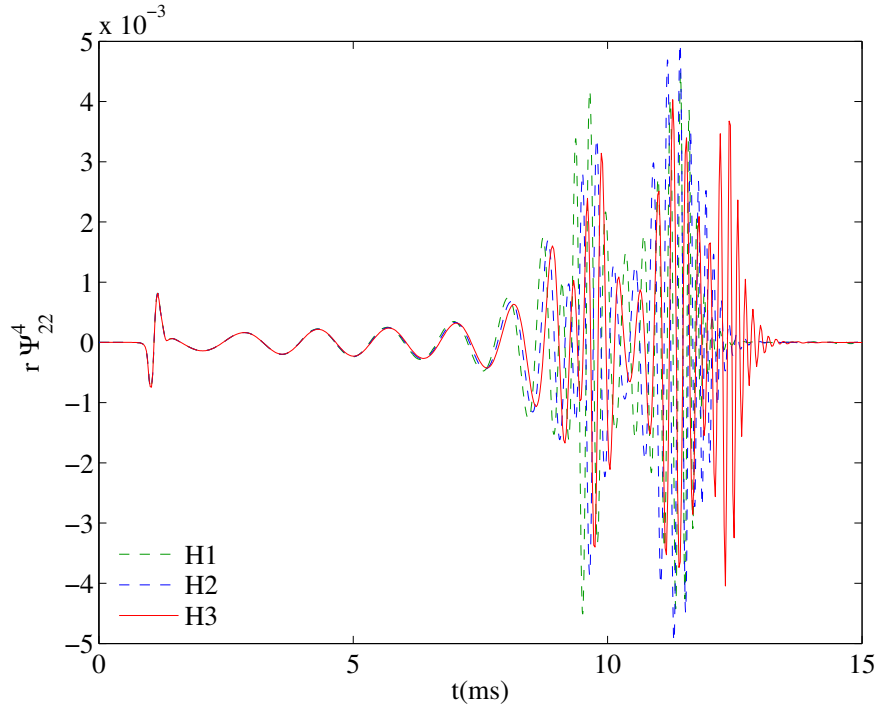


Figure 7.15.: Ψ^4 waveforms from cold evolution at different resolutions. The figure shows the real part of the $r\Psi_{22}^4$ waveform extracted at $r = 294$ km from runs H1-3.

Fig. 7.16 displays the (logarithmic) differences between the $r\Psi_{22}^4$ amplitude (top panel) and phase (bottom panel). In both panels I scale the difference between H2 and H3 for second order convergence. The vertical line in the figure marks the merger time as computed from the waveforms extrapolated in resolution. We display only the

time after the initial junk radiation and before the merger. Inside this time interval, I observe a quite clear 2nd order convergence in the amplitude while for the phase the convergence appears slower. As one can see the phase error is the dominant error. Computing the experimental convergence rate for the phase gives a factor between 1 and 2. This suggests that we are not yet in the convergence regime. Therefore we have to go to higher resolutions or higher order numerical methods. Here a proper time shift of the waveform may give better convergence. I prefer not to perform such a procedure in order to keep the analysis simple and clean. This method is used several times, for example in BBH simulation and even in the more complicated cases of unequal masses and spins, see e.g. [137, 86, 111].

After the merger convergence of the waves is lost. There is an improvement of several global quantities like the constraint violations in the post-merger phase (see e.g. Fig. 7.4). However it is not possible to show clear convergence. The convergence of the wave amplitude drops to first order, the phase on the other side shows over convergence. Looking directly at $r\Psi^4$ in Fig. 7.15 gives a monotonic dependence on resolution.

Since we have clear convergence in the waves it is possible to make a statement about an error estimate by using Richardson extrapolation. The method is used to compute amplitude and phase at spatial infinity. Results concerning the maximum error estimated during the inspiral are reported in Tab. 7.4. When we use four resolutions (H0-3) and assume 2nd order convergence, the maximum phase and amplitude error are about $\max \delta\phi \sim 0.3$ rad and $\max \delta A/A \sim 7$ %. Assuming that we have 1st order convergence results in larger errors, namely $\max \delta\phi \sim 1$ rad and $\max \delta A/A \sim 24$ %. On the other hand if we consider only the waves for the three highest resolutions (H1-3) again assuming 2nd order convergence we obtain $\max \delta\phi \sim 0.6$ rad and $\max \delta A/A \sim 14$ %. For 1st order we get $\max \delta\phi \sim 1.2$ rad but an unacceptable amplitude error. Furthermore we note that the assumption of 1st order leads to an evidently non realistic estimate of the merger time for the extrapolated data $t_m = 2280$ (11.23 ms). For 2nd order we get a more reasonable value of $t_m = 1800$ (8.87 ms). Here we used only the three highest resolutions (H1-3).

Some care is needed in interpreting these results in the context of the previous discussion. From our results we conclude that: (i) the series H0-2 is too inaccurate and is not reliable for error estimates; (ii) assuming 1st order convergence the series H0-3 is not appropriate and overestimates the actual errors; (iii) assuming 2nd order convergence

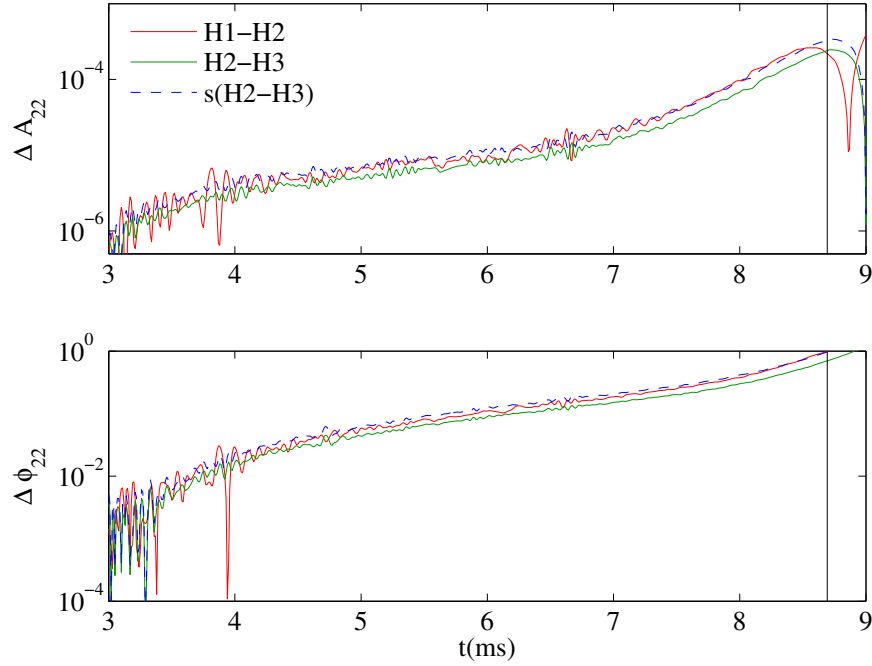


Figure 7.16.: Convergence of phase and amplitude in $r \Psi_{22}^4$ waveform from cold evolution. The figure shows the difference between runs H1 and H2 (blue solid line), between runs H2 and H3 (green solid-dotted line) as well as the difference between H2 and H3 (red dashed line) scaled for 2nd order convergence. Top panel displays the logarithm of amplitude differences, bottom panel displays the logarithm of phase differences. The vertical line indicates the merger.

the series H1-3 gives a conservative and realistic error estimate; (iv) the error of the extrapolated data can be estimated as the difference between the two series (H0-3) and (H1-3), e.g. $\max \delta\phi \sim 0.33$ rad and $\max \delta A/A \sim 7.4\%$. As expected my error is dominated by the fact that I use too little resolution. This was already indicated in [19]. The extraction at the finite radius seems to be a secondary problem. Therefore we did not investigate in errors coming from finite extraction. Going to higher resolutions, however, does improve the picture as indicated in [MTH4].

7.7. Thermal effects in gravitational waves

Finally I discuss the differences between waveforms produced with cold and hot EoS. This was e.g. done by [21], where the results differ from mine. The results refer to

Table 7.4.: Error estimates during inspiral for extrapolated waveforms. Columns: data used for extrapolation, assumed order of convergence, waveform, maximum absolute error in phase, maximum relative error in phase, maximum relative error in amplitude.

data	o	waveform	max $\delta\phi$ [rad]	max $\delta\phi/\phi$ [%]	max $\delta A/A$ [%]
H0-3	2	$r \Psi_{22}^4$	0.29	0.68	6.89
		$r h_{22}$	0.26	0.64	2.65
	1	$r \Psi_{22}^4$	1.04	2.40	24.02
		$r h_{22}$	0.87	2.17	13.31
H1-3	2	$r \Psi_{22}^4$	0.62	1.43	14.30
		$r h_{22}$	0.53	1.32	6.85
	1	$r \Psi_{22}^4$	1.20	2.85	$\gtrsim 100$
		$r h_{22}$	1.10	2.81	$\gtrsim 100$

H1 runs, the waves are shown in Fig. 7.17. As discussed earlier the physics is different in each simulation. Therefore the extracted waves will differ. The phase difference of the waveform h_{22} showing in the lower panel increases monotonically until the merger. Until the first contact both results are quite close, the waveform has accumulated a dephasing of $\Delta\phi = +0.67$ rad and the amplitude is about 6 % smaller. Since these differences are compatible with the truncation errors for this resolution and they are not expected in the continuum limit (the inspiral is an isentropic process from the fluid point of view) they likely have a numerical origin. Thermal effects play a important role after the star contact (see also Fig. 7.8). The dephasing reaches $\Delta\phi = +2.11$ rad at the merger time and the amplitude is about 14 % smaller. Similarly for the $r \Psi_{22}^4$ waveform we found a dephasing of $\Delta\phi = +0.67$ rad and a factor -15 % in amplitude at the contact time and a dephasing of $\Delta\phi = +2.43$ rad and a factor -50 % in amplitude at the merger time. After the merger both waveforms differ totally. The cold EoS has a short tail due to the early collapse. The hot EoS results in a bar-formed HMNS which dominates the signal in this stage. One can see a signal with approximately constant amplitude for around 10 ms. A lower frequency modulation of the signal is visible in the amplitude of the waveform and corresponds to the nonlinear quasi-radial pulsations shown in Fig. 7.9. The high-frequency part of the GW signal is instead dominated by $m = 2$ non-axisymmetric nonlinear modes. The extracted frequencies show different modes around 2.7 kHz. They are slightly changing in time since the HMNS becomes more compact and therefore increases the rotation frequency. A Fourier analysis shows

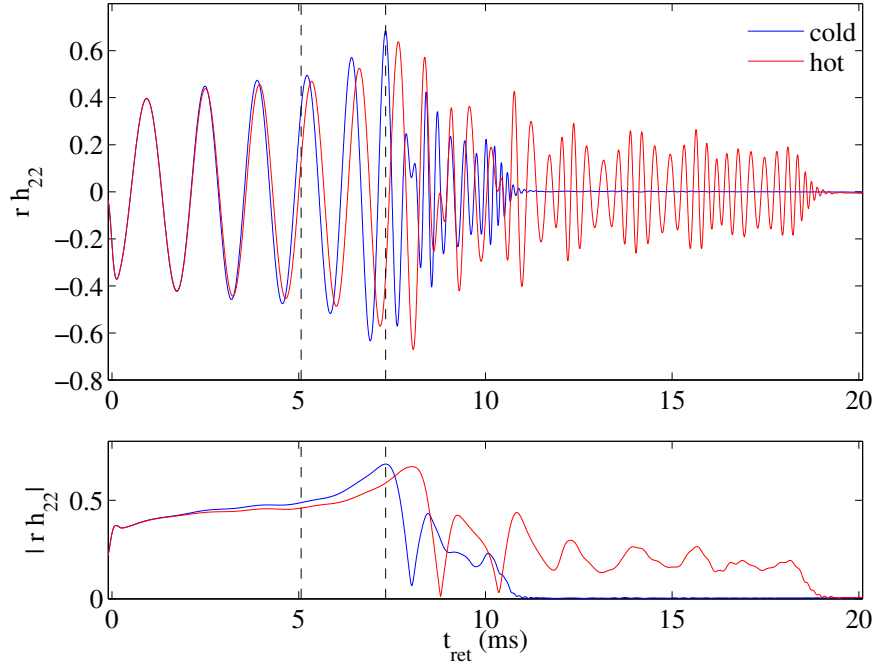


Figure 7.17.: Comparison between waveforms from hot and cold evolutions. The top panel shows the real part of h_{22} extracted at $r = 200$ for the two evolutions. The bottom panel shows the amplitudes. Vertical lines mark the time of the first contact between the stars and the merger time for the cold evolution. The waveforms are plotted against the retarded time $t_{\text{ret}} \equiv t - r_*$. Data refer to run H1.

results qualitatively compatible with [167].

A quite meaningful quantity is the derivative of the GW phase $\omega_{22} \equiv -\mathfrak{I}(\dot{h}_{22}/h_{22})$, which is connected to the dynamics. Fig. 7.18 presents the dimensionless quantity $M\omega_{22}$ computed from simulation using the cold (blue) and the hot (red) EoS. During the inspiral both GW frequencies increase monotonically from $M\omega_{22} \sim 0.056$ to $M\omega_{22} \sim 0.126$. This value (green horizontal solid line, see the bottom panel) is common to both evolutions but occurs at different times due to the accumulated phase difference. After the merger both waveforms have a first maximum with similar values ($M\omega_{22} \sim 0.181$ for cold and $M\omega_{22} \sim 0.184$ for hot EoS), but different time ($t_{\text{ret}} \sim 7.84$ ms for cold and $t_{\text{ret}} \sim 8.68$ ms for hot). Here the waveforms look similar, thermal effects generate only a time shift (retardation). Between the merger and the collapse (formation of the apparent horizon) the GW frequencies are totally dif-

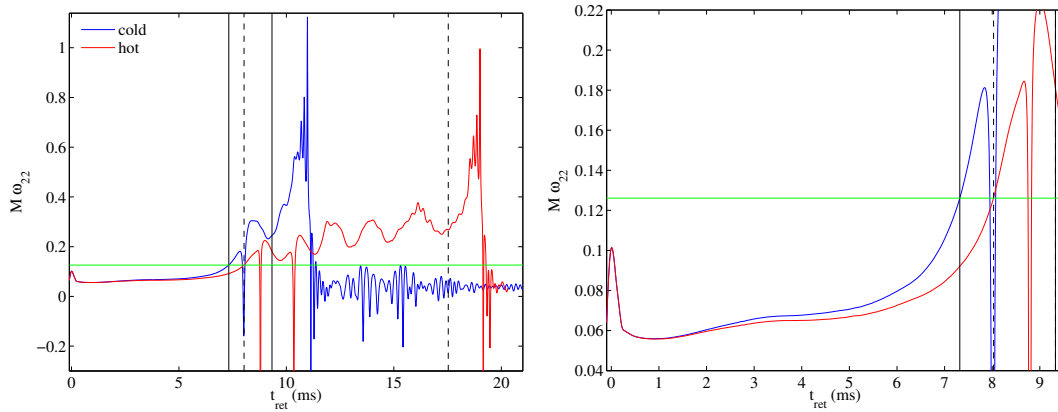


Figure 7.18.: Gravitational wave frequency from hot and cold evolutions. The figure shows $M\omega_{22}$ computed from h_{22} waveforms. In the top panel the blue solid line refers to cold EoS and the red dashed line to hot EoS. The vertical black solid lines mark respectively the merger time and the apparent horizon formation for cold. The vertical black dashed lines mark respectively the merger time and the apparent horizon formation for hot EoS. The bottom panel gives a detail of the top panel showing the inspiral part. The horizontal green solid line marks the value of $M\omega_{22}$ at the merger for cold EoS. Data refer to run H1.

ferent. For cold EoS there is one oscillation and it increases from $M\omega_{22} \sim 0.2$ to $M\omega_{22} \sim 0.245$. In the case of hot EoS the GW frequency reflects the dynamics of the HMNS: it increases almost linearly with large oscillations corresponding to the HMNS quasi-radial oscillations. After the minimum within the last oscillation the collapse happens at a frequency $M\omega_{22} \sim 0.27$.

The collapse phase for both cases are quite similar. The quasi normal mode frequency differs slightly and has a value of $\nu_{\text{QNM}} \sim 6.45$ kHz in case of the hot EoS. After the collapse the amplitude and frequency drops to zero. There is an interesting feature accruing directly after the merger. In both cases the GW frequency becomes negative. At this time the rest-mass density in the equatorial plane is almost-spherical. However it is not clear whether this is physical or only of a numerical nature.

8. Conclusion

In this thesis I implemented a general relativistic hydrodynamic code in the flux-conservative Eulerian formulation coupled to the existing vacuum code BAM . I employed it to investigate numerically neutron star spacetimes in 3+1 dimensions. The main goals were the simulation and extraction of gravitational waves from binary neutron star systems and the gravitational collapse with the puncture gauge. I described the numerical methods which were implemented like the HRSC scheme and tested the framework with three different test scenarios: the shock tube, a stable TOV star and a boosted TOV star.

All tests showed the expected behavior. The shock tube test confirmed that the implementation of the HRSC scheme is correct. I could show that the shape (and all other fields) of the stable star is well conserved for an evolution time of up to 10 ms and the conservation improved with resolution. In case of the norm of the rest-mass density I obtained the expected 2nd order convergence. The proper radial modes of the simulated star agree with results from the literature in the Cowling approximation as well as in full-GR. For all these runs I found that CENO reconstruction gives the best results for conservation and convergence with the smallest truncation errors. The boosted TOV simulations showed that the gauge used has a effect on the shape preservation of the star. Using a non-vanishing damping parameter inside the Gamma-driver condition for the shift results in an expanding coordinate size of the NS. Using vanishing damping preserved the shape of the star most closely. We obtained 2nd order convergence for the boosted star after an evolution of about 4 ms.

Afterwards, I investigated the collapse of a perturbed unstable TOV star simulated in the puncture gauge. I found that this specific gauge provides stable evolutions. The transition from the star to a black hole is handled generically without any artificial numerical assumptions. By comparing it with the numerical evolution of a single puncture using the same gauge, I have shown that the two numerical spacetimes tend

to the same trumpet solution at late times, a possibility already conjectured in [26]. In the order to have a quantitative comparison I used the lapse as a function of trace of the extrinsic curvature and compared the final states of this quantity. The difference between puncture evolution and collapse is less than a few percent. Additionally I compared the final state with the analytic solution for a single puncture and found the same dependency.

At the continuum level the agreement of both end states can not be explained. Investigating two different conditions for the gauge in the matter evolution ($\mu_S = 1$ and $\mu_S = \alpha^2$) showed that the Gamma-driver shift condition forces the matter to rapidly move to the region inside the innermost grid-point by stretching the spatial numerical grid. Thus in the domain covered by the numerical coordinates the spacetimes agree, solving the apparent contradiction. Since the spacetime has lost all matter the final spacetime on the grid is the vacuum Schwarzschild solution. The analysis also demonstrates that I obtain robust numerical evolutions of the collapse when using the puncture gauges with $\mu_S = 1$, however, it is not appropriate for a detailed study of the dynamics of the matter near the singularity.

I furthermore evolved binary neutron star initial data in a quasi-equilibrium configuration and investigated in the dynamics for various resolutions. Increasing resolution have resulted in an improved behavior of all quantities. In particular I found 2nd order convergence during the inspiral phase for the norm of the Hamilton constraint. During this phase I obtained good conservation of the rest-mass with a relative error smaller than 0.5%. After the merger I found an accretion disk around the final black hole. Convergence was lost after the merger which is expected for the numerical scheme employed due to a lack of resolution. Therefore the results are trustworthy only to some extent.

I investigated the effect of different reconstruction methods and found a significant change of the binary neutron star evolution for different methods. The best results in terms of conservation of the star shape was found for CENO reconstruction. I further looked at the influence of different equation of states (hot and cold EoS) and found similar results during the inspiral phase, as expected. However, the behavior differed during the merger phase. The cold EoS showed one oscillation of the hyper massive neutron star (HMNS) before collapsing to a black hole, whereas using a hot EoS results in an oscillating HNMS for around 9 ms before collapsing.

The neutron star dynamics on the grid are effected by the gauge conditions, especially the Gamma-driver shift condition. I compared simulations with different damping coefficients η and obtained coordinate eccentricity when using a non-vanishing η . According to the numerics I found $\eta = 0$ to be the best choice. However, looking at the apparent horizon tells that a value of about $\eta = 0.3$ preserves the coordinate radius best which is appropriate to resolve the final BH.

Finally I investigated gravitational waves from binary neutron star simulations. I used two different integration methods to compute rh_{22} out of the Newman-Penrose scalar Ψ^4 . According to [143] using the fixed-frequency integration gave better results. Applying this method I found reasonable 2nd order convergence in amplitude and phase for the waves during the inspiral. Additionally I made predictions of an error estimate for the waves. Comparing waveforms produced by different equation of states showed that they had different behavior after the merger. While the cold EoS waveform has a short tail the hot EoS waveform has approximately constant amplitude. This can be explained by the bar deformed HMNS.

In total, the BAM code is now able to stably evolve spacetimes containing matter. My simulations of neutron star binaries showed accurate evolutions for more than 25 ms.

A. 3+1 Formalism

A.1. 3+1 splitting

In order to reformulate general relativity as a Cauchy problem, the whole spacetime has to be “split back” into space and time. More rigorously, the manifold representing a globally hyperbolic spacetime is foliated in spacelike hypersurfaces Σ_t . As described in detail in [185, 6] the foliation can be identified by a parameter t which can be considered as a time function. Having two neighbored hypersurfaces Σ_t and Σ_{t+dt} the spacetime between the two slices can be described by three quantities, namely the lapse, the shift and the 3-metric. The lapse α measures the proper time $d\tau$ between both hypersurfaces for an observer moving in normal direction to the hypersurface

$$d\tau = \alpha(t, x^i) dt. \quad (\text{A.1})$$

The shift vector β^i is the relation between Eulerian observers and constant spatial coordinates

$$x^i_{t+dt} = x^i_t - \beta^i(t, x^i) dt. \quad (\text{A.2})$$

And the 3-metric γ_{ij} which measures the proper distance within the hypersurface by

$$dl^2 = \gamma_{ij} dx^i dx^j. \quad (\text{A.3})$$

Having this in mind the line-element of the spacetime can be written as

$$\begin{aligned} ds^2 &= -\alpha^2 dt^2 + \gamma_{ij} (dx^i + \beta^i dt)(dx^j + \beta^j dt) \\ &= (-\alpha^2 + \beta_i \beta^i) dt^2 + 2\beta_i dt dx^i + \gamma_{ij} dx^i dx^j, \end{aligned} \quad (\text{A.4})$$

where we only used the three new variables¹.

The relation between the 4-metric $g_{\mu\nu}$ and the new quantities is given explicitly given by

$$g^{\mu\nu} = \begin{pmatrix} -\alpha^{-2} & \alpha^{-2}\beta^i \\ \alpha^{-2}\beta^j & \gamma^{ij} - \alpha^{-2}\beta^i\beta^j \end{pmatrix}, \quad (\text{A.5})$$

and the inverse by

$$g_{\mu\nu} = \begin{pmatrix} -\alpha^2 + \beta_k\beta^k & \beta_i \\ \beta_j & \gamma_{ij} \end{pmatrix}. \quad (\text{A.6})$$

The normal vector to the hypersurface follows from the given relation

$$n^\mu = \frac{1}{\alpha}(1, -\beta^i), \quad n_\mu = (-\alpha, 0). \quad (\text{A.7})$$

A.2. Extrinsic curvature

Looking at the Einstein equations show that we have an equation second order in space and time. From the numerical point of view it is more convenient to have a system of differential equation which are first order in time. Therefore we introduce a new quantity which is something like the time derivative of the metric. Or in other words the extrinsic curvature describes how the normal vector is changed by parallel transport to a neighboring point in the given slice. In order to define the extrinsic curvature one has to create a projection operator P_ν^μ by

$$P_\nu^\mu := \delta_\nu^\mu + n^\mu n_\nu. \quad (\text{A.8})$$

Now using this operator to define the extrinsic curvature by

$$K_{\mu\nu} := -P_\mu^\sigma \nabla_\sigma n_\nu \quad (\text{A.9})$$

¹Here we used $\beta_i := \gamma_{ij}\beta^j$.

gives a purely spacial and symmetric tensor. Using the definition of the Lie derivative in normal direction the extrinsic curvature can be written as

$$K_{\mu\nu} = -\frac{1}{2}\mathcal{L}_{\vec{n}}\gamma_{\mu\nu}. \quad (\text{A.10})$$

With this we have a quantity which tells how hypersurfaces are immersed in the four-dimensional spacetime. Some analysis show that this relation can lead to an evolution equation for the metric

$$\partial_t\gamma_{ij} = -2\alpha K_{ij} + \nabla_i\beta_j + \nabla_j\beta_i. \quad (\text{A.11})$$

Here the three-dimensional covariant derivative is the projection of the four-dimensional one: $D_\mu := P_\mu^\sigma \nabla_\sigma$. This is the first part of the ADM evolution equations which only depends on the normal vector and the extrinsic curvature. The second part is coming from the contraction of Einstein equations.

A.3. ADM constraint equations

At this point the Einstein equations are not use yet. Writing these equations in the 3+1 form gives two kinds of systems, namely constraint and evolution equations. To gain the constraint equations one has to express the four-dimensional Riemann tensor $R^\alpha{}_{\beta\mu\nu}$ in terms of quantities which only defined inside the hypersurface, like the three-dimensional Riemann tensor ${}^{(3)}R^\alpha{}_{\beta\mu\nu}$ and the extrinsic curvature $K_{\mu\nu}$. The full projection of the Riemann tensor is called the Gauss-Codazzi equations

$$\perp R_{\alpha\beta\mu\nu} = P_\alpha^\delta P_\beta^\kappa P_\mu^\lambda P_\nu^\sigma R_{\delta\kappa\lambda\sigma} = {}^{(3)}R_{\alpha\beta\mu\nu} + K_{\alpha\mu}K_{\beta\nu} - K_{\alpha\nu}K_{\beta\mu}. \quad (\text{A.12})$$

Contracting the Riemann tensor once by the normal vector gives the Codazzi-Mainardi equations

$$\perp R_{\alpha\beta\mu\nu}n^\nu = P_\alpha^\delta P_\beta^\kappa P^\lambda R_{\delta\kappa\lambda\nu}n^\nu = D_\beta K_{\alpha\mu} - D_\alpha K_{\beta\mu}. \quad (\text{A.13})$$

The relation between the Einstein tensor $G_{\mu\nu}$ and Riemann tensor can be given by

$$P^{\alpha\mu}P^{\beta\nu}R_{\alpha\beta\mu\nu} = R + 2n^\mu n^\nu R_{\mu\nu} = 2n^\mu n^\nu G_{\mu\nu}. \quad (\text{A.14})$$

Now using equation (A.12) and (A.13) and plug these into the Einstein equations one gets finally the Hamiltonian and the momentum constraint

$${}^{(3)}R + K^2 + K_{ij}K^{ij} = 16\pi\rho, \quad (\text{A.15})$$

$$D_j (K^{ij} - \gamma^{ij}K) = 8\pi j^i, \quad (\text{A.16})$$

with the definition of the energy density $\rho := n^\mu n^\nu T_{\mu\nu}$ and the momentum density $j^i := -P^{i\mu} n^\nu T_{\mu\nu}$ and the trace of the extrinsic curvature $K = K_i^i$. Both the Hamiltonian and the momentum constraint do not depend on time derivatives or the gauge functions α and β^i . Therefore both equations are independent on the slicing and refer totally to the given hypersurface.

A.4. ADM evolution equations

To yield evolution equations out of the Riemann tensor one has project twice with the normal vector.

$$P_\mu^\delta P_\nu^\kappa n^\lambda n^\sigma R_{\delta\lambda\kappa\sigma} = \mathcal{L}_{\vec{n}} K_{\mu\nu} + K_{\mu\lambda} K_\nu^\lambda + \frac{1}{\alpha} D_\mu D_\nu \alpha. \quad (\text{A.17})$$

Putting this again in the Einstein equations and use equation (A.12) gives at the end an evolution equation for the extrinsic curvature

$$\begin{aligned} \partial_t K_{ij} &= \beta^k \partial_k K_{ij} + K_{ki} \partial_j \beta^k + K_{kj} \partial_i \beta^k - D_i D_j \alpha \\ &+ \alpha [R_{ij} + K K_{ij} - 2K_{ik} K_j^k] + 4\pi\alpha [\gamma_{ij}(S - \rho) - 2S_{ij}]. \end{aligned} \quad (\text{A.18})$$

At this point we used the definition of the spatial stress energy tensor

$$S_{ij} := P_i^\mu P_j^\nu T_{\mu\nu} \quad (\text{A.19})$$

and the trace of this object $S = S_i^i$.

With this we have two sets of evolution equations, namely equation (A.11) and (A.18).

B. Global quantities

B.1. Total mass and momentum

In general relativity there is no meaningful way to define locally energy or momentum. They are well defined in case of flat space. The approach we are using defines both quantities of a asymptotic flat spacetime. The definition is discussed in e.g. [15] and are given by

$$E = \frac{1}{16\pi} \oint_S \sqrt{g} g^{ij} g^{kl} (\partial_j g_{ik} - \partial_k g_{ij}) dS_l, \quad (\text{B.1})$$

$$P^i = \frac{1}{8\pi} \oint_S \sqrt{g} (K_j^i - \delta_j^i K) dS_j, \quad (\text{B.2})$$

$$J^i = \frac{1}{8\pi} \epsilon^{ijk} \oint_S \sqrt{g} x_j (K_{kl} - \delta_{kl} K) dS^l. \quad (\text{B.3})$$

The expressions are called the ADM mass, ADM momentum and ADM angular momentum, where ϵ_{ijk} is the Levi-Civita tensor. These quantities are not expected to give correct results in the strong field regime therefore the integral has to be defined faraway. The correct values can be achieved by integrating at spacial infinity

$$M_{\text{ADM}} = \lim_{r \rightarrow \infty} E(r), \quad (\text{B.4})$$

$$P_{\text{ADM}}^i = \lim_{r \rightarrow \infty} P^i(r), \quad (\text{B.5})$$

$$J_{\text{ADM}}^i = \lim_{r \rightarrow \infty} J^i(r). \quad (\text{B.6})$$

B.2. Gravitational wave extraction

In order to extract gravitational waves we use the Newman-Penrose formalism [134]. It is based on the introduction of a tetrad of null vectors $l^\mu, n^\mu, m^\mu, \bar{m}^\mu$. The Newman-

Penrose scalar Ψ^4 is defined by

$$\Psi^4 = -R_{\mu\nu\rho\sigma} n^\mu \bar{n}^\nu m^\rho \bar{m}^\sigma \quad (\text{B.7})$$

where $R_{\mu\nu\rho\sigma}$ is the Riemann tensor. Here l^μ and n^μ are in and outgoing null-vectors and the complex-valued m^μ is constructed by two spatial vectors. According to [53] we construct the tetrad by a orthonormalized spatial tetrad

$$\begin{aligned} u^i &= (-y, x, 0), \\ v^i &= (x, y, z), \\ w^i &= g^{ij} \epsilon_{jkl} u^k u^l \end{aligned} \quad (\text{B.8})$$

and get

$$\begin{aligned} n^0 &= \frac{1}{\sqrt{2}\alpha}, & n^i &= \frac{1}{\sqrt{2}} \left(-\frac{\beta^i}{\alpha} - v^i \right), \\ l^0 &= \frac{1}{\sqrt{2}\alpha}, & l^i &= \frac{1}{\sqrt{2}} \left(-\frac{\beta^i}{\alpha} + v^i \right), \\ m^0 &= 0, & m^i &= \frac{1}{\sqrt{2}} (u^i + i w^i). \end{aligned} \quad (\text{B.9})$$

The definition of Ψ^4 (B.7) consists out of four dimensional components which have to be expressed by three dimensional quantities given at each time slice. Using the Gauss-Codazzi (A.12) and the (A.13) Codazzi-Mainardi equation yields

$$\perp R_{\mu\nu\rho\sigma} = {}^{(3)}R_{\alpha\beta\mu\nu} + K_{\alpha\mu} K_{\beta\nu} - K_{\alpha\nu} K_{\beta\mu}, \quad (\text{B.10})$$

$$\perp R_{\mu\nu\rho\sigma} n^\mu = D_\rho K_{\nu\sigma} - D_\sigma K_{\nu\rho}, \quad (\text{B.11})$$

$$\perp R_{\mu\nu\rho\sigma} n^\mu n^\rho = {}^{(3)}R_{\nu\sigma} - K_{\nu\lambda} K_\sigma^\lambda + K K_{\mu\sigma}. \quad (\text{B.12})$$

With this the Newman-Penrose scalar is given by

$$\Psi^4 = -\frac{1}{4} (\perp R_{ijkl} v^i v^k - 2 \perp R_{\mu jkl} n^\mu v^k + \perp R_{ij\rho l} n^i n^\rho) (u^j - i w^j) (u^l - i w^l) \quad (\text{B.13})$$

and depends only on the ADM variables in a given time slice.

In order to obtain the contributions of Ψ^4 of the individual modes the scalar is

projected by the spherical harmonics Y_{lm}^{-2} of spin weight -2 given by

$$A_{lm} = \int_0^{2\pi} \int_0^\pi \Psi^4 \bar{Y}_{lm}^{-2} \sin \theta \, d\theta d\phi \quad (\text{B.14})$$

at a finite extraction radius.

B.3. Energy and momentum of gravitational waves

The Newman-Penrose scalar can be used to compute the amount of radiated energy or linear and angular momentum. They are given by

$$\frac{dE}{dt} = \lim_{r \rightarrow \infty} \left[\frac{r^2}{16} \oint_S \left| \int_{-\infty}^t \Psi^4 dt' \right|^2 dS \right], \quad (\text{B.15})$$

$$\frac{dP_i}{dt} = - \lim_{r \rightarrow \infty} \left[\frac{r^2}{16} \oint_S l_i \left| \int_{-\infty}^t \Psi^4 dt' \right|^2 dS \right], \quad (\text{B.16})$$

$$\frac{dJ_z}{dt} = - \lim_{r \rightarrow \infty} \left[\frac{r^2}{16} \Re \left\{ \oint_S \left(\int_{-\infty}^t \int_{-\infty}^{t'} \bar{\Psi}^4 dt'' \right) \left(\partial_\phi \int_{-\infty}^t \Psi^4 dt' \right) dS \right\} \right] \quad (\text{B.17})$$

with $l_i = (-\sin \theta \cos \phi, -\sin \theta \sin \phi, -\cos \theta)$.

C. Different reconstruction methods

C.1. MC2

The VanLeer MONOTONIZED CENTERED (MC2) limiter is given by:

$$\begin{aligned}\Delta_i &= \text{MM} \left[\theta \Delta_i^-, \frac{1}{2}(\Delta_i^+ + \Delta_i^-), \theta \Delta_i^+ \right] \\ &= \begin{cases} \text{sign}(\Delta_i^+) \min(\theta |\Delta_i^-|, \frac{1}{2} |\Delta_i^+ + \Delta_i^-|, \theta |\Delta_i^+|) & \text{if } (\Delta_i^+ \Delta_i^-) > 0 \\ 0 & \text{otherwise} \end{cases} \\ &= \frac{1}{2} [\text{sign}(\Delta_i^-) + \text{sign}(\Delta_i^+)] \min(\theta |\Delta_i^-|, \frac{1}{2} |\Delta_i^+ + \Delta_i^-|, \theta |\Delta_i^+|)\end{aligned}$$

with $\theta \in [1, 2]$.

C.2. PPM

Following [60, 120] the reconstruction procedure of the PPM is composed in 4 steps:

- i. Interpolation: $w_{i+\frac{1}{2}}$ is estimated by differencing a quartic polynomial determined by the five points w_{i-2} , w_{i-1} , ..., w_{i+2} , where the MC limiter is used to constraint the value between w_i and w_{i+1} .
- ii. Contact steepening: a correction to produce narrower profiles near a contact discontinuity. it is applied only on ρ .
- iii. Flattening: a correction to reduce post-shock oscillations.
- iv. Monotonization: to ensure that the final interpolation parabola is a monotone function in the cell.

Step i and iii require 2 ghosts, and this is a general and “minimal” PPM. Then step ii and iii are specifically designed for hydro equations, step ii requires 3 ghosts and the

correct implementation of step iii require 4 ghost points. The method gives formally a 3rd order scheme. In [59] a fully 3rd order PPM method is better implemented in a scheme not field-by-field where cells instead of interfaces are reconstructed.

C.3. CENO3

CENO reconstruction with 3rd order accuracy can be obtained using a quadratic CENO interpolation [108, 186]. The CENO quadratic polynomials around the point i are:

$$Q_i^k(x) = w_j + \Delta_j^0 \frac{x - x_j}{\Delta x} + \frac{1}{2} \Delta_j^2 \left(\frac{x - x_j}{\Delta x} \right)^2 \quad (\text{C.1})$$

where the undivided differences are defined as

$$\begin{aligned} \Delta_j^0 &\equiv \frac{1}{2}(\Delta_j^+ + \Delta_j^-) = \frac{1}{2}(w_{i+1} - w_{i-1}), \\ \Delta_j^2 &\equiv \Delta_j^+ \Delta_j^- = w_{j+1} - 2w_j + w_{j-1}. \end{aligned} \quad (\text{C.2})$$

and $k = -1, 0, 1$, $j = i + k$. Explicitly they read

$$\begin{aligned} Q_i^{-1}(x) &= w_{i-1} + \Delta_{i-1}^0 \frac{x - x_{i-1}}{\Delta x} + \frac{1}{2} \Delta_{i-1}^2 \left(\frac{x - x_{i-1}}{\Delta x} \right)^2, \\ Q_i^0(x) &= w_i + \Delta_i^0 \frac{x - x_i}{\Delta x} + \frac{1}{2} \Delta_i^2 \left(\frac{x - x_i}{\Delta x} \right)^2, \\ Q_i^{+1}(x) &= w_{i+1} + \Delta_{i+1}^0 \frac{x - x_{i+1}}{\Delta x} + \frac{1}{2} \Delta_{i+1}^2 \left(\frac{x - x_{i+1}}{\Delta x} \right)^2, \end{aligned} \quad (\text{C.3})$$

and at point $x = x_{i+\frac{1}{2}}$ (which corresponds to L_i):

$$\begin{aligned}
Q_i^{-1} &= w_{i-1} + \frac{3}{2}\Delta_{i-1}^0 + \frac{9}{8}\Delta_{i-1}^2 \\
&= \frac{1}{8}(3w_{i-2} - 10w_{i-1} + 15w_i), \\
Q_i^0 &= w_i + \frac{1}{2}\Delta_i^0 + \frac{1}{8}\Delta_i^2 \\
&= \frac{1}{8}(-w_{i-1} + 6w_i + 3w_{i+1}), \\
Q_i^{+1} &= w_{i+1} - \frac{1}{2}\Delta_{i+1}^0 + \frac{1}{8}\Delta_{i+1}^2 \\
&= \frac{1}{8}(3w_i + 6w_{i+1} - w_{i+2}).
\end{aligned} \tag{C.4}$$

The CENO ‘‘philosophy’’ then tells what interpolation must be chosen. Namely, first compute the weighted differences

$$d_i^k = \alpha^k(Q_i^k - L_i) \tag{C.5}$$

with $\alpha^{\pm 1} = 1$ and $\alpha^0 = 0.7$ ¹, i.e.

$$\begin{aligned}
d_i^{-1} &= Q_i^{-1} - L_i, \\
d_i^0 &= 0.7(Q_i^0 - L_i), \\
d_i^{+1} &= Q_i^{+1} - L_i
\end{aligned} \tag{C.6}$$

and second reconstruct the value as

$$w^{\text{recon}} = \begin{cases} Q_i^{k_0} & \text{if } \text{sign}(d_i^{-1}) = \text{sign}(d_i^0) = \text{sign}(d_i^1) \\ L_i & \text{otherwise} \end{cases} \tag{C.7}$$

with

$$k_0 : |d_i^{k_0}| = \min_k (|d_i^k|). \tag{C.8}$$

CENO3 reconstruction requires 3 ghost points.

¹The value of $\alpha^0 = 0.7$ is the standard choice in [108, 186]. We found that $\alpha^0 = 0.1$ gives better results (see section 5.2).

List of Publications

- [MTH1] M. THIERFELDER, S. BERNUZZI, D. HILDITCH *et al.* *The trumpet solution from spherical gravitational collapse with puncture gauges.* Phys.Rev., **D83**:064022 (2011)
- [MTH2] M. THIERFELDER, S. BERNUZZI and B. BRÜGMANN. *Numerical relativity simulations of binary neutron stars.* Phys. Rev. D, **84**, 4:044012 (2011)
- [MTH3] M. THIERFELDER and B. BRÜGMANN. *Finding event horizons in multiple black hole simulations* (2011). In preparation
- [MTH4] S. BERNUZZI, M. THIERFELDER and B. BRÜGMANN. *Accuracy of numerical relativity waveforms from binary neutron star mergers and their comparison with post-Newtonian waveforms* (2011)
- [MTH5] R. GOLD, S. BERNUZZI, M. THIERFELDER *et al.* *Eccentric binary neutron star mergers* (2011)

List of Presentations

- [P1] M. THIERFELDER, B. BRÜGMANN and J. GONZÁLES. *Event horizon finder for black holes* (2008). Talk at DPG spring Meeting, Freiburg
- [P2] M. THIERFELDER, B. BRÜGMANN, J. GONZÁLES *et al.* *Finding event horizons in black hole simulations* (2008). Talk at SFB Videoseminar, Jena
- [P3] M. THIERFELDER, B. BRÜGMANN, J. GONZÁLES *et al.* *Finding event horizons in multiple black hole simulations* (2009). Talk at DPG spring Meeting, Muenchen
- [P4] M. THIERFELDER, B. BRÜGMANN, J. GONZÁLES *et al.* *Finding event horizons in multiple black hole simulations* (2009). Talk at Marcel Grossmann Meeting, Paris
- [P5] M. THIERFELDER, W. TICHY, S. BERNUZZI *et al.* *3d matter evolution with the z_4 formulation* (2010). Talk at DPG spring Meeting, Bonn
- [P6] M. THIERFELDER, S. BERNUZZI and B. BRÜGMANN. *Numerical simulations of neutron stars* (2011). Talk at DPG spring Meeting, Karlsruhe

Bibliography

- [1] J. ABADIE, B. P. ABBOTT, R. ABBOTT *et al.* *Search for gravitational-wave inspiral signals associated with short Gamma-Ray Bursts during LIGO's fifth and Virgo's first science run* (2010)
- [2] A. A. ABRAMOVICI, W. ALTHOUSE, R. P. DREVER *et al.* *LIGO: The Laser Interferometer Gravitational-Wave Observatory*. *Science*, **256**:325–333 (1992)
- [3] M. ABRAMOWITZ and I. A. STEGUN. *Handbook of Mathematical Functions*. Dover, New York (1965)
- [4] F. ACERNESE *et al.* *The virgo status*. *Class. Quantum Grav.*, **23**:S635–S642 (2006)
- [5] M. ALCUBIERRE. *Hyperbolic slicings of spacetime: singularity avoidance and gauge shocks*. *Class. Quantum Grav.*, **20**, **4**:607–624 (2003)
- [6] M. ALCUBIERRE. *Introduction to 3+1 Numerical Relativity (International Series of Monographs on Physics)*. Oxford University Press, USA (2008)
- [7] M. ALCUBIERRE, G. ALLEN, B. BRÜGMANN *et al.* *Towards an understanding of the stability properties of the 3+1 evolution equations in general relativity*. *Phys. Rev. D*, **62**:124011 (2000). Gr-qc/9908079
- [8] M. ALCUBIERRE, S. R. BRANDT, B. BRÜGMANN *et al.* *Test-beds and applications for apparent horizon finders in numerical relativity*. *Class. Quantum Grav.*, **17**:2159–2190 (2000)
- [9] M. ALCUBIERRE, B. BRÜGMANN, P. DIENER *et al.* *Gauge conditions for long-term numerical black hole evolutions without excision*. *Phys. Rev. D*, **67**:084023 (2003)
- [10] D. ALIC, L. REZZOLLA, I. HINDER *et al.* *Dynamical damping terms for symmetry-seeking shift conditions*. *Class. Quant. Grav.*, **27**:245023 (2010)
- [11] M. ANDERSON, E. W. HIRSCHMANN, L. LEHNER *et al.* *Magnetized Neutron Star Mergers and Gravitational Wave Signals*. *Phys. Rev. Lett.*, **100**:191101 (2008)
- [12] M. ANDERSON, E. W. HIRSCHMANN, L. LEHNER *et al.* *Simulating binary neutron stars: dynamics and gravitational waves*. *Phys. Rev.*, **D77**:024006 (2008)
- [13] N. ANDERSSON, V. FERRARI, D. JONES *et al.* *Gravitational waves from neutron stars: Promises and challenges* (2009)
- [14] ARNETT and BOWERS. *Astrohys. J. Suppl.*, **415**:415 (1977)
- [15] R. ARNOWITT, S. DESER and C. W. MISNER. *The dynamics of general relativity*.

- In L. WITTEN, ed., *Gravitation: An Introduction to Current Research*, 227–265. Wiley, New York (1962)
- [16] W. BAADE and F. ZWICKY. *Cosmic rays from super-Novae*. Proc. Nat. Acad. Sci. U.S., **20**:259–263 (1934)
- [17] L. BAIOTTI, S. BERNUZZI, G. CORVINO *et al.* *Gravitational-Wave Extraction from Neutron Stars Oscillations: comparing linear and nonlinear techniques*. Phys. Rev., **D79**:024002 (2009)
- [18] L. BAIOTTI, T. DAMOUR, B. GIACOMAZZO *et al.* *Analytic modelling of tidal effects in the relativistic inspiral of binary neutron stars*. Phys.Rev.Lett., **105**:261101 (2010)
- [19] L. BAIOTTI, T. DAMOUR, B. GIACOMAZZO *et al.* *Accurate numerical simulations of inspiralling binary neutron stars and their comparison with effective-one-body analytical models* (2011)
- [20] L. BAIOTTI, R. DE PIETRI, G. M. MANCA *et al.* *Accurate simulations of the dynamical bar-mode instability in full General Relativity*. Phys. Rev., **D75**:044023 (2007)
- [21] L. BAIOTTI, B. GIACOMAZZO and L. REZZOLLA. *Accurate evolutions of inspiralling neutron-star binaries: prompt and delayed collapse to black hole*. Phys. Rev., **D78**:084033 (2008)
- [22] L. BAIOTTI, B. GIACOMAZZO and L. REZZOLLA. *Accurate evolutions of inspiralling neutron-star binaries: assessment of the truncation error*. Class. Quant. Grav., **26**:114005 (2009)
- [23] L. BAIOTTI, I. HAWKE, P. MONTERO *et al.* *A new three-dimensional general-relativistic hydrodynamics code*. In R. CAPUZZO-DOLCETTA, ed., *Computational Astrophysics in Italy: Methods and Tools*, volume 1, 210. Mem. Soc. Astron. It. Suppl., Trieste (2003)
- [24] L. BAIOTTI, I. HAWKE, P. J. MONTERO *et al.* *Three-dimensional relativistic simulations of rotating neutron star collapse to a Kerr black hole*. Phys. Rev. D, **71**:024035 (2005)
- [25] L. BAIOTTI, I. HAWKE and L. REZZOLLA. *On the gravitational radiation from the collapse of neutron stars to rotating black holes*. Class. Quantum Grav., **24** (2007)
- [26] L. BAIOTTI and L. REZZOLLA. *Challenging the paradigm of singularity excision in gravitational collapse*. Phys. Rev. Lett., **97**:141101 (2006)
- [27] L. BAIOTTI, M. SHIBATA and T. YAMAMOTO. *Binary neutron-star mergers with Whisky and SACRA: First quantitative comparison of results from independent general-relativistic hydrodynamics codes*. Phys. Rev., **D82**:064015 (2010)
- [28] J. G. BAKER, W. D. BOGGS, J. CENTRELLA *et al.* *Mergers of nonspinning black-hole binaries: Gravitational radiation characteristics*. Physical Review D,

- 78:044046 (2008)
- [29] J. G. BAKER, J. CENTRELLA, D.-I. CHOI *et al.* *Binary black hole merger dynamics and waveforms.* Phys. Rev. D, **73**:104002 (2006). Gr-qc/0602026
- [30] J. G. BAKER, J. CENTRELLA, D.-I. CHOI *et al.* *Gravitational wave extraction from an inspiraling configuration of merging black holes.* Phys. Rev. Lett., **96**:111102 (2006)
- [31] F. BANYULS, J. A. FONT, J. M. IBÁÑEZ *et al.* *Numerical 3+1 general-relativistic hydrodynamics: A local characteristic approach.* Astrophys. J., **476**:221 (1997)
- [32] T. W. BAUMGARTE, G. B. COOK, M. A. SCHEEL *et al.* *Binary neutron stars in general relativity: Quasiequilibrium models.* Phys. Rev. Lett., **79**:1182–1185 (1997)
- [33] T. W. BAUMGARTE, G. B. COOK, M. A. SCHEEL *et al.* *General relativistic models of binary neutron stars in quasiequilibrium.* Phys. Rev. D, **57**, **12**:7299–7311 (1998)
- [34] T. W. BAUMGARTE and S. L. SHAPIRO. *On the Numerical integration of Einstein's field equations.* Phys. Rev. D, **59**:024007 (1998)
- [35] T. W. BAUMGARTE and S. L. SHAPIRO. *Evolution of rotating supermassive stars to the onset of collapse.* Astrophys. J., **526**:941 (1999)
- [36] A. BAUSWEIN, H. T. JANKA and R. OECHSLIN. *Testing Approximations of Thermal Effects in Neutron Star Merger Simulations* (2010)
- [37] K. BELCZYNSKI, V. KALOGERA, F. A. RASIO *et al.* *On the rarity of double black hole binaries: Consequences for gravitational-wave detection.* Astrophys. J., **662**:504–512 (2007)
- [38] M. J. BERGER and J. OLIGER. *Adaptive mesh refinement for hyperbolic partial differential equations.* J. Comput. Phys., **53**:484–512 (1984)
- [39] S. BERNUZZI and D. HILDITCH. *Constraint violation in free evolution schemes: comparing bssnok with a conformal decomposition of z_4 .* Phys. Rev., **D81**:084003 (2010)
- [40] S. BERNUZZI and A. NAGAR. *Gravitational waves from pulsations of neutron stars described by realistic Equations of State.* Phys. Rev., **D78**:024024 (2008)
- [41] S. BERNUZZI, A. NAGAR and A. ZENGINOGLU. *Binary black hole coalescence in the extreme-mass-ratio limit: testing and improving the effective-one-body multipolar waveform.* Phys.Rev., **D83**:064010 (2011)
- [42] E. BERTI *et al.* *Inspiral, merger and ringdown of unequal mass black hole binaries: A multipolar analysis.* Phys. Rev., **D76**:064034 (2007)
- [43] L. BLANCHET, T. DAMOUR, B. R. IYER *et al.* *Gravitational-Radiation Damping of Compact Binary Systems to Second Post-Newtonian Order.* Phys. Rev. Lett., **74**:3515–3518 (1995)
- [44] C. BONA, J. MASSÓ, E. SEIDEL *et al.* *A New Formalism for Numerical Relativity.* Phys. Rev. Lett., **75**:600–603 (1995)

- [45] C. BONA, J. MASSÓ, E. SEIDEL *et al.* *First order hyperbolic formalism for numerical relativity*. Phys. Rev. D, **56**:3405–3415 (1997). Gr-qc/9709016
- [46] S. BONAZZOLA, E. GOURGOULHON and J.-A. MARCK. *Evolutionary sequences of irrotational binary neutron stars*. Proceedings of the 19th Texas Symposium (1998). Gr-qc/9904040
- [47] S. BRANDT and B. BRÜGMANN. *A simple construction of initial data for multiple black holes*. Phys. Rev. Lett., **78**, **19**:3606–3609 (1997)
- [48] B. BRÜGMANN. *Adaptive mesh and geodesically sliced Schwarzschild spacetime in 3+1 dimensions*. Phys. Rev. D, **54**, **12**:7361–7372 (1996)
- [49] B. BRÜGMANN. *Binary black hole mergers in 3d numerical relativity*. Int. J. Mod. Phys., **8**:85–100 (1999)
- [50] B. BRÜGMANN. *Binary black hole mergers in 3D numerical relativity*. Int. J. Mod. Phys. D, **8**:85 (1999)
- [51] B. BRÜGMANN. *Schwarzschild black hole as moving puncture in isotropic coordinates*. Gen. Rel. Grav., **41**:2131–2151 (2009)
- [52] B. BRÜGMANN, J. A. GONZÁLEZ, M. HANNAM *et al.* *Calibration of Moving Puncture Simulations*. Phys. Rev., **D77**:024027 (2008)
- [53] B. BRÜGMANN, J. A. GONZÁLEZ, M. HANNAM *et al.* *Exploring black hole superkicks*. Phys. Rev., **D77**:124047 (2008)
- [54] B. BRÜGMANN, W. TICHY and N. JANSEN. *Numerical simulation of orbiting black holes*. Phys. Rev. Lett., **92**:211101 (2004)
- [55] M. CAMPANELLI, C. O. LOUSTO, P. MARRONETTI *et al.* *Accurate evolutions of orbiting black-hole binaries without excision*. Phys. Rev. Lett., **96**:111101 (2006)
- [56] S. M. CARROLL. *Spacetime and Geometry: An Introduction to General Relativity*. Benjamin Cummings (2003)
- [57] B. CARTER. *General Relativity: An Einstein Centenary Survey*. Cambridge University Press, Cambridge, England (1979)
- [58] M. W. CHOPTUIK. *Universality and scaling in gravitational collapse of massless scalar field*. Phys. Rev. Lett., **70**:9 (1993)
- [59] P. COLELLA and M. D. SEKORA. *Short note: A limiter for ppm that preserves accuracy at smooth extrema*. J. Comput. Phys., **227**, **15**:7069–7076 (2008)
- [60] P. COLELLA and P. R. WOODWARD. *The Piecewise Parabolic Method (PPM) for Gas Dynamical Simulations*. J. Comput. Phys., **54**:174–201 (1984)
- [61] G. B. COOK. *Initial data for numerical relativity*. Living Rev. Relativity, **3**:5 (2000)
- [62] I. CORDERO-CARRIÓN, P. CERDÁ-DURÁN, H. DIMMELMEIER *et al.* *Improved constrained scheme for the einstein equations: An approach to the uniqueness issue*. Phys. Rev. D, **79**, **2**:024017 (2009)

- [63] T. DAMOUR and A. NAGAR. *Effective One Body description of tidal effects in inspiralling compact binaries*. Phys. Rev., **D81**:084016 (2010)
- [64] T. DAMOUR, A. NAGAR, M. HANNAM *et al.* *Accurate effective-one-body waveforms of inspiralling and coalescing black-hole binaries*. Phys. Rev., **D78**:044039 (2008)
- [65] H. DIMMELMEIER, J. A. FONT and E. MÜLLER. *Relativistic simulations of rotational core collapse. I. Methods, initial models, and code tests*. Astron. Astrophys., **388**:917–935 (2002)
- [66] M. D. DUEZ, Y. T. LIU, S. L. SHAPIRO *et al.* *Relativistic magnetohydrodynamics in dynamical spacetimes: Numerical methods and tests* (2005). Astro-ph/0503420
- [67] F. ECHEVERRÍA. *Gravitational-wave measurements of mass and angular momentum of a black hole*. Phys. Rev. D, **40**:3194 (1989)
- [68] B. EINFELDT. *On Godunov-type methods for gas dynamics*. SIAM J. Numer. Anal., **25**:294–318 (1988)
- [69] ERIC GOURGOULHON, PHILIPPE GRANDCLMENT, JEAN-ALAIN MARCK, JRME NOVAK AND KEISUKE TANIGUCHI. *Paris Observatory, Meudon section - LUTH laboratory*. [Http://www.lorene.obspm.fr/](http://www.lorene.obspm.fr/)
- [70] J. A. FONT. *Numerical hydrodynamics and magnetohydrodynamics in general relativity*. Living Rev. Relativity, **11**:7 (2007)
- [71] J. A. FONT, T. GOODALE, S. IYER *et al.* *Three-dimensional general relativistic hydrodynamics. II. Long-term dynamics of single relativistic stars*. Phys. Rev. D, **65**:084024 (2002)
- [72] J. A. FONT, M. MILLER, W. M. SUEN *et al.* *Three-dimensional numerical general relativistic hydrodynamics: Formulations, methods, and code tests*. Phys. Rev. D, **61**:044011 (2000)
- [73] J. A. FONT, N. STERGIOLAS and K. D. KOKKOTAS. *Nonlinear hydrodynamical evolution of rotating relativistic stars: Numerical methods and code tests*. Mon. Not. R. Astron. Soc., **313**:678 (2000)
- [74] D. GARFINKLE, C. GUNDLACH and D. HILDITCH. *Comments on Bona-Masso type slicing conditions in long-term black hole evolutions*. Class. Quant. Grav., **25**:075007 (2008)
- [75] C. W. GEAR. *Numerical Initial Value Problems in Ordinary Differential Equations*. Prentice-Hall, Englewood Cliffs (1971)
- [76] B. GIACOMAZZO, L. REZZOLLA and L. BAIOTTI. *Can magnetic fields be detected during the inspiral of binary neutron stars?* Mon. Not. Roy. Astron. Soc., **399**:L164–L168 (2009)
- [77] B. GIACOMAZZO, L. REZZOLLA and L. BAIOTTI. *Accurate evolutions of inspiralling and magnetized neutron-stars: equal-mass binaries*. Phys. Rev., **D83**:044014 (2011)

- [78] E. GOURGOULHON. *Construction of initial data for 3+1 numerical relativity* (2007)
- [79] E. GOURGOULHON, P. GRANDCLÉMENT, K. TANIGUCHI *et al.* *Quasiequilibrium sequences of synchronized and irrotational binary neutron stars in general relativity: Method and tests.* Phys. Rev. D, **63**:064029 (2001)
- [80] E. GOURGOULHON, P. GRANDCLÉMENT, K. TANIGUCHI *et al.* *Quasiequilibrium sequences of synchronized and irrotational binary neutron stars in general relativity: Method and tests.* Phys. Rev. D, **63**:064029 (2001)
- [81] C. GUNDLACH. *Pseudo-spectral apparent horizon finders: an efficient new algorithm.* Phys. Rev. D, **57**, **2**:863–875 (1998)
- [82] C. GUNDLACH. *Pseudo-spectral apparent horizon finders: An efficient new algorithm.* Phys. Rev. D, **57**:863–875 (1998)
- [83] B. GUSTAFSSON, H.-O. KREISS and J. OLIGER. *Time dependent problems and difference methods.* Wiley, New York (1995)
- [84] M. HANNAM, S. HUSA, J. A. GONZÁLEZ *et al.* *Where post-Newtonian and numerical-relativity waveforms meet.* Phys. Rev. D, **77**:044020 (2008)
- [85] M. HANNAM, S. HUSA, F. OHME *et al.* *Wormholes and trumpets: the Schwarzschild spacetime for the moving-puncture generation.* Phys. Rev., **D78**:064020 (2008)
- [86] M. HANNAM, S. HUSA, F. OHME *et al.* *Simulations of black-hole binaries with unequal masses or nonprecessing spins: Accuracy, physical properties, and comparison with post-newtonian results.* Phys. Rev., **D82**:124008 (2010)
- [87] M. HANNAM, S. HUSA, D. POLLNEY *et al.* *Geometry and regularity of moving punctures.* Phys. Rev. Lett., **99**:241102 (2007)
- [88] B. K. HARRISON, K. S. THORNE, M. WAKANO *et al.* *Gravitation Theory and Gravitational Collapse.* Univers. Chicago Press, Chicago (1965)
- [89] A. HARTEN, B. ENQUIST, S. OSHER *et al.* *Uniformly high order accurate essentially non-oscillatory schemes III.* J. Comput. Phys., **71**:2311 (1987)
- [90] A. HARTEN, P. D. LAX and B. VAN LEER. SIAM Rev., **25**:35 (1983)
- [91] I. HAWKE, F. LÖFFLER and A. NEROZZI. *Excision methods for high resolution shock capturing schemes applied to general relativistic hydrodynamics.* Phys. Rev. D, **71**:104006 (2005)
- [92] A. HEWISH, S. J. BELL, J. D. H. PILKINGTON *et al.* *Observation of a rapidly pulsating radio source.* Nature, **217**:709–713 (1968)
- [93] T. HINDERER, B. D. LACKEY, R. N. LANG *et al.* *Tidal deformability of neutron stars with realistic equations of state and their gravitational wave signatures in binary inspiral.* Phys. Rev., **D81**:123016 (2010)
- [94] T. Y. HOU and P. G. LEFLOCH. *Why Nonconservative Schemes Converge to Wrong Solutions: Error Analysis.* Math. Comp., **62**:497–530 (1994)

- [95] S. HUSA, J. A. GONZÁLEZ, M. HANNAM *et al.* *Reducing phase error in long numerical binary black hole evolutions with sixth order finite differencing.* *Class. Quantum Grav.*, **25**:105006 (2008)
- [96] G. JIANG. *Efficient Implementation of Weighted ENO Schemes.* *J. Comp. Phys.*, **126**:202–228 (1996)
- [97] K. KIUCHI, Y. SEKIGUCHI, M. SHIBATA *et al.* *Longterm general relativistic simulation of binary neutron stars collapsing to a black hole.* *Phys. Rev.*, **D80**:064037 (2009)
- [98] K. KIUCHI, Y. SEKIGUCHI, M. SHIBATA *et al.* *Exploring binary-neutron-star-merger scenario of short-gamma-ray bursts by gravitational-wave observation.* *Phys.Rev.Lett.*, **104**:141101 (2010)
- [99] K. D. KOKKOTAS and J. RUOFF. *Radial oscillations of neutron stars.* *Astron. Astroph.*, **366**:565 (2001). Gr-qc/0011093
- [100] H. O. KREISS and J. OLIGER. *Methods for the approximate solution of time dependent problems.* GARP publication series No. 10, Geneva (1973)
- [101] A. KURGANOV and E. TADMOR. *New high-resolution central schemes for nonlinear conservation laws and convection-diffusion equations.* *J. Comp. Phys.*, **160**:214–282 (2000)
- [102] P. D. LAX and B. WENDROFF. *Systems of conservation laws.* *Commun. Pure Appl. Math.*, **13**:217–237 (1960)
- [103] W. H. LEE and E. RAMIREZ-RUIZ. *The Progenitors of Short Gamma-Ray Bursts.* *New J. Phys.*, **9**:17 (2007)
- [104] R. J. LEVEQUE. *Numerical Methods for Conservation Laws.* Birkhauser Verlag, Basel (1992)
- [105] R. J. LEVEQUE. *Finite Volume Methods for Hyperbolic Problems.* Cambridge University Press (2002)
- [106] A. LICHNEROWICZ. *Relativistic Hydrodynamics and Magnetohydrodynamics* (1967)
- [107] L. LINDBLOM, M. A. SCHEEL, L. E. KIDDER *et al.* *A new generalized harmonic evolution system.* *Class. Quantum Grav.*, **23**:S447–S462 (2006)
- [108] X. LIU and S. OSHER. *Convex eno high order multi-dimensional schemes without field by field decomposition or staggered grids.* *J. Comput. Phys.*, **142**:304–330 (1998)
- [109] Y. T. LIU, S. L. SHAPIRO, Z. B. ETIENNE *et al.* *General relativistic simulations of magnetized binary neutron star mergers.* *Phys. Rev.*, **D78**:024012 (2008)
- [110] C. O. LOUSTO, H. NAKANO, Y. ZLOCHOWER *et al.* *Intermediate-mass-ratio black hole binaries: intertwining numerical and perturbative techniques.* *Phys. Rev.*, **D82**:104057 (2010)
- [111] C. O. LOUSTO, H. NAKANO, Y. ZLOCHOWER *et al.* *Intermediate mass ratio*

- black hole binaries: Numerical relativity meets perturbation theory.* Phys. Rev. Lett., **104**:211101 (2010)
- [112] C. O. LOUSTO and Y. ZLOCHOWER. *Orbital evolution of extreme-mass-ratio black-hole binaries with numerical relativity.* Phys. Rev. Lett., **106**:041101 (2011)
- [113] A. LUCAS-SERRANO, J. A. FONT, J. M. IBANEZ *et al.* *Assessment of a high-resolution central scheme for the solution of the relativistic hydrodynamics equations.* Astron. Astrophys., **428**:703–715 (2004)
- [114] C. B. MACDONALD and S. J. RUUTH. *Level set equations on surfaces via the Closest Point Method.* J. Sci. Comput., **35**, **2–3**:219–240 (2008). Doi:10.1007/s10915-008-9196-6
- [115] G. M. MANCA, L. BAIOTTI, R. DE PIETRI *et al.* *Dynamical non-axisymmetric instabilities in rotating relativistic stars.* Class. Quant. Grav., **24**:S171–S186 (2007)
- [116] P. MARRONETTI, G. J. MATHEWS and J. R. WILSON. *Binary neutron-star systems: From the Newtonian regime to the last stable orbit.* Phys. Rev. D, **58**:107503 (1998)
- [117] P. MARRONETTI, G. J. MATHEWS and J. R. WILSON. *Irrotational binary neutron stars in quasi-equilibrium.* Phys. Rev. D, **60**:087301 (1999)
- [118] P. MARRONETTI and S. L. SHAPIRO. *Relativistic models for binary neutron stars with arbitrary spins.* Phys. Rev., **D68**:104024 (2003)
- [119] J. M. MARTÍ and E. MÜLLER. *The analytical solution of the riemann problem in relativistic hydrodynamics.* J. Fluid Mech., **258**:317–333 (1994)
- [120] J. M. MARTÍ and E. MÜLLER. *Extension of the piecewise parabolic method to one-dimensional relativistic hydrodynamics.* J. Comput. Phys., **123**:1–14 (1996)
- [121] J. M. MARTÍ and E. MÜLLER. *Numerical hydrodynamics in special relativity.* Living Rev. Relativity, **2**:3 (1999)
- [122] G. MATHEWS, P. MARRONETTI and J. WILSON. *Relativistic hydrodynamics in close binary systems: Analysis of neutron-star collapse.* Phys. Rev. D, **58**:043003 (1998)
- [123] G. MATHEWS and J. WILSON. *Revised relativistic hydrodynamical model for neutron star binaries.* Phys. Rev. D, **61**:127304 (2000)
- [124] B. D. METZGER, D. GIANNIOS, T. A. THOMPSON *et al.* *The Proto-Magnetar Model for Gamma-Ray Bursts* (2010)
- [125] M. MILLER, P. GRESSMAN and W.-M. SUEN. *Towards a realistic neutron star binary inspiral: Initial data and multiple orbit evolution in full general relativity.* Phys. Rev. D, **69**:064026 (2004)
- [126] C. W. MISNER, K. S. THORNE and J. A. WHEELER. *Gravitation.* W. H. Freeman, San Francisco (1973)
- [127] D. MÜLLER and B. BRÜGMANN. *Toward a dynamical shift condition for unequal mass black hole binary simulations.* Class. Quant. Grav., **27**:114008 (2010)

- [128] D. MÜLLER, J. GRIGSBY and B. BRÜGMANN. *Dynamical shift condition for unequal mass black hole binaries*. Phys. Rev., **D82**:064004 (2010)
- [129] T. NAKAMURA. *General Relativistic Collapse of Axially Symmetric Stars Leading to the Formation of Rotating Black Holes*. Prog. Theor. Phys., **65**:1876–1890 (1981)
- [130] T. NAKAMURA, K. OOHARA and Y. KOJIMA. *General relativistic collapse to black holes and gravitational waves from black holes*. Prog. Theor. Phys. Suppl., **90**:1–218 (1987)
- [131] E. NAKAR. *Short-hard gamma-ray bursts*. Phys. Rept., **442**:166–236 (2007)
- [132] D. NEILSEN, E. W. HIRSCHMANN and R. S. MILLWARD. *Relativistic MHD and black hole excision: Formulation and initial tests*. Class. Quant. Grav., **23**:S505 (2006)
- [133] H. NESSYAHU and E. TADMOR. *Non-oscillatory central differencing for hyperbolic conservation laws*. J. Comp. Phys., **87**:408463 (1990)
- [134] E. T. NEWMAN and R. PENROSE. *An approach to gravitational radiation by a method of spin coefficients*. J. Math. Phys., **3**, **3**:566–578 (1962). Erratum in J. Math. Phys. 4, 998 (1963)
- [135] R. OECHSLIN and H. T. JANKA. *Gravitational waves from relativistic neutron star mergers with nonzero-temperature equations of state*. Phys. Rev. Lett., **99**:121102 (2007)
- [136] F. ÖZEL and D. PSALTIS. *Reconstructing the neutron-star equation of state from astrophysical measurements*. Phys. Rev. D, **80**, **10**:103003 (2009)
- [137] D. POLLNEY, C. REISSWIG, E. SCHNETTER *et al.* *High accuracy binary black hole simulations with an extended wave zone*. Phys. Rev., **D83**:044045 (2011)
- [138] D. POLLNEY *et al.* *Recoil velocities from equal-mass binary black-hole mergers: a systematic investigation of spin-orbit aligned configurations*. Phys. Rev., **D76**:124002 (2007)
- [139] W. H. PRESS, S. A. TEUKOLSKY, W. T. VETTERLING *et al.* *Numerical Recipes 3rd Edition: The Art of Scientific Computing*. Cambridge University Press, New York, NY, USA, 3rd edition (2007)
- [140] F. PRETORIUS. *Evolution of binary black hole spacetimes*. Phys. Rev. Lett., **95**:121101 (2005)
- [141] J. S. READ, B. D. LACKEY, B. J. OWEN *et al.* *Constraints on a phenomenologically parameterized neutron-star equation of state*. Phys.Rev., **D79**:124032 (2009)
- [142] J. S. READ, C. MARKAKIS, M. SHIBATA *et al.* *Measuring the neutron star equation of state with gravitational wave observations*. Phys. Rev., **D79**:124033 (2009)
- [143] C. REISSWIG and D. POLLNEY. *Notes on the integration of numerical relativity waveforms* (2010)

- [144] L. REZZOLLA, B. GIACOMAZZO, L. BAIOTTI *et al.* *The missing link: Merging neutron stars naturally produce jet-like structures and can power short Gamma-Ray Bursts* (2011)
- [145] O. RINNE. *Axisymmetric numerical relativity*. Ph.D. thesis, University of Cambridge, Cambridge, England (2005). Gr-qc/0601064
- [146] O. RINNE. *An axisymmetric evolution code for the Einstein equations on hyperboloidal slices*. *Class. Quant. Grav.*, **27**:035014 (2010)
- [147] O. RINNE, L. LINDBLOM and M. A. SCHEEL. *Testing outer boundary treatments for the Einstein equations*. *Class. Quant. Grav.*, **24**:4053–4078 (2007)
- [148] S. ROSSWOG and M. B. DAVIES. *High Resolution Calculations of Merging Neutron Stars I: Model Description and Hydrodynamic Evolution*. *Mon. Not. Roy. Astron. Soc.*, **345**:1077 (2003)
- [149] S. ROSSWOG, E. RAMIREZ-RUIZ and M. B. DAVIES. *High Resolution Calculations of Merging Neutron Stars III: Gamma-Ray Bursts* (2003)
- [150] M. RUFFERT, H.-T. JANKA and G. SCHÄFER. *Coalescing neutron stars – a step towards physical models. i. hydrodynamic evolution and gravitational-wave emission*. *Astron. Astrophys.*, **311**:532 (1996)
- [151] M. RUFFERT, H.-T. JANKA, K. TAKAHASHI *et al.* *Coalescing neutron stars – a step towards physical models, II. neutrino emission, neutron tori, and gamma-ray bursts*. *Astron. Astrophys.*, **319**:122–153 (1997)
- [152] M. RUIZ, D. HILDITCH and S. BERNUZZI. *Constraint preserving boundary conditions for the $z4c$ formulation of general relativity*. *Phys. Rev.*, **D83**:024025 (2011)
- [153] O. SARBACH, G. CALABRESE, J. PULLIN *et al.* *Hyperbolicity of the BSSN system of Einstein evolution equations*. *Phys. Rev. D*, **66**:064002 (2002)
- [154] B. S. SATHYAPRAKASH and B. F. SCHUTZ. *Physics, Astrophysics and Cosmology with Gravitational Waves*. *Living Rev. Rel.*, **12**:2 (2009)
- [155] W. E. SCHIESSER. *The Numerical Method of Lines: Integration of Partial Differential Equations*. Academic Press, New York (1991)
- [156] E. SCHNETTER. *Time Step Size Limitation Introduced by the BSSN Gamma Driver*. *Class. Quant. Grav.*, **27**:167001 (2010)
- [157] Y. SEKIGUCHI. *An implementation of the microphysics in full general relativity : General relativistic neutrino leakage scheme* (2010)
- [158] Y. SEKIGUCHI. *Stellar core collapse in full general relativity with microphysics - Formulation and Spherical collapse test -*. *Prog. Theor. Phys.*, **124**:331–379 (2010)
- [159] S. L. SHAPIRO and S. A. TEUKOLSKY. *Relativistic stellar dynamics on the computer. I. Motivation and numerical method*. *Astrophys. J.*, **298**:34–57 (1985)
- [160] M. SHIBATA. *A relativistic formalism for computation of irrotational binary stars in quasi equilibrium states*. *Phys. Rev. D*, **58**:024012 (1998)

- [161] M. SHIBATA, T. W. BAUMGARTE and S. L. SHAPIRO. *The bar-mode instability in differentially rotating neutron stars: Simulations in full general relativity*. *Astrophys. J.*, **542**:453–463 (2000)
- [162] M. SHIBATA and T. NAKAMURA. *Evolution of three-dimensional gravitational waves: Harmonic slicing case*. *Phys. Rev. D*, **52**:5428–5444 (1995)
- [163] M. SHIBATA, K. TANIGUCHI and K. URYŪ. *Merger of binary neutron stars with realistic equations of state in full general relativity*. *Phys. Rev. D*, **71**:084021 (2005)
- [164] M. SHIBATA and K. URYŪ. *Simulation of merging binary neutron stars in full general relativity: Gamma=2 case*. *Phys. Rev. D*, **61**:064001 (2000). Gr-qc/9911058
- [165] C. W. SHU and S. J. OSHER. *Efficient implementation of essentially non-oscillatory shock-capturing schemes, i*. *J. Comput. Phys.*, **77**:439 (1988)
- [166] C. W. SHU and S. J. OSHER. *Efficient implementation of essentially non-oscillatory shock-capturing schemes, ii*. *J. Comput. Phys.*, **83**:32 (1989)
- [167] N. STERGIIOULAS, A. BAUSWEIN, K. ZAGKOURIS *et al.* *Gravitational waves and nonaxisymmetric oscillation modes in mergers of compact object binaries* (2011)
- [168] K. TANIGUCHI and E. GOURGOULHON. *Phys. Rev. D*, **65**:44027 (2002)
- [169] K. TANIGUCHI and E. GOURGOULHON. *Quasiequilibrium sequences of synchronized and irrotational binary neutron stars in general relativity. III: Identical and different mass stars with gamma = 2*. *Phys. Rev.*, **D66**:104019 (2002)
- [170] K. TANIGUCHI and E. GOURGOULHON. *Phys. Rev. D*, **68**:124025 (2003)
- [171] D. TATSUMI *et al.* *Current status of Japanese detectors*. *Class. Quant. Grav.*, **24**:S399–S404 (2007)
- [172] A. TCHEKHOVSKOY, J. C. MCKINNEY and R. NARAYAN. *WHAM: A WENO-based general relativistic numerical scheme I: Hydrodynamics*. *Mon. Not. Roy. Astron. Soc.*, **379**:469–497 (2007)
- [173] S. TEUKOLSKY. *Irrotational binary neutron stars in quasi-equilibrium in general relativity*. *Astrophys. J.*, **504**:442–449 (1998)
- [174] K. S. THORNE. *Relativistic radiative transfer - Moment formalisms*. *Mon. Not. Roy. Astron. Soc.*, **194**:439–473 (1981)
- [175] W. TICHY. *Long term black hole evolution with the BSSN system by pseudo-spectral methods*. *Phys. Rev.*, **D80**:104034 (2009)
- [176] R. C. TOLMAN. *Static solutions of Einstein's field equations for spheres of fluids*. *Phys. Rev.*, **55**:364 (1939)
- [177] E. F. TORO. *Riemann Solvers and Numerical Methods for Fluid Dynamics*. Springer-Verlag (1999)
- [178] K. URYU and Y. ERIGUCHI. *A new numerical method for constructing quasi-equilibrium sequences of irrotational binary neutron stars in general relativity*. *Phys. Rev.*, **D61**:124023 (2000)

- [179] K. URYU, F. LIMOUSIN, J. L. FRIEDMAN *et al.* *Binary neutron stars in a waveless approximation*. Phys. Rev. Lett., **97**:171101 (2006)
- [180] K. URYU, F. LIMOUSIN, J. L. FRIEDMAN *et al.* *Non-conformally flat initial data for binary compact objects*. Phys. Rev., **D80**:124004 (2009)
- [181] R. M. WALD. *General relativity*. The University of Chicago Press, Chicago (1984)
- [182] B. WILLKE. *GEO600: Status and plans*. Class. Quant. Grav., **24**:S389–S397 (2007)
- [183] J. R. WILSON and G. J. MATHEWS. *Relativistic hydrodynamics.*, 306–314 (1989)
- [184] T. YAMAMOTO, M. SHIBATA and K. TANIGUCHI. *Simulating coalescing compact binaries by a new code SACRA* (2008)
- [185] J. W. YORK. *Kinematics and dynamics of general relativity*. In L. L. SMARR, ed., *Sources of gravitational radiation*, 83–126. Cambridge University Press, Cambridge, UK (1979)
- [186] L. D. ZANNA and N. BUCCIANTINI. *An efficient shock-capturing central-type scheme for multidimensional relativistic flows. i. hydrodynamics*. Astron. Astrophys., **390**:1177 (2002)
- [187] L. D. ZANNA, O. ZANOTTI, N. BUCCIANTINI *et al.* *Echo: an eulerian conservative high order scheme for general relativistic magnetohydrodynamics and magnetodynamics* (2007)
- [188] O. ZANOTTI, L. REZZOLLA, L. DEL ZANNA *et al.* *EM counterparts of recoiling black holes: general relativistic simulations of non-Keplerian discs*. Astron. Astrophys., **523**:A8 (2010)
- [189] A. ZENGINOGLU. *Hyperboloidal evolution with the Einstein equations*. Class. Quant. Grav., **25**:195025 (2008)

Abbreviations, Acronyms and Notation

ADM	Arnowitt Deser Misner
AH	Apparent Horizon
AMR	Adaptive Mesh Refinement
BAM	Bi-functional Adaptive Mesh (used evolution code)
BBH	Binary Black Hole
BH	Black Hole
BNS	Binary Neutron Star
BSSNOK	Baumgarte, Shapiro, Shibata, Nakamura, Oohara, Kojima
CENO	Convex ENO
CFL	Courant-Friedrich-Lewy
CTI	Corrected Time domain Integration
ENO	Essentially Non-Oscillatory
EoS	Equation of State
FFI	Fixed-Frequency Integration
GHG	Generalized Harmonic Gauge
GRMHD	General Relativistic Magneto Hydrodynamic
GW	Gravitational Wave
HLLC	Harten, Lax, van Leer, Einfeldt
HMNS	Hyper Massive Neutron Star
HRSC	High Resolution Shock Capturing
LLF	Local Lax-Friedrichs
LRZ	Leibnitz Rechenzentrum
MC2	Monotonized Cendered
MM2	MINMOD
MoL	Method of Lines
NS	Neutron Star
ODE	Ordinary Differential Equation
PDE	Partial Differential Equation
PPM	Piecewise Parabolic Method
RK(3/4)	Runge-Kutta 3/4
RHS	Right-Hand-Side
SGRB	Short Gamma Ray Burst
TOV	Tolman-Oppenheimer-Volkoff
TVD	Total Variation Diminishing
WENO	Weighted ENO

i, j, k, \dots	Latin indices take values 1...3
μ, ν, ρ, \dots	Greek indices take values 0...3
M_{\odot}	Mass of the sun
$\Im(z)$	Imaginary part of complex number z
$\Re(z)$	Real part of complex number z
$T^{\alpha_1 \dots \alpha_n}_{\beta_1 \dots \beta_m}$	Tensor of rank $\binom{m}{n}$
$\partial_{\gamma} T^{\alpha_1 \dots \alpha_n}_{\beta_1 \dots \beta_m}$	Partial derivative along the coordinate x^{γ}
$\nabla_{\gamma} T^{\alpha_1 \dots \alpha_n}_{\beta_1 \dots \beta_m}$	Covariant derivative along the coordinate x^{γ}
$\mathcal{L}_{\vec{\gamma}} T^{\alpha_1 \dots \alpha_n}_{\beta_1 \dots \beta_m}$	Lie derivative along the vector $\vec{\gamma}$

Acknowledgements

I would like to thank my advisor Prof. B. Brüggemann for giving me the possibility to work on this interesting topic as well as for always helping me with difficult problems.

I also want to thank Sebastiano Bernuzzi for helping during the implementation of the matter part of BAM and discussions about the topic. I also want to thank Doreen Müller and David Hilditch for an uncountable number of helpful discussions about physics and non related topics as well. I thank Andreas Weyhausen for helping me with computer related topics and of course all other members of our group.

Special thanks to Sebastiano, Doreen, David and Niall Ó Murchadha for proofreading my thesis.

Finally I want to thank my parents and my girlfriend Dana which always supported and encouraged me.

Lebenslauf

Marcus Thierfelder

01.06.1982 geboren in Rudolstadt
1989 - 1993 Grundschule Goetheschule Königsee
1993 - 1997 Dr. Max Näder Gymnasium Königsee
1997 - 2001 Gymnasium Goetheschule Ilmenau
23.06.2001 Abitur
2001 - 2002 Grundwehrdienst Dillingen a. d. Donau
2002 - 2008 Physikstudium Friedrich-Schiller-Universität Jena
04.02.2008 Diplom
2008 - 2011 wissenschaftlicher Mitarbeiter TPI Jena

Jena, 06.12.2011

Marcus Thierfelder

Ehrenwörtliche Erklärung

Ich erkläre hiermit ehrenwörtlich, dass ich die vorliegende Arbeit selbständig, ohne unzulässige Hilfe Dritter und ohne Benutzung anderer als der angegebenen Hilfsmittel und Literatur angefertigt habe. Die aus anderen Quellen direkt oder indirekt übernommenen Daten und Konzepte sind unter Angabe der Quelle gekennzeichnet.

Bei der Auswahl und Auswertung folgenden Materials haben mir die nachstehend aufgeführten Personen in der jeweils beschriebenen Weise unentgeltlich geholfen:

1. Prof. Brüggemann - beratend
2. Dr. Bernuzzi - beratend

Weitere Personen waren an der inhaltlich-materiellen Erstellung der vorliegenden Arbeit nicht beteiligt. Insbesondere habe ich hierfür nicht die entgeltliche Hilfe von Vermittlungs- bzw. Beratungsdiensten (Promotionsberater oder anderen Personen) in Anspruch genommen. Niemand hat von mir unmittelbar oder mittelbar geldwerte Leistungen für Arbeiten erhalten, die im Zusammenhang mit dem Inhalt der vorgelegten Dissertation stehen.

Die Arbeit wurde bisher weder im In- noch im Ausland in gleicher oder ähnlicher Form einer anderen Prüfungsbehörde vorgelegt.

Die geltende Promotionsordnung der Physikalisch-Astronomischen Fakultät ist mir bekannt.

Ich versichere ehrenwörtlich, dass ich nach bestem Wissen die reine Wahrheit gesagt und nichts verschwiegen habe.

Jena, 06.12.2011

Marcus Thierfelder

Zusammenfassung

In dieser Arbeit wurden ein Computerprogramm zur Simulation der Vakuum Einsteingleichungen erweitert um die allgemeinen relativistischen Hydrodynamik Gleichungen zu lösen. Diese wurden benutzt um numerische Neutronensternen zu simulieren, insbesondere um den Kollapse eines Neutronensternes zu untersuchen und um Gravitationswellen von Binärsystemen zu extrahieren. Die verwendeten numerischen Methoden werden beschrieben und an Testfällen validiert.

Die Implementation der HRSC Methode wurde am Shocktube validiert. Bei der Simulation eines stabilen Sterns konnte Konvergenz gezeigt werde. Die erwartete Oszillationsfrequenz des Sterns in radialer Richtung stimmt mit der Literatur überein. Weiterhin wurde ein bewegter simuliert und Konvergenz gezeigt.

Der Kollapse eines instabilen Neutronensternes und das daraus entstehende schwarze Loch wurde mit der Raumzeit einem einzelnen schwarzen Loches bei unter gleicher Eichung verglichen. Es wurde gezeigt, dass beide zur gleichen Lösung tendieren die mit der analytischen Lösung in guter Näherung bereinstimmt. Das Verschwinden der Materie konnte durch die benutzte shift-Bedingung erklärt werden.

Weiterhin wurden binäre Neutronenstern Systeme betrachtet die sich anfänglich in einem quasi-Equilibrium befindet und sich näherungsweise auf Kreisbahnen bewegt. Für diese Simulationen konnten wir während des Einspiralens Konvergenz und sehr gute Massenerhaltung zeigen. Der finale Stern kollabiert zu einem schwarzen Loch mit einer Akkretionsscheibe. Der Effekt von unterschiedlichen Eichbedingungen und verschiedenen Zustandsgleichungen auf die Simulation und auf die extrahierten Gravitationswellen wurden betrachte.